2019

The Application of Contemporary Numerical Methods to the Modeling, Analysis, and Uncertainty Quantification of Glacier Dynamics

Jacob Zachary Downs

THE APPLICATION OF CONTEMPORARY NUMERICAL METHODS TO THE MODELING, ANALYSIS, AND UNCERTAINTY QUANTIFICATION OF GLACIER DYNAMICS

By

JACOB ZACHARY DOWNS

Master of Science, University of Montana, Missoula, MT, 2016
Bachelor of Science, Rocky Mountain College, Billings, MT, 2013

Dissertation

presented in partial fulfillment of the requirements
for the degree of

Doctor of Philosophy
in Mathematics

The University of Montana
Missoula, MT

December 2019

Approved by:

Scott Whittenburg,
Graduate School Dean

Dr. Jesse Johnson, Chair
Computer Science

Dr. Joel Harper
Geosciences

Dr. John Bardsley
Mathematical Sciences

Dr. Cory Palmer
Mathematical Sciences

Dr. Stephen Price
Fluid Dynamics Group, Los Alamos National Laboratory

The Application of Contemporary Numerical Methods to the Modeling, Analysis, and Uncertainty Quantification of Glacier Dynamics

Chairperson: Dr. Jesse V. Johnson

Warming temperatures have led to accelerating ice loss from the Greenland ice sheet, contributing to global sea level rise. Understanding the stability of the Greenland ice sheet to further warming is crucial to estimating rates of sea level rise over the next century. Estimating sea level rise is complicated by uncertainties in the physical mechanisms governing ice motion as well as uncertainties in the broader Arctic climate system of which the ice sheet is an integral part.

In chapter 2, we focus on how surface melt water input to the ice sheet bed influences the rate of basal sliding, which is thought to depend on the seasonal evolution of the subglacial drainage system. Models of subglacial drainage have developed considerably in recent years. However, the recent sublglacial hydrology model intercomparison project (SHMIP), presented in Appendix A, shows that a wide gamut of models underpredict subglacial water pressure in winter when compared to borehole water pressure observations from Greenland. We investigate possible causes for this unphysical model behavior, ranging from poorly constrained model parameters to uncertainties in the physical equations for subglacial drainage. We conclude that the mismatch between modeled and observed winter water pressure can be remedied by dynamically adjusting the hydraulic conductivity parameter, which accounts for missing physics in the models describing seasonal changes in drainage system connectivity.

Chapter 3 focuses on contextualizing modern climate change in the Arctic by investigating past changes in temperature and precipitation. In particular, we exploit a new chronology of ice sheet retreat in west Central Greenland, along with a novel data assimilation method based on the unscented transform (UT), to estimate changes in precipitation during the Holocene Thermal Maximum (HTM) -- a period of higher than modern temperatures that occurred some eight-thousand years ago. We demonstrate the effectiveness of the UT as a method for data assimilation and uncertainty quantification and show new evidence that the HTM was associated with greater than modern snowfall, which helped mitigate ice sheet retreat.

Contents

0.1 Acknowledgments

My sincere thanks to:

- My advisor Jesse Johnson, who has supported me academically and personally over the last six years. It's been a wild ride from Lovecraftian aliens, to PDEs and Sator squares, to New York City perambulations and Thanksgiving dinners. He's taught me a tremendous amount and done it in style.

- Toby Meirbachtol, Joel Harper, and Doug Brinkerhoff who consistently challenged my thinking and helped me crystallize ideas.

- My labmates past and present including (but not limited to) Caitlyn, Fred, Rosie (firn queen) Leone, Jimmy, Ben, Aidan, Patrick, Aaron, and Evan for much needed distractions and support. There's still no consensus on how dogs should wear pants though.

- Past mentors and teachers including Kim Smith, Andy Wildenberg, Deb Wiens, and Ulrich Hoensch who recognized some potential in me that I couldn't see.

- My family and close friends. Specifically to my mom and dad for unconditional love, support, and patience. Math is a logical pursuit, but pursuing math is not logical. To my sister for being the best friend I could hope for. To my friends Tyler and Ryan and girlfriend Sabrina for hearty laughs, moral support, and uplifting conversations.

Chapter 1

Introduction

The Arctic is undergoing rapid changes. Ice loss from the Greenland ice sheet (GrIS) is accelerating while sea ice cover is diminishing (IPCC, 2018). A complete meltdown of the GrIS would raise global sea levels by more than seven meters (IPCC, 2018). Hence, it is critical to understand if further warming will destabilize the ice sheet and lead to rapid sea level rise. The primary aim of this work is to better understand the sensitivity of the GrIS to warming temperatures using numerical models of ice flow and subglacial water flow constrained by field measurements.

Predicting the rate of ice loss in Greenland is complicated by uncertainties in the physical mechanisms governing ice motion. Glacier ice moves fluidly due to deformation under the force of gravity and due to basal sliding. Ice deformation is reasonably well understood in terms of the language of fluid mechanics. Pioneering work by Glen (1952) and Nye (1953) helped formalize the commonly accepted equations for ice flow, which led to the development of modern ice sheet models.

In the interior of the GrIS, the base of the ice is frozen to the bed, and ice motion is purely deformational. Nearer the margins of the ice sheet, basal melting and surface melt water input to the bed via crevasses and moulins (semi-vertical shafts in the ice)

reduce basal traction and induce basal sliding, presumably by altering subglacial water pressure and ice-bed contact (e.g. Bartholomew et al., 2010; Hoffman et al., 2011). Basal sliding contributes to ice loss by rapidly transporting ice from colder, higher regions to lower, warmer regions where it melts or calves into the ocean. Consequently, there is concern that increasing surface melt will accelerate basal sliding (Olivier and Werder, 2018).

The seasonal evolution of the subglacial drainage system is thought to play an important role in controlling the rate of basal sliding. This is evidenced by the ice surface velocity, which can more than double from winter to early summer (Bartholomew et al., 2010; Sundal et al., 2011). Conceptually, without sustained surface melt input, drainage pathways at the base of the ice squeeze shut during the winter (Hewitt, 2013). In the spring, a surge of surface meltwater overwhelms the drainage system, resulting in high subglacial water pressure, reduced ice-bed contact, and faster basal sliding. As the melt season progresses, the capacity and efficiency of the subglacial drainage system increases due to opening of drainage pathways and the formation of subglacial channel networks in the vicinity of the ice sheet margin (Hewitt, 2013).

Due to the difficulty of directly observing the subglaical drainage sytem, the glaciology community has turned to subglacial hydrology models to gain new insights into the physical processes controlling basal sliding. Recently, significant advances have been made in modeling subglacial hydrology, particularly with the advent of multi-element models combining continuum descriptions of water flow through linked-cavity systems with either discrete (e.g. Werder et al., 2013) or continuum (e.g. De Fleurian et al., 2014; Sommers et al., 2018) models of channelized drainage. A wide variety of contemporary approaches to modeling subglacial drainage are discussed in chapter 2 and appendix A.

While contemporary models have succeeded in capturing many expected features of the subglacial drainage system (Flowers, 2015; Werder et al., 2013), they suffer from a number of shortcomings. The physical equations describing distributed drainage on

the large spatial scales required for ice sheet models are highly uncertain (Hoffman and Price, 2014). These uncertainties lead to unphysical behavior in certain circumstances. For example, a wide gamut of models (in fact, every model) participating in a recent subglacial hydrology model intercomparison project (SHMIP), predict low subglacial water pressure in response to surface melt water attenuation during the winter (De Fleurian et al., 2018). This is is in spite of borehole water pressure measurements that show high sustained winter water pressure (Wright et al., 2016; Ryser et al., 2014; Van De Wal et al., 2015).

This discrepancy, which alludes to a gap in the current physical theory, is explored extensively in chapter 2. In this chapter, we compare modeled and observed subglacial water pressures using a custom implementation of the GlaDS model, which includes both distributed and channelized drainage components (Werder et al., 2013). We demonstrate a significant discrepancy between modeled and observed winter water pressures using a wide range of plausible parameter values on both synthetic and realistic glacier geometries. After exploring a variety of potential causes, we argue that the discrepancy is likely due to missing physics in the model describing seasonal changes in the connectivity of the distributed drainage system. Dynamically adjusting the hydraulic conductivity parameter in GlaDS and many similar continuum models can account for these changes in drainage system connectivity (Downs et al., 2018).

Modeling ice dynamics is crucial to understanding the stability of the Greenland ice sheet. However, it is also important to view the GrIS as part of the broader Arctic climate system. Ice sheet models and subglacial hydrology models are useful tools for testing ice sheet stability, but they require surface mass balance inputs quantifying the rate of accumulation / ablation over the ice surface. Surface mass balance in turn depends on the complex relationship between temperature and precipitation. Arctic warming and sea-ice decline is expected to result in a greater than 50% increase in precipitation by the end of the century (Bintanja and Selten, 2014). Thus, it is possible that surface

melting will be somewhat offset by increased ice accumulation due to elevated snowfall over the GrIS.

Modern Arctic warming has a geologically recent precedent. Terrestrial and marine climate proxies from the northern hemisphere suggest temperatures in Greenland peaked at 2.5 - 3 °C above modern during a period referred to as the Holocene Thermal Maximum (HTM). This warming, likely caused by greater than modern insolation, occurred at different times in different areas of Greenland (Kaufman et al., 2004; Marcott et al., 2013). For example, borehole temperature reconstructions show an HTM signal from 7 - 4 ka BP (thousands of years before present) at the Dye-3 borehole site versus 8 - 5 ka BP at GRIP (Renssen et al., 2012) (see Figure 3.1 for borehole locations).

Recently, Buizert et al. (2018) used a data assimilation approach to merge ice core records and climate model output to create spatially explicit estimates of temperature through the Holocene ($\sim$ 11.7 ka BP onward). While the data assimilation techniques in Buizert et al. (2018) also yield precipitation estimates, there are few direct proxy records of precipitation that can be used to constrain climate output.

In chapter 3, we outline a novel data-assimilation approach exploiting a new chronology of ice sheet terminus position during the Holocene (Young et al., 2019) to constrain a flowline ice sheet model and generate quantitative estimates of Holocene precipitation in the Kangerlussuaq region of west central Greenland. Our data assimilation approach is based on the unscented transform, a method of estimating the characteristics of a non-Gaussian probability distribution using a small, deterministic set of sample points.

We argue that this method has advantages over alternative methods, including more commonly used random sampling methods, for certain problems due to its low computational cost and innate parallelism. Our results suggest that HTM warming was associated with greater than modern snowfall, which helped stabilize the GrIS.

Bibliography

Bartholomew, I., Nienow, P., Mair, D., Hubbard, A., King, M. A., and Sole, A. (2010). Seasonal evolution of subglacial drainage and acceleration in a Greenland outlet glacier. *Nature Geoscience*.

Bintanja, R. and Selten, F. M. (2014). Future increases in Arctic precipitation linked to local evaporation and sea-ice retreat. *Nature*.

Buizert, C., Keisling, B. A., Box, J. E., He, F., Carlson, A. E., Sinclair, G., and DeConto, R. M. (2018). Greenland-Wide Seasonal Temperatures During the Last Deglaciation. *Geophysical Research Letters*.

De Fleurian, B., Gagliardini, O., Zwinger, T., Durand, G., Le Meur, E., Mair, D. W. F., and Räback, P. (2014). A double continuum hydrological model for glacier applications. *Cryosphere*, 8(1):137–153.

De Fleurian, B., Werder, M. A., Beyer, S., Brinkerhoff, D. J., Delaney, I., Dow, C. F., Downs, J., Gagliardini, O., Hoffman, M. J., Hooke, R. L., Seguinot, J., and Sommers, A. N. (2018). SHMIP The subglacial hydrology model intercomparison Project. *Journal of Glaciology*, 64(248):897–916.

Downs, J., Johnson, J., Harper, J., Meierbachtol, T., and Werder, M. (2018). Dynamic Hydraulic Conductivity Reconciles Mismatch Between Modeled and Observed Winter Subglacial Water Pressure. *Journal of Geophysical Research: Earth Surface*, 123(4).

Flowers, G. E. (2015). Modelling water flow under glaciers and ice sheets.

Glen, J. W. (1952). Experiments on the Deformation of Ice. *Journal of Glaciology*.

Hewitt, I. J. (2013). Seasonal changes in ice sheet motion due to melt water lubrication. *Earth and Planetary Science Letters*, 371-372:16–25.

Hoffman, M. and Price, S. (2014). Feedbacks between coupled subglacial hydrology and glacier dynamics. *Journal of Geophysical Research: Earth Surface*, 119(3):414–436.

Hoffman, M. J., Catania, G. A., Neumann, T. A., Andrews, L. C., and Rumrill, J. A. (2011). Links between acceleration, melting, and supraglacial lake drainage of the western Greenland Ice Sheet. *Journal of Geophysical Research: Earth Surface*.

IPCC (2018). IPCC Special Report 1.5 - Summary for Policymakers. In Masson-Delmotte, V., Zhai, P., Pörtner, H. O., Roberts, D., Skea, J., Shukla, P. R., Pirani, A., Moufouma-Okia, W., Péan, C., Pidcock, R., Connors, S., Matthews, J. B. R., Chen, Y., Zhou, X., Gomis, M. I., Lonnoy, E., Maycock, T., Tignor, M., and Waterfield, T., editors, *Global warming of 1.5 C. An IPCC Special Report on the impacts of global warming of 1.5 C above pre-industrial levels and related global greenhouse gas emission pathways, in the context of strengthening the global response to the threat of climate change,*, page 32. World Meteorological Organization.

Kaufman, D. S., Ager, T. A., Anderson, N. J., Anderson, P. M., Andrews, J. T., Bartlein, P. J., Brubaker, L. B., Coats, L. L., Cwynar, L. C., Duvall, M. L., Dyke, A. S., Edwards, M. E., Eisner, W. R., Gajewski, K., Geirsdóttir, A., Hu, F. S., Jennings, A. E., Kaplan, M. R., Kerwin, M. W., Lozhkin, A. V., MacDonald, G. M., Miller, G. H., Mock, C. J., Oswald, W. W., Otto-Bliesner, B. L., Porinchu, D. F., Rühland, K., Smol, J. P., Steig, E. J., and Wolfe, B. B. (2004). Holocene thermal maximum in the western Arctic (0-180 W). *Quaternary Science Reviews*.

Marcott, S. A., Shakun, J. D., Clark, P. U., and Mix, A. C. (2013). A reconstruction of regional and global temperature for the past 11,300 years. *Science*, 339(6124):1198–1201.

Nye, J. F. (1953). The Flow Law of Ice from Measurements in Glacier Tunnels, Lab-

oratory Experiments and the Jungfraufirn Borehole Experiment. *Proceedings of the Royal Society A: Mathematical, Physical and Engineering Sciences*.

Olivier, G. and Werder, M. A. (2018). Influence of increasing surface melt over decadal timescales on land-terminating Greenland-type outlet glaciers. *Journal of Glaciology*, 64(247):700–710.

Renssen, H., Seppä, H., Crosta, X., Goosse, H., and Roche, D. M. (2012). Global characterization of the Holocene Thermal Maximum. *Quaternary Science Reviews*.

Ryser, C., Lüthi, M. P., Andrews, L. C., Catania, G. A., Funk, M., Hawley, R., Hoffman, M., and Neumann, T. A. (2014). Caterpillar-like ice motion in the ablation zone of the Greenland ice sheet. *Journal of Geophysical Research: Earth Surface*, pages n/a–n/a.

Sommers, A., Rajaram, H., and Morlighem, M. (2018). SHAKTI: Subglacial hydrology and kinetic, transient interactions v1.0. *Geoscientific Model Development*.

Sundal, A. V., Shepherd, A., Nienow, P., Hanna, E., Palmer, S., and Huybrechts, P. (2011). Melt-induced speed-up of Greenland ice sheet offset by efficient subglacial drainage. *Nature*.

Van De Wal, R. S., Smeets, C. J., Boot, W., Stoffelen, M., Van Kampen, R., Doyle, S. H., Wilhelms, F., Van Den Broeke, M. R., Reijmer, C. H., Oerlemans, J., and Hubbard, A. (2015). Self-regulation of ice flow varies across the ablation area in south-west Greenland. *Cryosphere*.

Werder, M. A., Hewitt, I. J., Schoof, C. G., and Flowers, G. E. (2013). Modeling channelized and distributed subglacial drainage in two dimensions. *Journal of Geophysical Research: Earth Surface*, 118(4):2140–2158.

Wright, P. J., Harper, J. T., Humphrey, N. F., and Meierbachtol, T. W. (2016). Measured

basal water pressure variability of the western Greenland Ice Sheet: Implications for hydraulic potential. *Journal of Geophysical Research: Earth Surface*.

Young, N. E., Briner, J. P., Miller, G. H., Crump, S. E., Lesnek, A. J., and Thomas, E. K. (2019). Arctic deglaciation interrupted by abrupt coolings. *Science Advances*.

Chapter 2

Dynamic hydraulic conductivity reconciles mismatch between modeled and observed winter subglacial water pressure

Overview

This chapter was previously published in JGR Earth surface.

Authors

Jacob Downs, Jesse Johnson, Joel Harper, Toby Meierbachtol, Mauro Werder

Abstract

The link between subglacial hydrology and basal sliding has prompted work on basal hydrology models with water pressure and drainage capacity as prognostic variables.

We find that the Glacier Drainage System model (GlaDS), which belongs to a commonly used family of subglacial hydrology models that include both channelized and distributed drainage components, underpredicts winter water pressure when compared to borehole observations from western Greenland given a wide range of plausible parameter values and inputs. This problem, though previously noted by other modelers, has not been addressed. Possible causes for the discrepancy including idealized model inputs or unconstrained parameters are investigated through a series of modeling experiments on both synthetic and realistic ice sheet geometries. Numerical experiments reveal that englacial storage and hydraulic conductivity in the distributed system are the primary controls on winter water pressure in GlaDS. Observations of temperate layer thickness and englacial water content from Western Greenland imply an upper bound on englacial storage, suggesting that a reduction in hydraulic conductivity is the most plausible cause of high winter water pressure. We conclude that hydraulic conductivity acts as a proxy for the subgrid scale connectivity of the linked cavity system and should therefore change seasonally in correspondence with melt water availability.

2.1 Introduction

Surface melt input into the subglacial drainage system is believed to play a significant role in controlling the rate of basal sliding of the Greenland Ice Sheet (*Zwally et al.*, 2002; *Shepherd et al.*, 2009; *van de Wal et al.*, 2008) as evidenced by surface velocity, which can more than double from winter to early summer (*Bartholomew et al.*, 2010; *Sundal et al.*, 2011). However, the relationship between surface melt and basal sliding is poorly understood. More surface melt does not necessarily translate to faster basal sliding (*Zwally et al.*, 2002; *Bartholomew et al.*, 2010; *Hoffman et al.*, 2011). The complex coupling between surface melt and sliding speed depends on the evolution of the subglacial drainage system as it adapts to variations in melt input to the bed on diurnal

and seasonal time scales (e.g. *Hewitt et al.*, 2012).

Seminal publications such as *Iken* (1972), *Budd et al.* (1979), and *Bindschadler* (1983) recognized a possible link between water pressure in the subglacial drainage system and basal sliding. Efforts are ongoing to develop sliding laws that mathematically relate sliding velocity to water pressure (e.g. *Schoof*, 2005), formalizing the idea that higher water pressure reduces contact between the ice sheet and bed, leading to faster sliding. Borehole water pressure measurements in Greenland illustrate a shortcoming of this idea. While boreholes offer only a localized glimpse of drainage system behavior, measurements presented in *Wright et al.* (2016), *Ryser et al.* (2014), and *van De Wal et al.* (2015) all show that borehole water pressures remain high through the fall and winter, even as sliding velocity decreases (*Palmer et al.*, 2011).

The difficulty of directly observing the subglacial drainage system has motivated work on basal hydrology models simulating water storage and pressure. Models of distributed drainage through linked cavities introduced by *Hewitt* (2011) and *Schoof et al.* (2012) provided a versatile foundation for a family of recent multicomponent models that incorporate additional drainage elements such as channels (*Werder et al.*, 2013; *Hewitt et al.*, 2012) and till (*Bueler and Van Pelt*, 2015). Model developers face the difficult task of balancing practical mathematical and computational concerns with physical fidelity. Though models have advanced significantly, there are still fundamental uncertainties in the governing physical equations, as well as a host of poorly constrained parameters.

A known problem with current models is their tendency to underpredict winter water pressure (e.g. *Werder et al.*, 2013; *Flowers*, 2015). The inability of models to match observations suggests that they may be neglecting or oversimplifying important physical processes. *Hoffman et al.* (2016), for example, have proposed introducing a new weakly connected component to the current distributed drainage model. Previous modeling work has focused on the evolution of the drainage system during the melt season, but the winter mode of the drainage system is perhaps equally important. *Sole et al.* (2013)

observed that high melt years do not have significantly faster surface velocities than low melt years because fast summer ice flow is offset by slow ice flow in subsequent winters. The winter dynamics of the subglacial drainage system are important for determining total annual ice flow.

Here we address the problem of low modeled winter water pressure . We find that the Glacier Drainage System model (GlaDS) (*Werder et al.*, 2013), a model of water flow through linked cavities and R-channels. Through a gamut of simulations on both synthetic and realistic ice sheet geometries, we investigate a number of possible causes of low modeled winter water pressure including poorly constrained model inputs and parameters to neglected physical processes (Section 2.3).

2.2 Model Description and Modeling Methodology

In numerical experiments, we use a custom implementation of the Glacier Drainage System Model (GlaDS), which combines a continuum representation of flow through linked cavities with a discrete channel model. Prognostic variables include spatially averaged cavity height h (also referred to as sheet height or sheet thickness), channel cross-sectional area S, and hydraulic potential ϕ. Channel specific fields such as S are discrete variables defined on the edges of the unstructured finite element mesh used in numerical simulations, while ϕ and h are continuous variables on the 2D spatial domain Ω. Model inputs include bed elevation B, ice thickness H, melt input to the bed m, and sliding speed u_b.

Spatially averaged cavity height h is modeled as a balance between opening $w(h)$ due to sliding over bedrock bumps and creep closure $v(h, N)$:

$$\frac{\partial h}{\partial t} = w(h) - v(h, N). \tag{2.1}$$

Cavity opening due to melting of cavity walls is assumed to be negligible. Opening and closing rates are given by

$$w(h) = \begin{cases} \frac{u_b(h_r - h)}{l_r} & h \leq h_r \\ 0 & \text{otherwise} \end{cases} \tag{2.2}$$

and

$$v(h, N) = \frac{2}{27} A h N^3 \tag{2.3}$$

respectively. Here, h_r is characteristic bump height, l_r is characteristic bump length, A is the rate factor for ice, and N is effective pressure. Effective pressure is defined as

$$N = p_i - p_w$$

where $p_i = \rho_i g H$ is ice overburden pressure and p_w is water pressure. Hydraulic potential ϕ and water pressure are directly related. In particular

$$\phi = \phi_m + p_w$$

where $\phi_m = \rho_w g B$ is the elevation potential. Hence, effective pressure can also be related directly to the unknown ϕ by

$$N = \phi_0 - \phi$$

with $\phi_0 = \phi_m + p_i$.

The height of water h_w within cavities obeys a conservation equation

$$\frac{\partial h_w}{\partial t} + \frac{\partial h_e}{\partial t} + \nabla \cdot \mathbf{q} = m. \tag{2.4}$$

where $\mathbf{q}$ is flux and h_e represents the volume of water stored in an englacial aquifer per

Table 2.1: Summary of all model constants, inputs, and parameters used in this work. Default values are provided where applicable.

Description	**Symbol**	**Value**	**Units**
Physical Constants			
Gravitational acceleration	g	9.81	m s^{-2}
Ice density	ρ_i	910	kg m^{-3}
Water density	ρ_w	1000	kg m^{-3}
Pressure melt coefficient	c_t	7.5 $\times 10^{-8}$	K Pa^{-1}
Heat capacity of water	c_w	4.22 $\times 10^{3}$	J kg^{-1} K^{-1}
Model Inputs			
Bed elevation	B	-	m
Ice thickness	H	-	m
Melt input	m		m s^{-1}
Sliding speed	u_b	-	m s^{-1}
Potential at 0 pressure	ϕ_m	$\rho_w g B$	Pa
Ice overburden pressure	p_i	$\rho_i g H$	Pa
Overburden potential	ϕ_0	$\phi_m + p_i$	Pa
Model Outputs			
Cavity height	h	-	m
Channel cross-sectional area	S	-	m^2
Hydraulic potential	ϕ	-	Pa
Water pressure	p_w	$\phi - \phi_m$	Pa
Effective pressure	N	$\phi_0 - \phi$	Pa
Model Parameters			
Hydraulic conductivity	k	-	$m^{\frac{7}{4}} kg^{-\frac{1}{2}}$
Bump height	h_r	0.1	m
Bump spacing	l_r	2	m
Englacial void ratio	e_v	0	-
Channel roughness	k_c	0.1	$m^{\frac{3}{2}} kg^{-\frac{1}{2}}$
Sheet width below channel	l_c	2	m
Rate factor for ice	A	6.7 $\times$ 10 $^{-24}$	Pa^{-3} s^{-1}
Flux exponent	α	5/4	-
Flux exponent	β	3/2	-

unit area of the bed. h_e is related to water pressure via

$$h_e\left(p_w\right) = \frac{e_v p_w}{\rho_w g} = \frac{e_v\left(\phi - \phi_m\right)}{\rho_w g} \tag{2.5}$$

where e_v is the englacial void ratio. *Schoof et al.* (2012) propose a general spatially averaged flux relation of the form

$$\mathbf{q} = -k h_w^{\alpha} |\nabla\phi|^{\beta-2} \nabla\phi. \tag{2.6}$$

Here k is hydraulic conductivity, $\alpha \geq 1$, and $\beta > 1$. We use $\alpha = \frac{5}{4}$ and $\beta = \frac{3}{2}$ for turbulent flow, corresponding to the Darcy-Weisbach formula.

The cross sectional area S of a single channel is modeled as a balance between opening due to dissipation of potential energy and changes in the pressure melting point of ice denoted by $\frac{\Xi - \Pi}{\rho_i L}$, as well as creep closure v_c:

$$\frac{\partial S}{\partial t} = \frac{\Xi - \Pi}{\rho_i L} - v_c = \frac{\Xi - \Pi}{\rho_i L} - \frac{2}{27} A S N^3. \tag{2.7}$$

Viscous dissipation Ξ is given by

$$\Xi = \left| Q \frac{\partial\phi}{\partial s} \right| + \left| l_c q_c \frac{\partial\phi}{\partial s} \right|. \tag{2.8}$$

Here, Q is channel discharge, l_c is a parameter controlling the width of sheet around the channel that contributes to channel melt, $q_c = -k h_w^{\alpha} \left| \frac{\partial\phi}{\partial s} \right|^{\beta-2} \frac{\partial\phi}{\partial s}$ is the discharge in the linked cavity system flowing parallel to the channel, and s denotes the horizontal coordinate along the channel. Channel discharge Q has the same form as sheet flux

$$Q = -k_c S_w^{\alpha} \left| \frac{\partial\phi}{\partial s} \right|^{\beta-2} \frac{\partial\phi}{\partial s} \tag{2.9}$$

with k_c a channel roughness parameter. Π represents sensible heat change and is given

by

$$\Pi = -c_t c_w \rho_w \left(Q + f l_c q_c\right) \frac{\partial p_w}{\partial s}. \tag{2.10}$$

Here, c_t is the Clapeyron slope, c_w is the specific heat capacity of water, and f is a switch enabling or disabling refreezing defined by

$$f = \begin{cases} 1 & \text{if } S > 0 \text{ or } \frac{\partial p_w}{\partial s} > 0 \\ 0 & \text{otherwise} \end{cases}.$$

As with h, there is a conservation equation for the cross sectional area S_w of water within channels

$$\frac{\partial S_w}{\partial t} + \frac{\partial Q}{\partial s} = \frac{\Xi - \Pi}{\rho_w L} + m_c \tag{2.11}$$

where m_c is the rate at which water enters the channel from the linked cavity system. *Werder et al.* (2013) assume that cavities and channels are always fully saturated ($h = h_w$, $S = S_w$). Combining equation 2.1 with equation 2.4 and equation 2.7 with equation 2.11 then yields the following PDEs:

$$\frac{e_v}{\rho_w g}\frac{\partial \phi}{\partial t} + \nabla \cdot \mathbf{q} + w - v - m = 0 \tag{2.12}$$

$$\frac{\partial Q}{\partial s} + \frac{\Xi - \Pi}{L}\left(\frac{1}{\rho_i} - \frac{1}{\rho_w}\right) - v_c - m_c = 0. \tag{2.13}$$

The model is closed by enforcing water conservation at nodal points of the computational mesh where channels intersect. Water pressure is assumed to be continuous between the linked cavity system and channels in order to determine m_c and couple the distributed system to the channel network.

Hydraulic potential ϕ is subject to conditions on the domain boundary $\partial\Omega$ including pressure (Dirichlet) boundary conditions on part of the boundary $\partial\Omega_D$ and flux (Neu-

mann) boundary conditions on the remainder of the boundary $\partial\Omega_N$. Neumann boundary conditions take the form

$$\mathbf{q} \cdot \mathbf{n} = q_N$$

where $\mathbf{n}$ is the outward normal vector to the boundary and q_N is some prescribed influx or outflux. Usually, $\phi = \phi_m$ (zero pressure) is prescribed on boundaries where outflow is expected and $\mathbf{q} \cdot \mathbf{n} = 0$ (zero flux) is prescribed elsewhere. Details related to the numerical solution of the model equations are provided in Appendix 2.A.

2.2.1 Modeling Methodology

In the following numerical experiments, we attempt to qualitatively match winter water pressure observations using GlaDS. Our goal is to reproduce the broad seasonal trend of high winter water pressure observed by *Wright et al.* (2016), *Ryser et al.* (2014), *van De Wal et al.* (2015), and *Meierbachtol et al.* (2013). We conduct experiments on both synthetic and realistic ice sheet geometries. In contrast to previous studies such as *Hoffman and Price* (2014) and *Hewitt* (2013), where basal hydrology models are coupled to ice sheet models, we do not model ice sheet dynamics. Both basal sliding speed and ice thickness are prescribed (see Section 2.2.3 on modeling methodology limitations for justification).

Synthetic experiments take place on a 60 x 20 km rectangular domain (Figure 2.2a). A plastic ice-sheet surface profile (*Cuffey and Patterson*, 2010, chap. 8) with a maximum thickness of 1500 meters ($\approx$ 167 kPa yield stress) is used for ice sheet thickness (Figure 2.2c) along with either a flat or trough bedrock geometry (Figure 2.2b). Summer sliding speed (Figure 2.2c) and melt input (Figure 2.2d) increase linearly approaching the terminus.

Summer inputs for synthetic runs are intended to broadly represent a typical Greenland outlet glacier, but favor simplicity over physical fidelity to make results easy to

interpret. In particular, the synthetic sliding speed profile does not decrease in the vicinity of the terminus as expected for a land terminating glacier. For this reason, we also perform several experiments using realistic model inputs from the Isunnguata Sermia / Russel Glacier region of western Greenland. We use measurements of bed elevation (Figure 2.3a) and ice thickness (Figure 2.3b) from *Bamber et al.* (2013), and surface mass balance (Figure 2.3a) from *Ettema et al.* (2009). Previous modeling work in the region indicates that most ice motion can be attributed to basal sliding (*Meierbachtol et al.*, 2015). Hence, we use 2007-2008 averaged surface velocity data from *Joughin et al.* (2010) for summer sliding speed (Figure 2.3c). The impact of uncertainty in the rate of basal sliding is explored in Section 2.3.

In our implementation of GlaDS, channelized drainage is treated akin to a parameter that can be toggled on or off. This is easily accomplished by neglecting the two channel equations 2.7 and 2.13, reducing the model to equations 2.1 and 2.12. The reduced model is recognizable as the linked cavity model of *Schoof et al.* (2012) with an added englacial storage term.

In all runs, the model is allowed to reach a state representative of the end of summer. If channelized drainage is disabled, the model is allowed to reach a steady state with summer melt input and sliding speed. Changes in water pressure and sheet height are usually minor after around four months. If channelization is enabled, we initialize the model with a constant sheet height of 2 cm and no channel network, then allow the channel network to develop for four months with high summer melt input and sliding speed. We adopt this approach because the steady state configuration of the channel network can take multiple years to develop and is not an accurate representation of the state of the channel network after the relatively short melt season.

As in *Hewitt* (2013), we use hydraulic conductivity as a tuning parameter to obtain a spatially averaged end of summer water pressure of 85% of overburden pressure in synthetic runs and 82.5% of overburden pressure in realistic runs as other parameters

or inputs are varied. These values are selected to emulate borehole observations, which typically fluctuate between 80% to 110% of overburden pressure during the melt season (*Wright et al.*, 2016), yet avoid the limitations of the model at overburden pressure discussed in Section 2.2.2 on model limitations. Water pressure constraints are applied in runs on realistic geometry, which are tuned to a lower summer water pressure in order to avoid significant mass loss in areas constrained to overburden pressure (refer to Section 2.2.2 for more details).

In order to simulate the fall shut down, melt input and sliding speed are reduced over the course of one month by multiplying the spatially varying summer melt and sliding speed functions by smoothly decreasing scaling functions (see equations 2.18 and 2.19 in Appendix 2.B). By default, surface melt input ceases completely after one month. Sliding speed decreases by a factor of two thirds over this period. When displaying simulation results, time 0 denotes the end of summer, and winter starts at month one. More details related to the melt input and sliding methodology are provided in Appendix 2.B.

Wright et al. (2016) observed nearly identical median summer and winter water pressure across several boreholes. On average, borehole water pressures tended to be at least as high (if not slightly higher) in winter compared to the melt season (e.g. Figure 2.1). To broadly compare observed and modeled water pressures, we adopt a metric called the seasonal pressure variability (SPV) ratio, defined as average winter water pressure divided by end of summer water pressure. Low SPV ratios indicate an unrealistic drop in modeled water pressure over the winter, whereas SPV values near 1 indicate higher winter water pressure more broadly consistent with observations.

SPV ratios are calculated at the three reference points in Figure 2.2a for synthetic experiments and the four reference points in Figure 2.3a for realistic experiments. Reference point locations are selected to capture spatial variations in water pressure. A domain-wide SPV ratio is also calculated by dividing the average winter water pressure

in both time and space by the spatially averaged end of summer pressure.

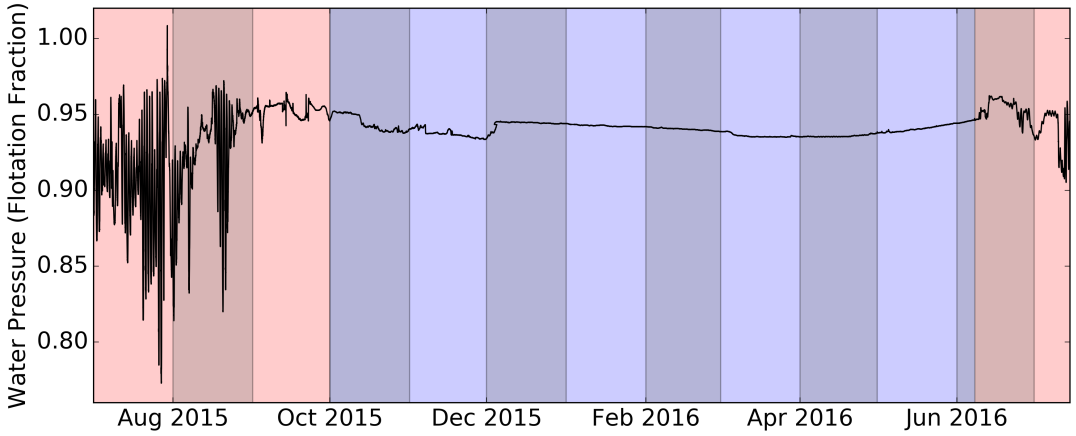

Figure 2.1: Time series of observed subglacial water pressure at borehole site 27km-12A in Isunnguata Sermia from *Wright et al.* (2016). The characteristic winter period is shaded in blue. The location of 27km-12A is marked in Figure 2.3a. This record is typical of borehole observations in the ice sheet interior.

2.2.2 Model Limitations

GlaDS contains several poorly constrained parameters including hydraulic conductivity k, bedrock bump parameters h_r and l_r, and englacial void ratio e_v (see Table 2.1). Many of these parameters cannot be observed directly or would be better represented by a spatially, and in some cases temporally, varying function rather than a constant value. Naturally there is uncertainty associated with model inputs such as sliding speed and melt input. Perhaps more critical than unconstrained parameters are fundamental uncertainties in equations 2.1 and 2.6 governing cavity opening / closing and flux respectively (*Hoffman and Price*, 2014). Little work has been done to bridge the gap between large scale models of distributed drainage such as *Hewitt* (2011) and *Schoof et al.* (2012) and earlier, small scale models describing the the physics governing individual links and cavities (e.g. *Kamb* (1987)).

As posed, the model may predict water pressure below zero or well above overbur-

den pressure. As a partial solution to this problem, we have implemented GlaDS with the ability to constrain water pressure between atmospheric pressure and overburden pressure using PETSc (Portable, Extensible Toolkit for Scientific Computation). In particular, we use one of PETSc's scalable nonlinear equations solvers called the variational inequality solver or SNESVI (*Balay et al.*, 2016). We have verified that our approach is equivalent to the variational inequality approach outlined in *Schoof et al.* (2012) by comparing the SNESVI solver to an alternative minimization method proposed by *Schoof et al.* (2012).

Where water pressure constraints are active, cavity height and water height as well as channel and water cross sectional areas may no longer be equal and should therefore be solved for separately (*Schoof et al.*, 2012; *Hewitt et al.*, 2012). Due to the complexity of implementing this approach in a 2D model, we continue to assume that cavities and channels are saturated in these regions. A drawback is that water is added where water pressure is constrained to zero and lost in areas constrained to overburden pressure.

This problem is not unique to our implementation, but reflects a more general problem with applying water pressure constraints in GlaDS and similar models that use the saturation assumption. An alternative approach is given by *Bueler and Van Pelt* (2015) who truncate water pressure below zero or above overburden and conserve water by solving for water height using the conservation Equation 2.4 rather than for cavity height using Equation 2.11.

In practice, we find that applying water pressure constraints is only necessary in simulations on realistic geometry. When constraints are enforced, mass conservation errors typically represent around $\pm$ 10% of the total melt input. However, most mass loss or gain occurs near the outflow boundary at the terminus where it is less likely to have a significant impact on results.

2.2.3 Modeling Methodology Limitations

A limitation of our modeling approach is that the subglacial hydrology model is not coupled to an ice sheet model via a sliding law. We believe that the disadvantages of introducing a sliding law outweigh the disadvantages of prescribed sliding in this case since we know of no sliding law that can explain winter observations of slow sliding speed (*Palmer et al.*, 2011) and high water pressure (*Wright et al.*, 2016). However, prescribing sliding may obscure important coupling in model parameters. Therefore, in section 2.3.2, we consider how uncertainties in prescribed sliding speed impact winter water pressure.

Because the model is uncoupled, we cannot use modeled basal traction to estimate the rate of basal melt. Geothermal heat flux is also poorly constrained. Some modelers have assumed a uniform basal melt rate. For instance, *Werder et al.* (2013) and *Hewitt et al.* (2012) use 0.1 and 0.6 cm a^{-1} respectively. *Hoffman et al.* (2016) calculate basal melt by assuming a characteristic basal traction of 0.1 MPa and geothermal heat flux of 0.06 W m^{-2}. Using these values, we calculate a basal melt rate of 2.4 cm a^{-1} corresponding to the average prescribed winter sliding speed used in synthetic experiments. In runs that include basal melt, we use values from 1 to 3 cm a^{-1}.

A possible drawback of using GlaDS in this study is its omission of sediment. Borehole measurements indicate that the drainage system under Isunnguata Sermia is characteristic of a hard bed (*Harper et al.*, 2017). Further south, *Dow et al.* (2013) find seismic evidence of sediment underlying Russel glacier. However, the spatial extent and thickness of till is largely unknown. Although not a proper substitute for till, the englacial aquifer modeled in GlaDS can also be interpreted as a relatively impermeable till aquifer (*Hewitt*, 2013). Other possible water sources such as groundwater are not considered here.

Our modeling approach is reminiscent of *Hoffman et al.* (2016) in that, although we model channels, we primarily focus on the dynamics of the distributed drainage system.

Several runs are conducted with channelization disabled. Moreover, we do not perform sensitivity tests on the channel parameters l_c and k_c as with other parameters and inputs.

Observations and modeling suggest that the current conceptual model of subglacial drainage may overemphasize the importance of channels (*Hoffman et al.*, 2016). Modeling studies indicate that muted surface slopes prevent significant channelization in the ice sheet interior (*Meierbachtol et al.*, 2013; *Dow et al.*, 2014, 2015) and that the channel system collapses in winter and starts anew every spring (*Hewitt*, 2013). Moulin water pressure measurements presented in *Andrews et al.* (2014) showed the presence of channels around 20km inland from the ice sheet terminus. However, nearby boreholes appeared to tap into regions of the bed hydraulically isolated from the channelized drainage system, suggesting that channels have a limited spatial influence.

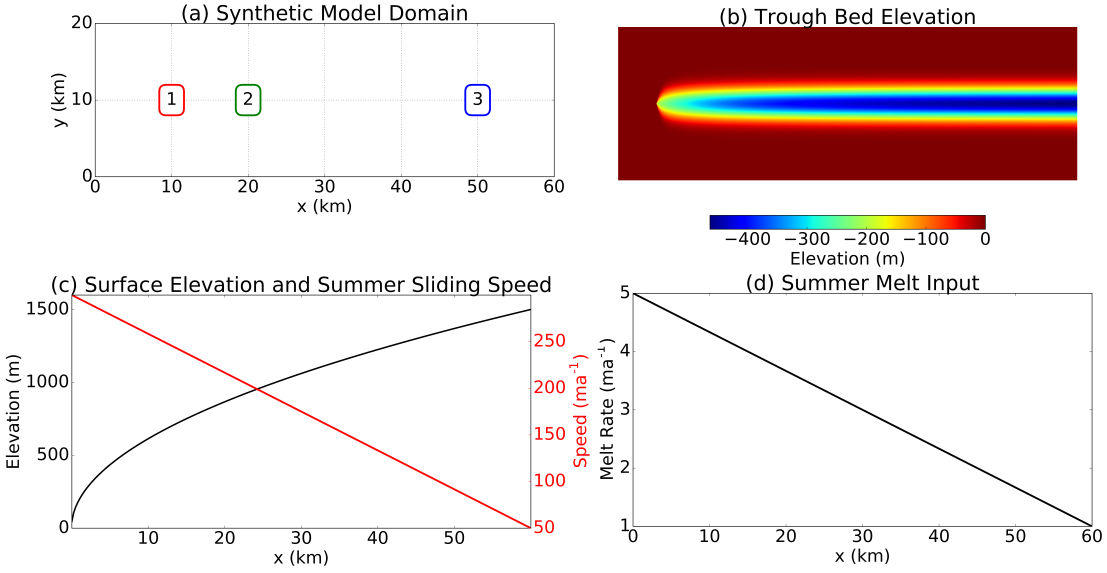

Figure 2.2: (a) 60 x 20 km rectangular model domain used in synthetic experiments. A zero pressure boundary condition is applied at the margin $x = 0$ and no flux at all other boundaries. SPV ratios are computed at reference points 1, 2, and 3. (b) Trough bedrock geometry used in some synthetic runs. (c) Surface elevation and summer sliding speed used in synthetic runs. (d) Summer melt input for synthetic runs.

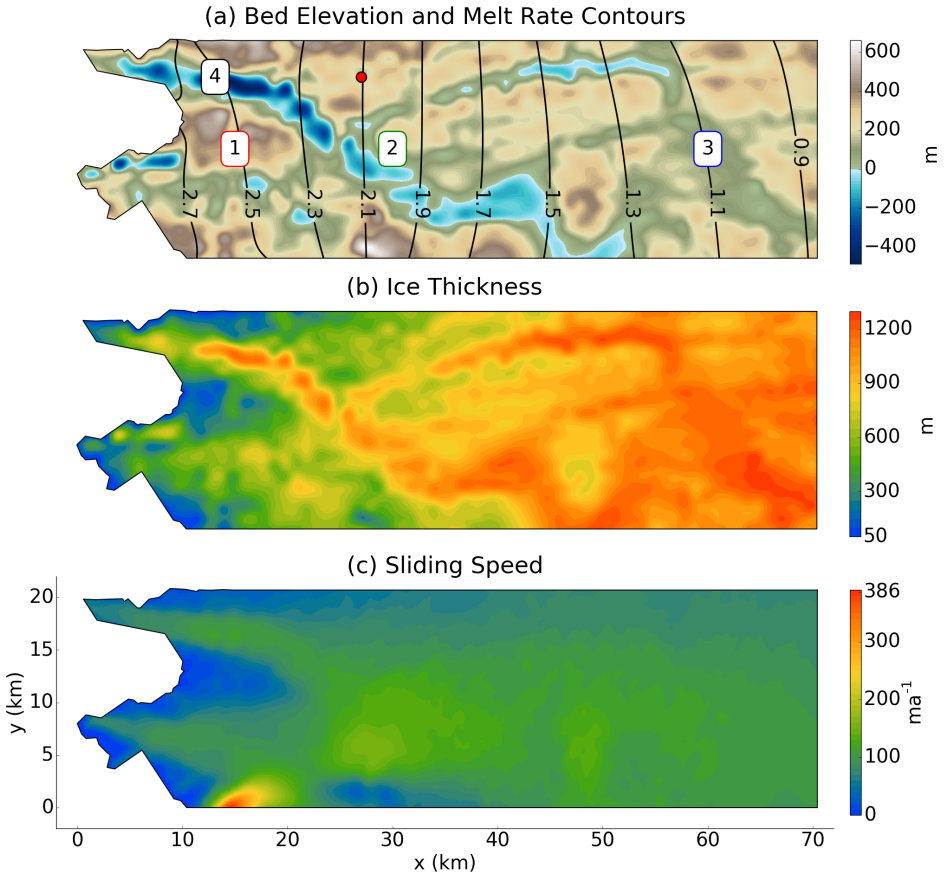

Figure 2.3: Model inputs for realistic runs on the Isunnguata Sermia / Russel Glacier area of western Greenland. Bed elevation and contours of summer melt input expressed in m a^{-1} are shown in (a). SPV ratios are calculated at reference points 1, 2, 3, and 4. The red dot indicates the location of borehole site 27km-12A, where water pressure data is plotted in Figure 2.1. Panels (b) and (c) show ice thickness and summer sliding speed respectively.

2.3 Numerical Experiments and Results

2.3.1 Reference Experiment

Here we simulate winter water pressure on a flat bed and synthetic trough with no channels or winter water sources. We use standard model parameters based on *Werder et al.* (2013) and *Schoof et al.* (2012). Default parameter values used in this experiment

can be found in Table 2.1. GlaDS significantly underpredicts winter water pressure in both runs (Table 2.2: row 1). Aggregation of water in the trough results in slightly higher winter pressure on a trough than a flat bed (Figure 2.4). SPV ratios range from 0.07 - 0.34 in the trough run versus 0.004 - 0.025 in the flat run.

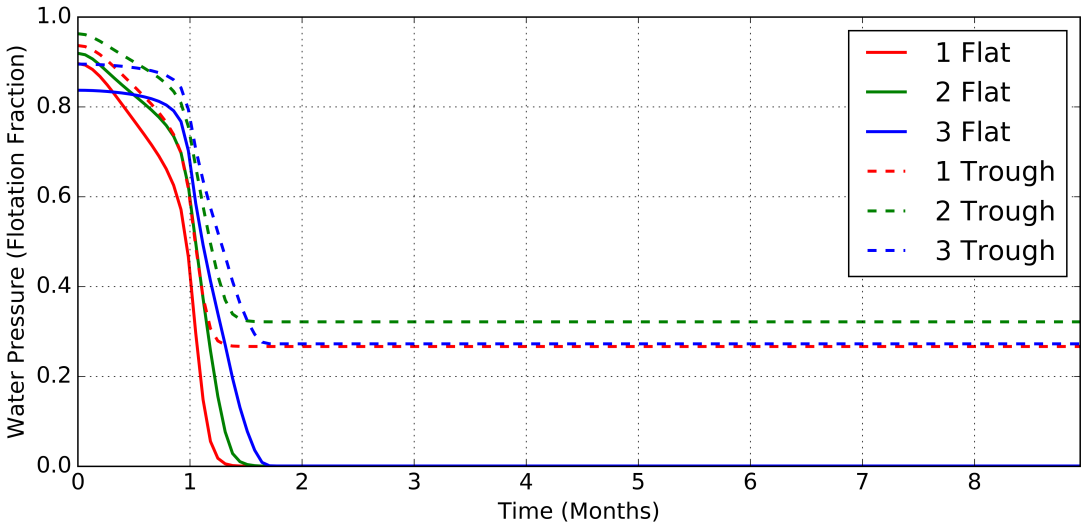

Figure 2.4: Time series showing synthetic winter water pressures at the three points in Figure 2.2a for the reference experiment with no channels or winter water sources. Time 0 denotes the end of summer, and month 1 marks the start of winter as described in the text. Solid and dashed lines show water pressures on a flat bed and trough respectively.

2.3.2 Sensitivity Experiments

The reference experiment reveals a significant disparity between modeled and observed winter water pressures. This problem could arise from inappropriate choices of several unconstrained parameters or from using simple, idealized model inputs. In this section, we investigate several factors that may contribute to low modeled winter water pressure through a series of sensitivity experiments. With the exception of the geometry sensitivity experiment, a synthetic trough geometry is used (Figure 2.2b). For each sensitivity experiment, we describe all parameters and inputs that are varied from the reference experiment. Additional details are are provided in appendix Table 2.B.1.

- **Sliding Speed**

  Sliding speed u_b enters the cavity opening term in equation 2.1. Imposing a slower winter sliding speed might restrict cavity opening and increase winter water pressure. To test this idea, we conduct six runs with a fast, moderate, or slow summer sliding speed in combination with a fast or slow winter sliding speed. The moderate summer sliding speed is equivalent to that used in the reference experiment (Figure 2.2c). Fast and slow summer speeds are 33% faster and slower respectively. Sliding speed is scaled so that the maximum winter value is 100 m a^{-1} in fast winter runs and only 5 m a^{-1} in slow winter runs, which should maximize the negative feedback between sliding speed and water pressure noted by *Hoffman and Price* (2014).

- **Bump Height**

  As with sliding speed, characteristic bump height and bump length parameters h_r and l_r enter the cavity opening term in Equation 2.1, which may affect winter water pressure. We found that the model was insensitive to l_r values between 1 and 5 m and do not include these runs in Table 2.2. Listed values span the range of bedrock bump parameters used in *Schoof et al.* (2012), *Werder et al.* (2013), *Hoffman and Price* (2014), *Hewitt* (2013), and *Bueler and Van Pelt* (2015).

- **Rate Factor**

  The rate factor A influences the rate of creep closure in Equation 2.1. Rapid cavity closure corresponding to a large rate factor could increase winter water pressure. We test the minimum and maximum suggested rate factors of 2.4 and 9.3×10^{-24}

Pa^{-3} s^{-1} listed in *Cuffey and Patterson* (2010) for temperate ice.

- **Channels**

The interplay between channelized and distributed drainage may play an important role in controlling winter water pressure. The absence of channels in the reference experiment may mean the model is tuned in a way that overestimates the efficiency of the distributed system. To investigate this possibility, we perform a run with channelized drainage enabled and default values for k_c and l_c taken from *Werder et al.* (2013) (Table 2.1).

- **Realistic Geometry**

The reference experiment shows that aggregation of water in a trough produces higher winter water pressure. This effect could be more pronounced in troughs and other complex features in realistic bedrock geometry. To test this, we perform a run with realistic inputs from the Isunnguata Sermia / Russel Glacier region of Greenland. Several additional runs were performed testing variations in summer and winter sliding speed, following the same approach as the sliding sensitivity experiment. Results were fundamentally similar to the test on synthetic geometry and are therefore excluded from Table 2.2.

- **Englacial Storage**

Winter water sources, although small compared to surface melt input, could boost winter water pressure. Here we introduce a source term from an englacial aquifer. We test low, medium, and high englacial void ratios e_v of 10^{-4}, 10^{-3} and 10^{-2}. Including the reference experiment, where $e_v = 0$, this comprises the range of void ratio values compiled in *Hewitt* (2013) from previous modeling studies.

- **Basal Melt**

  Steady basal melt may enhance the sensitivity of winter pressure to other inputs or parameters. We repeat several runs from previous sensitivity experiments with a uniform basal melt rate of 3 cm per year. In particular, we repeat the reference experiment, the moderate summer sliding to slow winter sliding run in the sliding sensitivity experiment, the 1m bump height run in the bump sensitivity experiment, the high rate factor run in the rate factor sensitivity experiment, and the realistic geometry experiment. An additional run combining channels, basal melt, and englacial storage is also presented in Section 2.3.3.

- **Hydraulic Conductivity**

  Hydraulic conductivity is a complex and poorly constrained parameter that depends on the subgrid scale geometry of the linked cavity system. In this experiment we allow for spatially and temporally varying conductivity by scaling conductivity linearly with melt input according to

$$k = \left(\frac{k_{max} - k_{min}}{\max(m)} \right) m(x, y, t - l) + k_{min} \tag{2.14}$$

  Conductivity is tuned by setting the parameters k_{min} and k_{max}, which represent the maximum summer and minimum winter conductivities respectively. Conceptu-

ally, we envision that reduced melt input in winter causes subgrid scale geometric changes to the linked cavity system that reduce hydraulic conductivity. The physical basis for changing hydraulic conductivity is discussed extensively in Section 2.4.2. We conduct one run in which conductivity begins to decrease immediately as melt decreases, as well as a second run in which the decrease in conductivity is delayed by six hours (represented by the lag time parameter l in equation 2.14).

Results

SPV ratios for all sensitivity experiments are summarized in Table 2.2. Winter water pressure is relatively insensitive to sliding speed, bump height, bump length, and rate factor (Table 2.2: rows 3, 5, and 7). Even an implausibly low winter sliding speed (≤ 5 m a^{-1}) results in only a minor increase in winter water pressure. Examining equation 2.1 shows that changing the characteristic bump length l_r amounts to rescaling sliding speed, and it too has little effect. Similarly, using a large rate factor in the creep closure relation only marginally increases winter water pressure.

Large bump heights lead to moderately higher winter water pressure. SPV ratios are highest in the 2m bump height run, ranging from 0.46 - 0.72. Tall bedrock bumps cause large cavities to develop, reducing summer water pressure. Low conductivity values are necessary to compensate and obtain high summer water pressure consistent with borehole observations. Cavities collapse rapidly during the fall as surface melt input decreases. The drainage system thus transitions to an inefficient state with small, low-conductivity cavities during the winter, which helps bolster water pressure.

Although the 2 m bump height run has the highest winter water pressure, it is perhaps the least physically plausible. At the end of summer, sheet height is around 1.4 m on average, extending up to around 2 m in places. Since sheet height is a spatial average, and water is not distributed uniformly at the bed, this would imply the existence of multi-meter tall cavities.

As with using a large bump height, adding channelized drainage improves the efficiency of the drainage system in summer and requires lower conductivity values to elevate summer water pressure. Conductivity is around five times smaller in the channel sensitivity experiment than the reference experiment (10^{-3} versus 5×10^{-3} $m^{\frac{7}{4}}$ $kg^{-\frac{1}{2}}$). In summer, channels have the greatest influence on water pressure within around 15 km of the glacier terminus. The largest channels nucleate at the snout of the bedrock trough near test point 1. As channels collapse in the fall, the efficiency of the drainage system decreases, which helps maintain slightly higher winter water pressure (Table 2.2: row 9).

Introducing realistic bedrock geometry results in a heterogeneous water pressure field, with high winter pressure in bedrock troughs and low pressure elsewhere. Winter water pressure remains high at reference point 4, but plummets at reference points 1-3 (Figure 2.5). Elevated water pressure in bedrock troughs yields overall higher winter water pressure compared to the reference experiment (Table 2.2: row 11).

Winter water sources can significantly contribute to higher modeled winter water pressure (Table 2.2: rows 2, 4, 6, 8, 10, 12, 13). Drainage from the englacial aquifer matches or exceeds basal melt for all tested void ratios. Water drains from the englacial aquifer at rates of around 4 cm a $^{-1}$ and 24 cm a^{-1} for void ratios of 10^{-4} and 10^{-3} respectively. For a void ratio of 10^{-2}, water drains at a rate of nearly 1 m a^{-1}, producing relatively high water pressure through the winter with SPV ratios ranging from 0.9 - 0.98. However, observations of temperate layer thickness presented in *Harrington et al.* (2015) cast doubt on this result, suggesting that the model overpredicts storage at high void ratios. This is discussed further in Section 2.4.1.

Variable hydraulic conductivity yields high winter pressure with all SPV ratios near 1 (Table 2.2: row 14). If there is no delay between decreased melt input and reduced conductivity, water pressure rises during the fall then gradually declines through the winter (Figure 2.6). Although we are only attempting to broadly reproduce observations by obtaining similar summer and winter water pressure, this spike in pressure is not

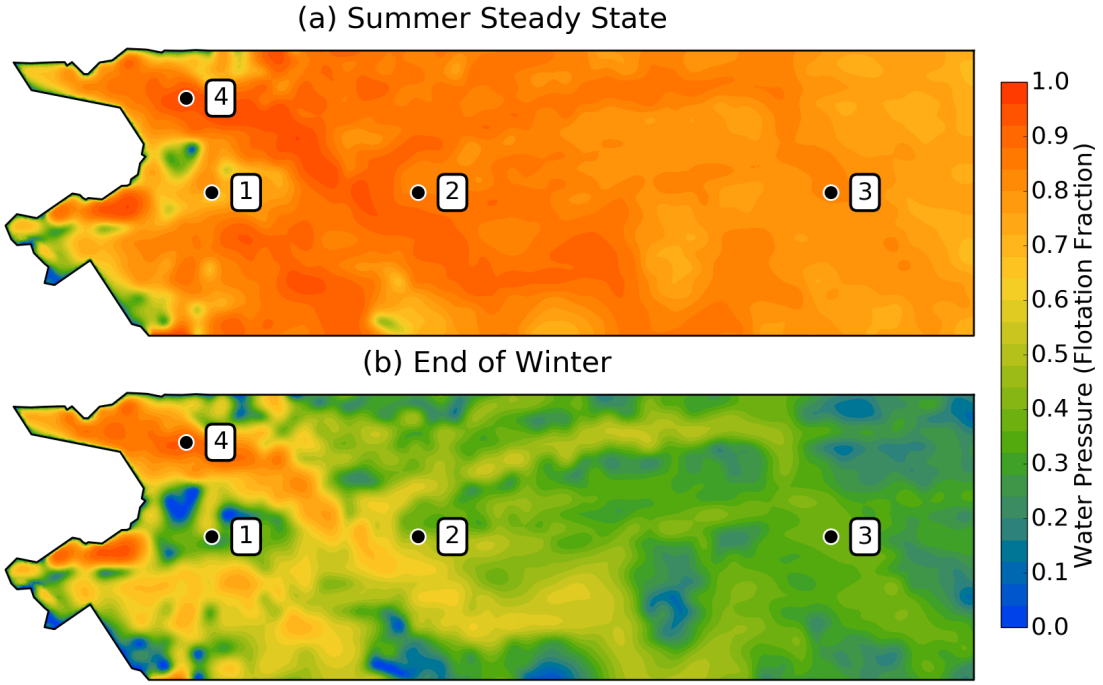

Figure 2.5: Summer steady state (a) and end of winter (b) water pressure on the realistic topography of Isunnguata Sermia. SPV ratios calculated at points 1-4 are reported in Table 2.2: row 11.

necessarily consistent with observations and biases SPV ratios due to high water pressure in early winter. Delaying the response of conductivity to decreased melt by 6 hours mitigates this spike, resulting in steadier water water pressure through fall and winter.

In the conductivity sensitivity experiment, we use a value of 5×10^{-7} $\mathrm{m}^{\frac{7}{4}}$ $\mathrm{kg}^{-\frac{1}{2}}$ for k_{min} and 8×10^{-3} $\mathrm{m}^{\frac{7}{4}}$ $\mathrm{kg}^{-\frac{1}{2}}$ for k_{max} – a range of four orders of magnitude. In principle, the gradual decline of winter water pressure could be prevented by imposing a lower winter conductivity k_{min}. We have found this approach impractical since imposing a very low conductivity value on the order of 10^{-8} $\mathrm{m}^{\frac{7}{4}}$ $\mathrm{kg}^{-\frac{1}{2}}$ leads to numerical instability. Alternatively, combining a winter water source with variable conductivity leads to level winter water pressure as shown in the next section.

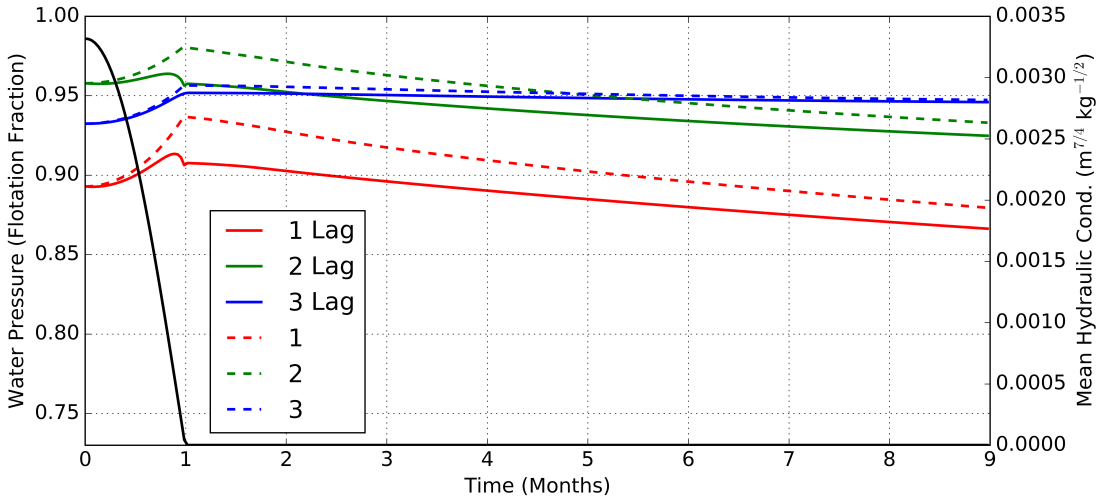

Figure 2.6: Time series of winter water pressures at the three points in Figure 2.2a for two runs using variable hydraulic conductivity. Dashed lines show water pressures for a run where conductivity begins decreasing immediately with surface melt input. Solid lines show pressures for a run where conductivity begins decreasing six hours after melt. The solid black line shows the geometric mean conductivity for the run with no lag in conductivity.

2.3.3 Combination Experiments

High winter water pressure is likely caused by multiple interacting physical processes rather than a single process such as englacial storage or changing conductivity. Although exploring all combinations of parameters and inputs is intractable, we will examine two more complex scenarios, motivated by the results of the sensitivity experiments. In the first experiment, we test the idea that high winter pressure might result from a combination of collapsing channels and winter water sources as opposed to changing efficiency in the distributed drainage system. In the second experiment, we test variable hydraulic conductivity in a more realistic context.

- **Channels + Winter Water Sources**

  Sensitivity experiments show that channelized drainage, basal melt, and englacial storage all contribute to higher winter water pressure. The combination of all three

may be able to reproduce winter water pressure observations. We perform a run with channelized drainage enabled, a void ratio 10^{-3}, and a uniform basal melt rate of 1 cm a^{-1}. Due to the difficulty of simulating channels on realistic geometry, we use a synthetic trough geometry.

- **Variable Conductivity + Realistic Geometry**

  Variable hydraulic conductivity broadly reproduces winter water pressure observations in the conductivity sensitivity experiment. Here, we apply variable hydraulic conductivity to realistic bedrock geometry to verify that results are similar. We perform a run with conductivity determined by equation 2.14, lag time $l = 0$, and a void ratio of 10^{-4}.

Results

In the channels + winter water sources experiment (Figure 2.7, Table 2.2: row 10), winter water pressure declines relatively slowly, but drops considerably by the end of winter. The englacial aquifer serves as the primary winter water source, draining at a rate of around 16 cm a^{-1}.

Applying variable conductivity to realistic geometry yields similar results to the conductivity sensitivity experiment, with a few noteworthy differences (Table 2.2: row 15). While the maximum summer conductivity k_{max} is essentially the same as in the conductivity sensitivity experiment, the minimum winter conductivity k_{min} is an order of magnitude larger. Rising water pressure during the fall is counteracted by intake of water into the englacial aquifer. Although the decrease in conductivity is not delayed, water pressure does not spike during the fall as in the conductivity sensitivity experiment (Figure 2.8). Water is released from the englacial aquifer at around 3 cm a^{-1} through the winter. Low conductivity combined with a small winter water source yields nearly static winter water pressure.

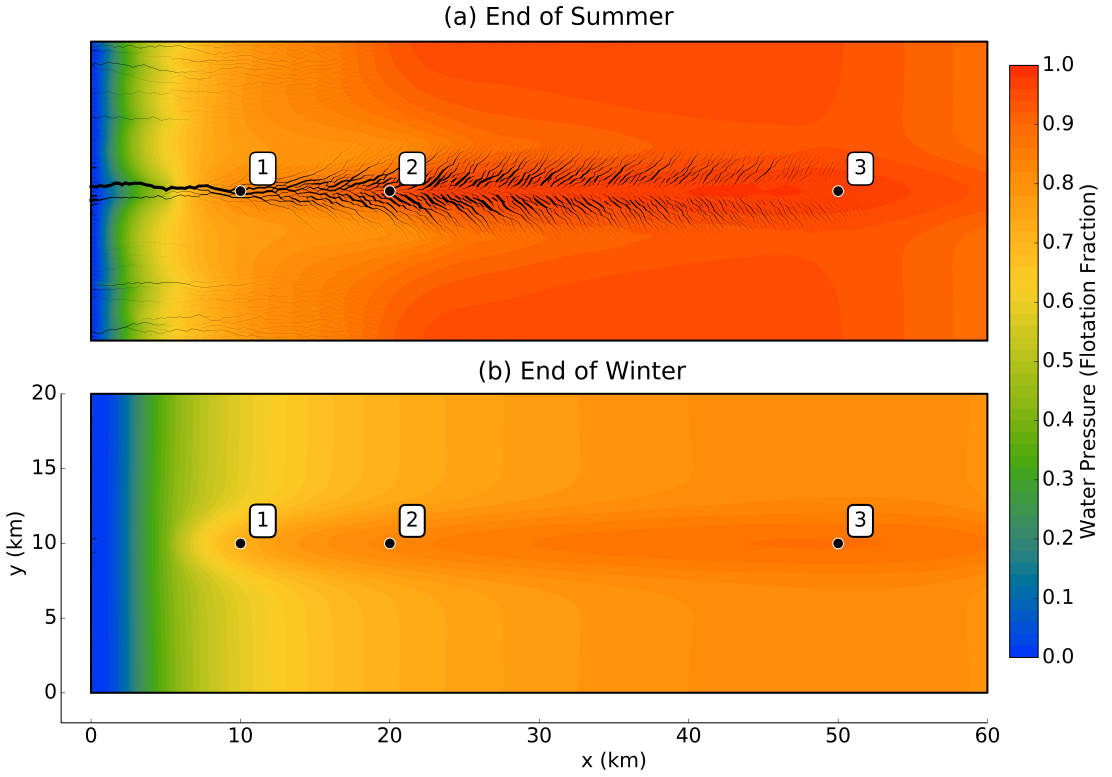

Figure 2.7: End of summer (a) and end of winter (b) water pressure on a synthetic trough geometry with channels, basal melt, and englacial storage. Black lines represent channel locations. Line weight is proportional to the cross-sectional area of the channel. In summer, the maximum channel-cross sectional area is 40 m^2. By the end of winter, the channel system is nearly nonexistent.

2.4 Discussion

Consistent with previous findings (e.g *Werder et al.*, 2013), sensitivity experiments demonstrate that GlaDS underpredicts winter water pressure observations given a wide range of inputs and parameter values. Moreover, they help isolate two general processes that contribute to higher modeled winter water pressure. Numerical experiments suggest that water sources such as englacial storage and, to a lesser extent, basal melt may significantly elevate winter water pressure. A sufficiently large englacial water source alone could potentially explain high winter water pressure, however this likely requires more storage than observations suggest possible. This is discussed further in Section

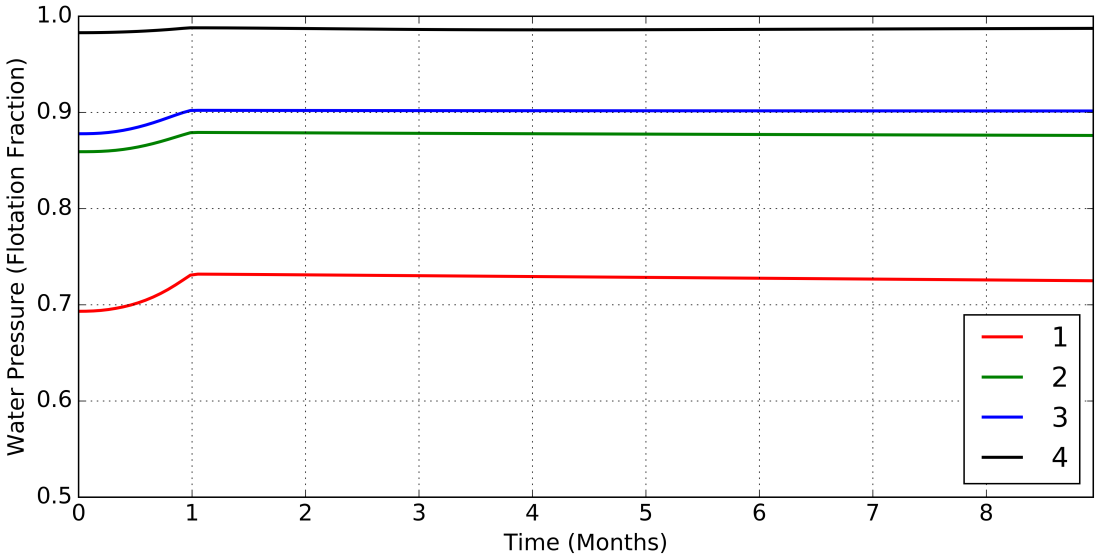

Figure 2.8: Time series of water pressures at the four points in Figure 2.3a for a run with realistic geometry, variable conductivity, and englacial storage.

Table 2.2: Each row displays minimum and maximum SPV ratios for all runs in a single experiment. SPV ratios are calculated at the three reference points in Figure 2.2a for synthetic runs and the four reference points in Figure 2.3a for realistic runs. The domain wide SPV value is also reported in the domain column. SPV ratios exceeding 0.9 are displayed in red, while SPV values over 0.95 are also bolded.

	Experminent	**Domain**	**Point 1**	**Point 2**	**Point 3**	**Point 4**
1	**Reference**	0.01 - 0.07	0.00 - 0.28	0.01 - 0.34	0.02 - 0.32	-
2	**+ Basal Melt**	0.57	0.43	0.65	0.84	-
3	**Sliding**	0.091 - 0.095	0.28 - 0.29	0.34 - 0.35	0.33 - 0.34	-
4	**+ Basal Melt**	0.91	0.84	0.91	**1.02**	-
5	**Bump Height**	0.06 - 0.49	0.28 - 0.46	0.33 - 0.61	0.31 - 0.72	-
6	**+ Basal Melt**	0.64	0.55	0.71	0.86	-
7	**Rate Factor**	0.07-0.10	0.28-0.30	0.33-0.36	0.33-0.35	-
8	**+ Basal Melt**	0.61	0.49	0.70	0.85	-
9	**Channels**	0.146	0.35	0.38	0.36	-
10	**+ Water Sources**	0.87	0.92	0.89	0.92	-
11	**Realistic Geometry**	0.50	0.50	0.54	0.46	0.92
12	**+ Basal Melt**	0.74	0.53	0.69	0.82	0.93
13	**Englacial Storage**	0.56 - 0.90	0.44 - 0.86	0.64 - 0.91	0.83 - **0.98**	-
14	**Variable Conductivity**	**0.99** - **1.01**	**0.99** - **1.01**	**0.98** - **0.99**	**1.01** - **1.02**	-
15	**+ Realistic Geometry**	**1.03**	**1.05**	**1.02**	**1.02**	**1.00**

2.4.1.

The second major process contributing to higher modeled winter water pressure is reduced efficiency of the drainage system during the fall and winter. It is unsurprising that slower winter sliding, collapsing channels, and shrinking cavities contribute to higher winter water pressure. Perhaps not intuitively obvious is that these processes do not offset the drop in modeled winter water pressure caused by surface melt shut off. Although channels collapse and cavities shrink in winter, the drainage system can still easily accommodate the limited water supply from englacial storage and basal melt.

Changing hydraulic conductivity is another plausible reason for changes in drainage system efficiency. As surface melt input decreases, connections between cavities likely close, reducing hydraulic conductivity by restricting the flow of water. In the model, reducing hydraulic conductivity during the fall can broadly reproduce observations either in isolation or alongside other processes like englacial storage. The physical basis for variable hydraulic conductivity is discussed in Section 2.4.2.

2.4.1 Englacial Storage

Numerical experiments indicate that englacial storage could act as a significant winter water source. In numerical experiments, drainage from the englacial aquifer at least matched and in some cases eclipsed basal melt depending on the value of the englacial void ratio parameter. Larger void ratios result in more summer water storage, faster drainage from the englacial aquifer during winter, and higher winter water pressure. In theory, imposing a void ratio in excess of 1% might yield water pressure close to observations. Here, we will consider if a void ratio of this magnitude is physically plausible.

In numerical simulations, the depth averaged englacial water content at the end of summer essentially matched the englacial void ratio. For large void ratios, this equates to a substantial volume of englacial water. For example, in the 1% void ratio run in

the englacial storage sensitivity experiment, the effective water layer thickness in the englacial aquifer was an average of 7 m at the end of summer, reaching up to 18 m in the interior.

Observations suggest that a depth averaged englacial water content of 1% is implausibly high in the interior. Temperature measurements from three boreholes 27, 27.1, and 45.5 km from the terminus of Isunnguata Sermia showed a temperate layer thickness of around 100 m at the first two sites and 20 m at the third site (*Harrington et al.*, 2015). Average water content in a transect spanning the first two sites was estimated at around 0.5 - 1.1% (*Brown et al.*, 2017). Water was mostly concentrated in the temperate layer, which had an estimated water content of 2.9-4.6%. If, as observations suggest, there is a 20 m thick temperate layer deeper in the interior with a similar 5% water content, then the overall depth averaged water content there is only 0.06% (assuming an ice thickness of 1500 m). Hence, the model probably vastly overestimates englacial storage in the interior for a 1% void ratio.

It is also important to note the difference between englacial void ratio, which represents water bearing void spaces such as basal crevasses with a direct, no-resistance connection to the bed, and englacial water content, which includes water isolated from the bed that has no impact on winter water pressure. *Hewitt* (2013) uses a void ratio of 10^{-4}, arguing that while a higher void ratio may be appropriate, it is unlikely that englacial void spaces are all well connected to the bed as assumed by the model. A better approach to modeling englacial storage might be to limit the amount of englacial storage based on observations of temperate layer thickness or to model the englacial aquifer as a separate drainage component as in *Flowers and Clarke* (2002).

Since englacial storage is proportional to void ratio, results are more plausible for lower void ratios. Low hydraulic conductivity and, to a certain extent, slower winter sliding enhance the sensitivity of the model to a smaller englacial water source corresponding to a lower void ratio. This is reflected in the channels + winter water sources

experiment (Table 2.2: row 10) where low conductivity and englacial storage produce relatively high winter water pressure. Nonetheless, this combination was not sufficient to match winter water pressure observations.

2.4.2 Physical Interpretation of Variable Conductivity

Our results support the idea that high winter water pressure is at least partially caused by decreasing efficiency of the distributed drainage system due to reduced hydraulic conductivity. Given the lack of constraints on hydraulic conductivity and its past use as a tuning parameter, it is perhaps unsurprising that it can be manipulated to reproduce winter water pressure observations. Beyond its effectiveness in numerical experiments, there is a good physical basis for varying hydraulic conductivity.

Broadly speaking, hydraulic conductivity determines how easily water flows through the linked cavity system. It is useful to motivate its role by considering the case where $\beta = 2$ and $\alpha = 1$ in which flux equation 2.6 simplifies to Darcy's law for laminar flow through a porous medium

$$\mathbf{q} = -kh_w \nabla \phi. \tag{2.15}$$

In Darcy's law, hydraulic conductivity can be written as $k = \frac{k_0}{\eta}$ where k_0 is the intrinsic permeability of the porous medium and η is the viscosity of the fluid. Increasing fluid viscosity or decreasing permeability increases flow resistance.

More generally, k may depend on the geometry of the local drainage system. For example, *Clarke* (1996) presents a flux relation for laminar flow through parallel plates

$$\mathbf{q} = -\frac{w}{12\eta l} h_w^3 \nabla \phi \tag{2.16}$$

where w is the cross-flow width of the sheet and l is the along flow length. *Hewitt* (2011) uses this flux relation in a precursor to the linked cavity model in GlaDS, writing it in

a form resembling Darcy's law:

$$\mathbf{q} = -\frac{k_0}{\eta} h_w^3 \nabla\phi = -k h_w^3 \nabla\phi \tag{2.17}$$

Here, $k_0 = \frac{w}{12l}$ is a geometric factor. We can think of $k = \frac{k_0}{\eta}$ as analogous to the hydraulic conductivity familiar from Darcy's law, bearing in mind that its precise physical meaning is different since it depends on drainage system geometry rather than the permeability of a porous medium.

Similarly, in GlaDS, hydraulic conductivity k depends on the complex subgrid scale geometry of the linked cavity system and bedrock. Equation 2.6 describes aggregate flow over a patch of the bed containing a complex network of interconnected cavities. As sources of water diminish, the conductivity of the linked cavity system may decrease due to closing links or other geometric changes that reduce connectivity between cavities. Changing connectivity is a subgrid scale phenomenon that cannot be resolved by the model. However, the net effect is to reduce the bulk hydraulic conductivity.

Our approach of adjusting hydraulic conductivity may compensate for physics describing the seasonal evolution of orifices neglected in current continuum models. Conceptually, it is the orifices linking cavities that dictate water flux through the distributed system (*Kamb*, 1987). A critical assumption in *Schoof et al.* (2012) is that orifice size, and thus discharge, scales with cavity size. This is fundamentally different from the foundational linked cavity models such as *Kamb* (1987) and *Fowler* (1987) that assume orifices behave like small R-channels, opening in part due to thermal effects. *Schoof et al.* (2012) attempt to incorporate viscous heat dissipation in a continuum model formulation, but show that it leads to unstable channelization.

While it is not clear how the subgrid scale thermal processes controlling orifice evolution should be treated in continuum models, their neglect could be responsible for the disagreement between observed and modeled winter water pressure. A reduction

in water sources at the end of the melt season limits orifice growth, while creep closure leads to loss of connectivity between cavities. Because these processes are not considered in GlaDS, it may overpredict discharge through the linked cavity system, even as the average cavity height decreases in winter, since orifices rather than cavities determine discharge. Thus, omitted physics for orifices may lead to low modeled winter water pressure.

Scaling conductivity linearly with melt input as in equation 2.14 is a pragmatic way to sidestep the complicated issue of modeling orifice evolution. We do not mean to imply a direct relationship between melt and conductivity but that variations in melt input cause subgrid scale changes in connectivity that in turn reduce conductivity.

This ad hoc relationship works well given ideal melt forcing, but may not be suitable for a more realistic melt forcing. Given our emphasis on winter water pressure, we have focused on the transition from summer to winter. However, hydraulic conductivity necessarily increases during the spring, and it is not clear if our simple relationship works in this situation either. This relationship will hopefully be improved upon in future research by using a dynamic expression for conductivity relating it to other model unknowns. One precedent is provided by *Flowers and Clarke* (2002) who employ a sheet height dependent conductivity for a porous sediment layer.

Constraining the change in conductivity in winter is problematic due to uncertainties in other inputs and parameters, particularly in the magnitude of winter water sources. If only a small winter water source is introduced, a change in conductivity of several orders of magnitude is required to match winter water pressure observations using the model. Unsurprisingly, a large winter water source requires a much smaller change in conductivity. While it is highly plausible that reduced hydraulic conductivity is a primary cause of high winter water pressure, it is difficult to confirm or refute this possibility without more precise constraints on winter water sources.

2.4.3 Relation to Previous Modeling Studies

Previous publications acknowledged the problem of low modeled winter pressure, and more generally, other problems associated with imposing constant hydraulic conductivity. *Werder et al.* (2013) discuss the tendency of GlaDS to predict low water pressure at low discharge as well as the idea that portions of the bed may become hydraulically disconnected in winter. This idea is supported in a mountain glacier setting by a study of Trapridge Glacier, where regions of the subglaical hydraulic system have been found to switch back and forth between hydraulically connected or disconnected (*Murray and Clarke*, 1995).

Hewitt (2013) describes the difficulty of selecting a single conductivity value that yields plausible behavior through multiple seasons. Setting conductivity too low can cause excessively high water pressure in spring, while setting conductivity too high results in low water pressure in winter. We observed similar behavior. In runs with channelized drainage, conductivity was tuned low to produce high water pressure at the end of summer. Since water pressure constraints were not enforced in these runs, water pressure in early summer significantly exceeded overburden pressure before the channel network was well developed.

Our work bears some resemblance to a modeling study by *Hoffman et al.* (2016) who attempt to explain observations at drill site FOXX in western Greenland (see e.g. *Andrews et al.* (2014)) using a subglacial hydrology model with a distributed component similar to GlaDS, but only a single prescribed channel. Observations at FOXX showed declining ice speed in late summer despite relatively stable water pressure in moulins feeding subglacial channels. At the same time, water pressure in boreholes tapping into weakly connected areas of the bed experienced a slight decline in water pressure. *Hoffman et al.* (2016) show that these observations can be explained in the numerical model by introducing a new weakly connected component in addition to the usual distributed and channelized components.

As in *Hoffman et al.* (2016), we appeal to subgrid scale phenomena and time variable conductivity to explain observations using a numerical model. *Hoffman et al.* (2016) conceptualized weakly connected patches of the bed that occupy a fraction of each grid cell. Weakly connected areas essentially act as storage reservoirs that have no internal flux but exchange water with the distributed system. The rate of exchange is related to a conductivity parameter that represents the connectivity between the weakly connected and distributed system. *Hoffman et al.* (2016) find that by increasing this conductivity parameter in late summer, they are able to reproduce observations of gradually declining water pressure in the weakly connected system.

Despite these similarities, there are some important differences between our study and *Hoffman et al.* (2016). For one, we focus on explaining observations in winter versus late summer. Secondly, we make no distinction between the weakly connected system and the regular distributed system, but consider connectivity as existing on a continuous spectrum. *Hoffman et al.* (2016) reason that they might be able to achieve similar results using a spatially varying conductivity on a fine grid scale – that is by imposing low conductivity in weakly connected areas of the bed and higher conductivity elsewhere.

2.5 Conclusions

In accordance with previous modeling studies, we found that GlaDS significantly underpredicts water pressure observations in winter. This problem persisted for a wide range of seemingly plausible parameter values and model inputs. To our knowledge, we are the first to focus narrowly on the problem of low modeled winter pressure in the context of a linked cavity model and on the physical interpretation of conductivity as a proxy for drainage system connectivity.

Sensitivity experiments indicated that englacial storage and variable hydraulic con-

ductivity are the dominant controls on modeled winter water pressure. We found that englacial storage significantly elevated winter water pressure for high values of the englacial void ratio parameter. However, measurements of temperate layer thickness and estimates of englacial water content from western GrIS demonstrated that englacial storage is likely limited in the ice sheet interior. For the large void ratio values needed to obtain high winter water pressure, the model predicted an implausibly high volume of englacial water in the interior.

We found that the discrepancy between modeled and observed winter water pressures could be resolved by decreasing hydraulic conductivity during the fall. Variable conductivity was used to reproduce winter water pressure observations in isolation and in conjunction with other processes like englacial storage. Examining the physical meaning of hydraulic conductivity in a linked cavity model, we concluded that decreasing hydraulic conductivity reflects reduced subgrid scale connectivity of the linked cavity system during the fall.

Variable hydraulic conductivity in the distributed system may be a critical process neglected by current generation continuum models. Future work is needed to better understand the physics controlling hydraulic conductivity and determine its functional form in terms of other model unknowns including sheet thickness and water pressure. Discrete, small scale models simulating individual cavities (e.g. *Schoof* (2010)) may prove useful, so long as results can be generalized to large scale continuum models.

Appendices

2.A Numerical Solution

We have implemented GlaDS in FEniCS, a finite element package callable from C++ or Python (*Alnaes et al.*, 2015). Continuous variables including ϕ and h are discretized using linear Lagrange finite elements. Channel related fields are discretized using discontinuous Lagrange trace elements. Time stepping involves solving for ϕ with h and S fixed, then advancing h and S with ϕ fixed. As in *Werder et al.* (2013), we solve for ϕ by expressing equations 2.12 and 2.13 in weak form and adding them to arrive at a single equation in weak form that can be solved by FEniCS. The resulting equation is solved using either Newton's method or, optionally, using PETSc's SNESVI solver which enforces constraints on water pressure. The time derivative in the storage term is discretized using the implicit Euler method. Equations 2.1 and 2.7 are solved using petsc4py with a 5th order Runge-Kutta method.

2.B Details of Model Experiments

In each model experiment, melt input takes the form

$$m = m_s(t)\,\hat{m}(x, y) + m_b$$

where $\hat{m}$ is the summer melt input, m_b is some constant basal melt, and m_s is a scaling function defined by

$$m_s(t) = \max\left(\cos\left(\frac{\pi t}{2t_o}\right), 0\right). \tag{2.18}$$

Here, t_o is a shut off time parameter that controls when surface melt input to the bed ceases. We use a fixed shut off time of one month in all simulations. Similarly, sliding speed takes the form

$$u_b = u_s(t)\,\hat{u_b}(x, y) \tag{2.19}$$

where $\hat{u_b}$ is the summer sliding speed and u_s is a scaling function defined by

$$u_s(t) = m_s(t)\left(1 - \frac{u_{max}}{\max(\hat{u_b})}\right) + \frac{u_{max}}{\max(\hat{u_b})}. \tag{2.20}$$

u_{max} is the maximum desired winter sliding speed. When $m_s(t) = 1$, $u_b = \hat{u_b}$ and when $m_s(t) = 0$ the maximum value of u_b at any point is u_{max}.

By default all experiments use the parameter values listed in Table 2.1, synthetic experiments use the model inputs displayed in Figure 2.2, and realistic experiments use the inputs displayed in Figure 2.3. A summary of inputs and parameters varied in each sensitivity experiment is provided below.

Table 2.B.1: Varied parameter values and inputs used in each model experiment.

Experiment	**Varied Parameters / Inputs**
Reference + Basal Melt	Basal melt $m_b = 3$ cm a^{-1}
Sliding	Summer sliding speed $\hat{u_b}$ ranges from 0.66 u_{bs} - 1.33u_{bs} where u_{bs} is the synthetic summer melt input function shown in Figure 2.2. Maximum winter sliding speed u_{max} ranges from 5 - 100 ma^{-1}.
Bump Height	Bump height h_r ranges from 5 - 200 cm.
Bump Height + Basal Melt	Bump height $h_r = 100$ cm. Basal melt $m_b = 3$ cma^{-1}.
Rate Factor	Rate factor A ranges from 2.4 to 9.3×10^{-24} Pa^{-3} s^{-1}.
Rate Factor + Basal Melt	Rate factor $A = 9.3 \times 10^{-24}$ Pa^{-3} s^{-1}. Basal melt $m_b = 3$ cm a^{-1}.
Channels	Channelization is enabled.
Channels + Water Sources	Channelization is enabled, basal melt $m_b = 1$ cm a^{-1}, and void ratio $e_v = 10^{-3}$.
Realistic Geometry	Uses realistic inputs shown in Figure 2.3.
Realistic Geometry + Basal Melt	Uses realistic inputs shown in Figure 2.3. Basal melt $m_b = 3$ cm a^{-1}.
Englacial Storage	Void ratio e_v ranges from 10^{-4} to 10^{-2}.
Variable Conductivity	Conductivity is determined by Equation 2.14. Lag time l ranges from 0 - 6 hours.
Variable Conductivity + Realistic Geometry	Uses realistic inputs shown in Figure 2.3. Conductivity is determined by Equation 2.14 with lag time $l = 0$.

Table 2.B.2: Range of tuned conductivity values used in each experiment.

Experiment	k / k_{max} $(m^{\frac{7}{4}} kg^{-\frac{1}{2}})$
Reference	4.41 - 4.48 $\times 10^{-3}$
Sliding	4.2 - 4.8 $\times 10^{-3}$
Bump Height	10^{-4} - 10^{-2}
Rate Factor	4.1 - 5 $\times 10^{-3}$
Channels	10^{-3}
Realistic Geometry	4×10^{-3}
Englacial Storage	4.4 $\times 10^{-3}$
Variable Conductivity	5 $\times 10^{-3}$
Variable Conductivity + Realistic Geometry	5 $\times 10^{-3}$

Code Repository

Our implementation of GlaDS used in this work is available at `https://github.com/JacobDowns/ChannelModel/`.

Acknowledgements

J. Z. Downs was supported by NSF grant 1543533. J. Z. Downs and J. V. Johnson were supported by NSF grant 1504457. We would like to thank editor Bryn Hubbard and five anonymous reviewers for their comments, which greatly improved the quality of this manuscript. Thanks to Douglas Brinkerhoff for many meaningful discussions and for providing code that served as the starting point for our implementation of GlaDS. Thanks also to Ed Bueler and Christian Schoof for answering a number of modeling related questions in earlier iterations of this work.

Bibliography

Alnaes, M. S., J. Blechta, J. Hake, A. Johansson, B. Kehlet, A. Logg, C. Richardson, J. Ring, M. E. Rognes, and G. N. Wells (2015), The FEniCS Project Version 1.5, *Archive of Numerical Software*, *3*(100), 9–23, doi:10.11588/ans.2015.100.20553.

Andrews, L. C., G. A. Catania, M. J. Hoffman, J. D. Gulley, M. P. Lüthi, C. Ryser, R. L. Hawley, and T. A. Neumann (2014), Direct observations of evolving subglacial drainage beneath the Greenland Ice Sheet, *Nature*, *514*(7520), 80–83, doi:10.1038/nature13796.

Balay, S., S. Abhyankar, M. Adams, J. Brown, P. Brune, K. Buschelman, L. Dalcin, V. Eijkhout, W. Gropp, D. Karpeyev, D. Kaushik, M. Knepley, L. Curfman McInnes, K. Rupp, B. Smith, S. Zampini, H. Zhang (2016), PETSc Users Manual , ANL-95/11 - Revision 3.7, `http://www.mcs.anl.gov/petsc/petsc-current/docs/manual.pdf`

Bamber, J. L., J. A. Griggs, R. T. W. L. Hurkmans, J. A. Dowdeswell, S. P. Gogineni, I. Howat, J. Mouginot, J. Paden, S. Palmer, E. Rignot, and D. Steinhage (2013), A new bed elevation dataset for Greenland, *Cryosphere*, *7*(2), 499–510, doi:10.5194/tc-7-499-2013.

Bartholomew, I., P. Nienow, D. Mair, A. Hubbard, M. A. King, and A. Sole (2010), Seasonal evolution of subglacial drainage and acceleration in a Greenland outlet glacier, *Nature Geosci.*, *3*(6), 408–411, doi:10.1038/ngeo863.

Bindschadler, R. (1983), The importance of pressurized subglacial water in separation and sliding at the glacier bed, *J. of Glaciol.*, *29*(101), 3–19, doi:10.1017/S0022143000005104.

Brown, J., J. Harper, and N. Humphrey (2017), Liquid water content in ice estimated through a full-depth ground radar profile and borehole measurements in western Greenland, *Cryosphere*, 11, 669–679, doi:10.5194/tc-11-669-2017.

Budd, W. F., P. L. Keage, and N. A. Blundy (1979), Emperical studies of ice sliding, *Journal of Glaciology*, *23*, 157-170, doi:10.1017/S0022143000029804.

Bueler, E., and W. Van Pelt (2015), Mass-conserving subglacial hydrology in the Parallel Ice Sheet Model version 0.6, *Geosci. Model Dev*, *8*, 1613–1635, doi:10.5194/gmd-8-1613-2015.

Clarke, G. (1996), Lumped-element analysis of subglacial hydraulic circuits *J. Geophys. Res.*, 101, 17547–17559, doi:10.1029/96JB01508.

Cuffey, K., W. Patterson (2010), The Physics of Glaciers, *Elsevier*, 4th edn., Burlington, MA, USA

Dalcin, L. D., R. R. Paz, P. A. Kler, and A. Cosimo (2011), Parallel distributed computing using Python, *Advances in Water Resources*, 34(9), 1124–1139 doi:10.1016/j.advwatres.2011.04.013.

Dow, C. F., A. Hubbard, A. D. Booth, S. H. Doyle, A. Gusmeroli, and B. Kulessa (2013), Seismic evidence of mechanically weak sediments underlying Russell Glacier, West Greenland, *Ann. Glaciol.*, *54*(64), 135–141, doi:10.3189/2013AoG64A032.

Dow, C. F., B. Kulessa, I. C. Rutt, S. H. Doyle, and A. Hubbard (2014), Upper bounds on subglacial channel development for interior regions of the Greenland ice sheet, *J. Glaciol*, doi:10.3189/2014JoG14J093.

Dow, C. F., B. Kulessa, I. C. Rutt, V. C. Tsai, S. Pimentel, S. H. Doyle, D. Van As, K. Lindbäck, R. Pettersson, G. A. Jones, and A. Hubbard (2015), Modeling of subglacial hydrological development following rapid supraglacial lake drainage, *J. Geophys. Res.: Earth Surface*, doi:10.1002/2014JF003333.

Ettema, J., M. R. Van Den Broeke, E. Van Meijgaard, W. J. Van De Berg, J. L. Bamber, J. E. Box, and R. C. Bales (2009), Higher surface mass balance of the Greenland ice sheet revealed by high-resolution climate modeling, *Geophys. Res. Lett.*, doi:10.1029/2009GL038110.

Flowers, G. E., G. K. C. Clarke (2002), A multicomponent coupled model of glacier hydrology 1. Theory and synthetic examples, *J. Geophys. Res.*, *107*(B11), 2287, doi:10.1029/2001JB001122.

Flowers, G. E.(2015), Modelling water flow under glaciers and ice sheets *Proc. R. Soc. London, Ser. A.*, 471(2176), doi:10.1098/rspa.2014.0907.

Fowler, A. C. (1987), Sliding with cavity formation, *J. Glaciol.*, *33*(115), 255-267, doi:10.1017/S0022143000008820.

Harrington, J. A., N. F. Humphrey, and J. T. Harper (2015), Temperature distribution and thermal anomalies along a flowline of the Greenland ice sheet, *Annals of Glac.*, 56(70), 98-104, doi:10.3189/2015AoG70A945.

Harper, J. T, N. F. Humphrey, T. W. Meierbachtol, J. A. Graly, and U. H. Fischer (2017), Borehole measurements indicate hard bed conditions, Kangerlussuaq sector, western Greenland Ice Sheet, *J. Geophys. Res.: Earth Surface*, 122, 1605-1618, doi:10.1002/2017JF004201.

Hewitt, I. J. (2011), Modelling distributed and channelized subglacial drainage: The spacing of channels, *J. Glaciol.*, *57*(202), 302–314, doi:10.3189/002214311796405951.

Hewitt, I. J., C. Schoof, and M. A. Werder (2012), Flotation and free surface flow in a model for subglacial drainage. Part 2. Channel flow, *J. Fluid Mech.*, *702*, 157–187, doi:10.1017/jfm.2012.166.

Hewitt, I. J. (2013), Seasonal changes in ice sheet motion due to melt water lubrication, *Earth Planet. Sci. Lett.*, *371-372*, 16–25, doi:10.1016/j.epsl.2013.04.022.

Hoffman, M. J., G. A. Catania, T. A. Neumann, L. C. Andrews, and J. A. Rumrill (2011), Links between acceleration, melting, and supraglacial lake drainage of the western Greenland Ice Sheet, *J. Geophys. Res.*, *116*, F04035, doi:10.1029/2010JF001934.

Hoffman, M., and S. Price (2014), Feedbacks between coupled subglacial hydrology and glacier dynamics, *J. Geophys. Res.: Earth Surface*, *119*(3), 414–436, doi:10.1002/2013JF002943.

Hoffman, M. J., L. C. Andrews, S. F. Price, G. A. Catania, T. A. Neumann, M. P. Lüthi, J. Gulley, C. Ryser, R. L. Hawley, and B. Morriss (2016), Greenland subglacial drainage evolution regulated by weakly connected regions of the bed, *Nature Comm.*, doi:10.1038/ncomms13903.

Humphrey, N. F. (1987), Coupling between water pressure and basal sliding in a linked-cavity hydraulic system *Proc. of the Vancouver Symposium*, August 1987, pp. 105-119, IAHS Publication number 170.

Iken, A. (1972), Measurements of Water Pressure in Moulins as Part of a Movement Study of the White Glacier, Axel Heiberg Island, Northwest Territories, Canada, *J. Glaciol.*, doi:10.1017/S0022143000022486.

Joughin, I., B. E. Smith, I. M. Howat, T. Scambos, and T. Moon (2010), Greenland flow variability from ice-sheet-wide velocity mapping, *J. Glaciol.*, 56, 415-430, doi:10.3189/002214310792447734.

Kamb, B. (1987), Glacier surge mechanism based on linked cavity configuration of the basal water conduit system *J. Geophys. Res.*, *92*(6), 9083-9100. doi:10.1029/JB092iB09p09083.

Meierbachtol, T., J. Harper, and N. Humphrey (2013), Basal drainage system response to increasing surface melt on the Greenland ice sheet, *Science*, *341*, 777–9, doi:10.1126/science.1235905.

Meierbachtol, T. W., J. T. Harper, J. V. Johnson, N. F. Humphrey, D. J. Brinkerhoff (2015), Thermal boundary conditions on western Greenland: Observational constraints and impacts on the modeled thermomechanical state, *J. Geophys. Res.: Earth Surface*, 120, 623-636, doi:10.1002/2014JF003375.

Murray, T., G. C. Clarke (1995), Black-box modeling of the subglacial water system, *J. Geophys. Res.*, 100, 10231-10245, doi:10.1029/95JB00671.

Palmer, S., A. Shepherd, P. Nienow, and I. Joughin (2011), Seasonal speedup of the Greenland Ice Sheet linked to routing of surface water, *Earth Planet. Sci. Lett.*, 302, 423-428, doi:10.1016/j.epsl.2010.12.037.

Rignot, E., P. Kanagaratnam (2006), Changes in the velocity structure of the Greenland ice sheet *Science*, 311, 986-990, doi:10.1126/science.1121381.

Ryser, C., M. P. Lüthi, L. C. Andrews, G. A. Catania, M. Funk, R. Hawley, M. Hoffman, and T. A. Neumann (2014), Caterpillar-like ice motion in the ablation zone of the Greenland ice sheet, *J. Geophys. Res.: Earth Surface*, 119, 2258-2271, doi:10.1002/2013JF003067.

Schoof, C. (2005), The effect of cavitation on glacier sliding, *Proc. R. Soc. Lond. As*, 461, 609–627, doi:10.1098/rspa.2004.1350.

Schoof, C. (2010), Ice-sheet acceleration driven by melt supply variability., *Nature*, *468*(7325), 803–806, doi:10.1038/nature09618.

Schoof, C., I. J. Hewitt, and M. A. Werder (2012), Flotation and free surface flow in a model for subglacial drainage. Part 1. Distributed drainage, *Journal of Fluid Mechanics*, *702*, 126–156, doi:10.1017/jfm.2012.165.

SeaRISE website (2012), available at: `http://websrv.cs.umt.edu/isis/index.php/SeaRISE_Assessment`

Shepherd, A., A. Hubbard, P. Nienow, M. King, M. McMillan, and I. Joughin (2009), Greenland ice sheet motion coupled with daily melting in late summer, *Geophys. Res. Lett.*, 36, L01501, doi:10.1029/2008GL035758.

Sole, A., P. Nienow, I. Bartholomew, D. Mair, T. Cowton, A. Tedstone, and M. A. King (2013), Winter motion mediates dynamic response of the Greenland Ice Sheet to warmer summers, *Geophys. Res. Lett.*, *40*(15), 3940–3944, doi:10.1002/grl.50764.

Sundal, A. V., A. Shepherd, P. Nienow, E. Hanna, S. Palmer, and P. Huybrechts (2011), Melt-induced speed-up of Greenland ice sheet offset by efficient subglacial drainage., *Nature*, *469*(7331), 521–524, doi:10.1038/nature09740.

van de Wal, R. S. W., W. Boot, M. van den Broeke, C. Smeets, C. Reijmer, J. Donker, J. Oerlemans (2008), Large and rapid melt-induced velocity changes in the ablation zone of the Greenland Ice Sheet *Science*, 321, 111-113, doi:10.1126/science.1158540.

van de Wal, R. S., C. J. Smeets, W. Boot, M. Stoffelen, R. Van Kampen, S. H. Doyle, F. Wilhelms, M. R. Van Den Broeke, C. H. Reijmer, J. Oerlemans, and A. Hub-

bard (2015), Self-regulation of ice flow varies across the ablation area in south-west Greenland, 9, 603-611, *Cryosphere*, doi:10.5194/tc-9-603-2015.

Walder, J. S. (1986), Hydraulics of subglacial cavities, *J. Glaciol.*, *32*(112), 439-445, doi:10.1017/S0022143000012156.

Werder, M. A., I. J. Hewitt, C. G. Schoof, and G. E. Flowers (2013), Modeling channelized and distributed subglacial drainage in two dimensions, *J. of Geophys. Res.: Earth Surface*, *118*(4), 2140–2158, doi:10.1002/jgrf.20146.

Wright, P. J., J. T. Harper, N. F. Humphrey, and T. W. Meierbachtol (2016), Measured basal water pressure variability of the western Greenland Ice Sheet: Implications for hydraulic potential, *J. of Geophys. Res.: Earth Surface*, 121, 1134–1147, doi:10.1002/2016JF003819.

Zwally, H. J., W. Abdalati, T. Herring, K. Larson, J. Saba, and K. Steffen (2002), Surface melt-induced acceleration of greenland ice-sheet flow, *Science*, *297*(5579), 218–222, doi:10.1126.1072708.

Chapter 3

Ice sheet retreat history reveals elevated HTM precipitation

Overview

This chapter has been accepted for Publication in The Cryosphere.

Authors

Jacob Downs, Jesse Johnson, Jason Briner, Nicolás Young, Alia Lesnek, Josh Cuzzone

Abstract

We investigate changing precipitation patterns in the Kangerlussuaq region of west central Greenland during the Holocene thermal maximum, using a new chronology of ice sheet terminus position through the Holocene and a novel inverse modeling approach based on the unscented transform (UT). The UT is applied to estimate changes in annual precipitation in order to reduce the misfit between modeled and observed terminus

positions. We demonstrate the effectiveness of the UT for time-dependent data assimilation, highlighting its low computational cost and trivial parallel implementation. Our results indicate that Holocene warming coincided with elevated precipitation, without which modeled retreat in the Kangerlussuaq region is more rapid than suggested by observations. Less conclusive is if high temperatures during the HTM were specifically associated with a transient increase in precipitation, as the results depend on the assumed temperature history. Our results highlight the important role that changing precipitation patterns had in controlling ice sheet extent during the Holocene.

3.1 Introduction

During the early Holocene (∼11.7 - 8 ka BP), terrestrial and marine climate proxies from the northern hemisphere reveal a warmer than present peak in temperature (Kaufman et al., 2004; Marcott et al., 2013). This period of elevated temperatures, likely initiated by greater than modern insolation, is referred to as the Holocene thermal maximum (HTM). Its onset, duration, and severity were likely spatially variable (Kaufman et al., 2004). Records of HTM warming can be found in Greenland ice core records. For example, temperatures measured in the Dye-3 borehole show a pronounced HTM signal occurring from 7 to 4 ka BP and having value of 2.5° above present temperatures (Dahl-Jensen et al., 1998; Miller et al., 2010), whereas at the GISP2 site, the HTM appears to occur slightly earlier, following the 8.2 ka BP cold event (Kobashi et al., 2017) (Figure 3.1).

While warming during the HTM is well established, less is known about the regional changes in precipitation that accompanied increased temperatures. Ice core records provide long term estimates of accumulation (Alley et al., 1993), but these point measurements near ice divides are not representative of the precipitation across the ice sheet, particularly at lower elevations near the coast. Because the HTM was accompanied by

lower Arctic sea ice extent (Polyak et al., 2010), it is possible that additional moisture was available to the GrIS from open Arctic waters. This is supported by proxy evidence showing an increase in winter precipitation in western Greenland coincident with HTM warming (Thomas et al., 2016). However, temperature is known with greater certainty than precipitation.

Understanding feedbacks between temperature and precipitation during the HTM has implications for the future of the GrIS. Warming and declining sea ice are projected to cause an increase in Arctic precipitation (Bintanja and Selten, 2014; Singarayer et al., 2006). On a global scale, the moisture content of the atmosphere increases by around 7% for every degree of warming, according to the Clausius-Clapeyron relation. On a regional scale, declining arctic sea ice is expected to cause changes in atmospheric circulation, bringing more moisture to the Arctic (Bintanja and Selten, 2014). While there are important differences between HTM and modern climate, the history of retreat in West Greenland may provide insights into how the GrIS will respond to a warmer and possibly wetter future climate.

Modeling studies indicate that Holocene retreat in land terminating regions of the GrIS were controlled primarily by surface mass balance rather than ice dynamics (Cuzzone et al., 2019; Lecavalier et al., 2014). Given the primary importance of surface mass balance in controlling modeled retreat, we explore the hypothesis that enhanced winter snowfall during the HTM may have slowed retreat by partially offsetting increased surface melt (Thomas et al., 2016). We investigate changes in precipitation in a land terminating sector of the western central GrIS, near Kangerlussuaq, taking advantage of a new chronology of ice sheet terminus position (Young et al., view) and a novel inverse modeling approach based on the unscented transform (UT) (Julier and Uhlmann, 1997). In particular, we use the UT to estimate changes in annual precipitation during the Holocene by reducing the misfit between modeled and observed terminus positions in an isothermal flowline ice dynamics model (Brinkerhoff et al., 2017) (section 3.2.1).

The inverse problem is posed as a Bayesian inference problem, and its solution involves estimating a non-Gaussian posterior probability distribution. Markov Chain Monte Carlo (MCMC) methods, such as Metropolis Hastings method (Chib and Greenberg, 1995), provide one means of solving the inference problem by generating random samples from the posterior distribution. Generating samples from the posterior, however, requires repeatedly running the ice dynamics model with different precipitation histories as input, which is intractable even for a relatively computationally inexpensive flowline model.

The unscented transform provides a computationally efficient and trivially parallelizable alternative to MCMC methods. The basic idea of the unscented transform is to use a small, fixed number of deterministic sample points in order to estimate the statistical moments (e.g. mean and covariance) of the posterior distribution. Sigma points, each of which represents a different precipitation history input to the ice dynamics model, are generated a priori (section 3.2.5). Consequently, all model runs can be performed simultaneously in parallel resulting in at least a 100 fold speed up compared to MCMC methods.

3.2 Numerical methods for inference

3.2.1 Ice-sheet model

We use the 1D, isothermal, flowline model with higher-order momentum balance described in Brinkerhoff et al. (2017). The momentum conservation equations are simplified using the Blatter-Pattyn approximation, assuming hydrostatic pressure and negligible vertical resistive stresses (Blatter, 1995; Pattyn, 2003). Default parameter values used in this work are specified in Table 3.1.

We adopt a linear sliding law of the form

$$\tau_b = \beta^2 N u_b \tag{3.1}$$

where τ_b is basal shear stress, β^2 is a constant basal traction parameter, N is effective pressure, and u_b is sliding speed. Based on borehole water pressure measurements in Wright et al. (2016), basal water pressure P_w is assumed to be a fixed fraction $P_{frac} = 0.85$ of ice overburden pressure P_0. Effective pressure is therefore given by

$$N = P_0 - P_{frac} P_0. \tag{3.2}$$

The basal traction parameter β^2 is tuned to minimize the misfit between modeled and observed surface velocities from Mouginot et al. (2017) for modern Isunnguata Sermia.

3.2.2 Flowline Selection and Moraine Age Constraints

To define the path followed by ice, we assume that flow follows the modern surface velocity field inland of the present day margin. In ice free regions, the direction of ice flow is inferred from bedrock topography (Figure 3.1). Since the direction of ice flow is unknown and time varying, we cannot directly quantify the uncertainty introduced by errors in flowline selection. To account for some of this uncertainty, we perform inversions on two plausible, adjacent paleo-flowlines in the Kangerlussuaq area.

The rate of Holocene retreat on each flowline is estimated using constraints on ice sheet terminus position from (Young et al., view) (Figure 3.1). Terminus position data in Young et al. (view) indicates that in the early Holocene (11.6 ka BP), the ice sheet margin was some tens of kilometers inland of the present day coastline. Although the moraine patterns are spatially complex, generally speaking there was a period of moderate retreat ($\sim$10 km on the northern flowline and $\sim$30 km on the southern flowline) from 11.6 to

10.3 ka BP, followed by rapid retreat (∼100 km on both flowlines) from 10.3 to 8.1 ka BP. By 8.1 ka BP, the margin position was within 20 km of its present position on both flowlines (Figure 3.5). The modern terminus position provides one additional constraint. Moraine ages have uncertainties of up to ± 400 years.

For modern bedrock geometry along the flowlines, we use BedMachine v3 (Morlighem et al., 2017). Isostatic uplift and relative sea level changes are accounted for using a Glacial isostatic adjustment model (Caron et al., 2018). This model, combined with the retreat chronology in Young et al. (view), indicate that ice remained grounded on both the northern and southern flowlines from 11.6 ka BP onward.

3.2.3 Positive degree day model

Surface mass balance is estimated using a positive degree day (PDD) model (Johannesson et al., 1995). Annual surface mass balance is constructed in the PDD model using estimates of average monthly precipitation and temperature. Inputs into the PDD model include the unknown ice surface elevation S, modern monthly temperature T_m and precipitation P_m along the flowlines, as well as the seasonal temperature anomaly ΔT. As in Cuzzone et al. (2019) , modern temperature and precipitation are computed as 30 year averages from 1980-2010 using Box (2013).

To assess the sensitivity of modeled retreat history to temperature, we perform experiments using temperature reconstructions from both Buizert et al. (2018) and Dahl-Jensen et al. (1998). For the spatially explicit Buizert et al. (2018) reconstruction, monthly temperature anomalies are computed as averages along the flowlines. In contrast, Dahl-Jensen et al. (1998) reconstruct temperature only at the GRIP and Dye-3 borehole locations (Figure 3.1). Since a full Holocene reconstruction is unavailable at the Dye-3 borehole site, which is closer to Kangerlussuaq, we use the temperature reconstruction at GRIP. The HTM is roughly 0.3° C warmer and 1,500 years later in Dahl-Jensen et al. (1998) than Buizert et al. (2018) (Figure 3.6)

A limitation of the Dahl-Jensen et al. (1998) reconstruction is that it does not resolve seasonal temperatures. To address this, we calculate the difference between monthly and mean annual temperatures in Buizert et al. (2018) and apply those offsets to the mean annual temperature at GRIP from Dahl-Jensen et al. (1998).

Surface temperature T is computed monthly as

$$T = T_m + \Delta T + \alpha(S - S_m) \tag{3.3}$$

where S_m is the modern surface elevation, and $\alpha = 5^\circ$ C km^{-1} is the lapse rate (Abe-Ouchi et al., 2007). Following Ritz et al. (2001) and Cuzzone et al. (2019), precipitation P along the flowline is estimated based on the Clausius-Clapeyron relation. In particular precipitation is estimated by

$$P = P_T + \Delta P = P_m \exp\left(\lambda_p (T - T_m)\right) + \Delta P. \tag{3.4}$$

The term P_T accounts for changes in precipitation solely due to changes in temperature. Here $\lambda_p = 0.07$, which results in a 7% increase in precipitation for every 1° C increase in temperature above modern (Abe-Ouchi et al., 2007; Ritz et al., 2001).

The term P_T does not capture the effects of many unknown climate factors that may have caused dynamic, regional changes in Holocene precipitation. Therefore, we introduce a precipitation anomaly term ΔP, analogous to the temperature anomaly ΔT. This time-dependent function, which has units of meters water equivalent (m.w.e.) a^{-1}, is used to adjust precipitation uniformly across a flowline in order to reduce mismatch between modeled and observed terminus positions. Unlike ΔT, which can be inferred from ice cores, ΔP will be used as a control variable to be determined using the inverse methods detailed in section 3.2.5. Equations 3.3 and 3.4 provide a method of accounting for elevation changes through time and downscaling inputs to match the mesh resolution of the model ($\sim$ 1 km).

Positive degree days and snowfall are computed month-by-month based on mean monthly temperature and precipitation (Johannesson et al., 1995). Snow is melted first at a rate of 5×10^{-3} m.w.e. per degree day followed by ice at a rate of 8×10^{-3} m.w.e. per degree day. Snow melt is initially supposed to refreeze in the snowpack as superimposed ice. Runoff begins when the superimposed ice reaches a given fraction (60%) of the snow cover (Reeh, 1991). A listing of ice-flow and PDD model parameters is provided in Table 3.1, and all data sets used in the model are shown in Table 3.2.

3.2.4 Modeling Limitations

A limitation of our modeling approach is that we do not account for potential ice dynamical effects caused by changes in surface runoff or subglacial hydrology. Modeling melt water runoff would be difficult in a flowline model due to flux of melt water in and out of the path of ice flow. Another limitation is that our model is isothermal. Unless ice temperature is treated in a vertically averaged sense, resolving temperature would require a 2D mesh, which would considerably increase the computational cost of the model. We consider the consequences of this simplification in section 3.3.3, where we test sensitivity to the ice hardness parameter.

The PDD scheme outlined in section 3.2.3 does not account for changes in surface mass balance due to orographic forcing, or other complex interactions between the ice sheet and climate system that could be captured by coupling the ice sheet model to an Earth system model (Bahadory and Tarasov, 2018). Since our emphasis is on estimating precipitation and surface mass balance using an inverse modeling approach, we believe the computational cost of such an approach outweighs the benefits. Uncertainties related to feedbacks between ice dynamics and climate are assessed via extensive sensitivity testing (section 3.3.3).

Table 3.1: Summary of primary model parameters used in this work. Default values are provided where applicable.

Description	Symbol	Value	Units
PDD Model Parameters			
Std. deviation	σ	5.5	C
Std. deviation, accumulation	σ_a	5 C	
Ablation rate, snow	λ_s	$5{\times}10^{-3}$	m.w.e. C^{-1} d^{-1}
Ablation rate, ice	λ_i	$8{\times}10^{-3}$	m.w.e. C^{-1} d^{-1}
Precipitation param.	λ_p	7×10^{-2}	C^{-1}
Superimposed ice fraction	p_{max}	0.6	-
Ice Flow Parameters			
Rate factor	A	3.5×10^{-25}	s^{-1} Pa^{-3}
Basal traction	β^2	$1.2{\times}10^{-3}$	Pa a m^{-1}
Water pressure fraction	P_{frac}	0.85	-
Precipitation Prior			
Prior kernel variance	σ_p^2	$5{\times}10^{-4}$	-
Prior time Scale	τ	8×10^{3}	-
Measurement Prior			
Prior kernel variance	σ_ℓ^2	1×10^{6}	-

Table 3.2: Citations for the primary data sets used in this work.

Data	Citation
Terminus position chronology	Young et al. (view)
Bedrock elevation	Morlighem et al. (2017)
Modern ice surface velocity	Mouginot et al. (2017)
Modern precipitation	Box (2013)
Temperature reconstructions	Buizert et al. (2018)
	Dahl-Jensen et al. (1998)
Glacial Isostatic Adjustment	Caron et al. (2018)

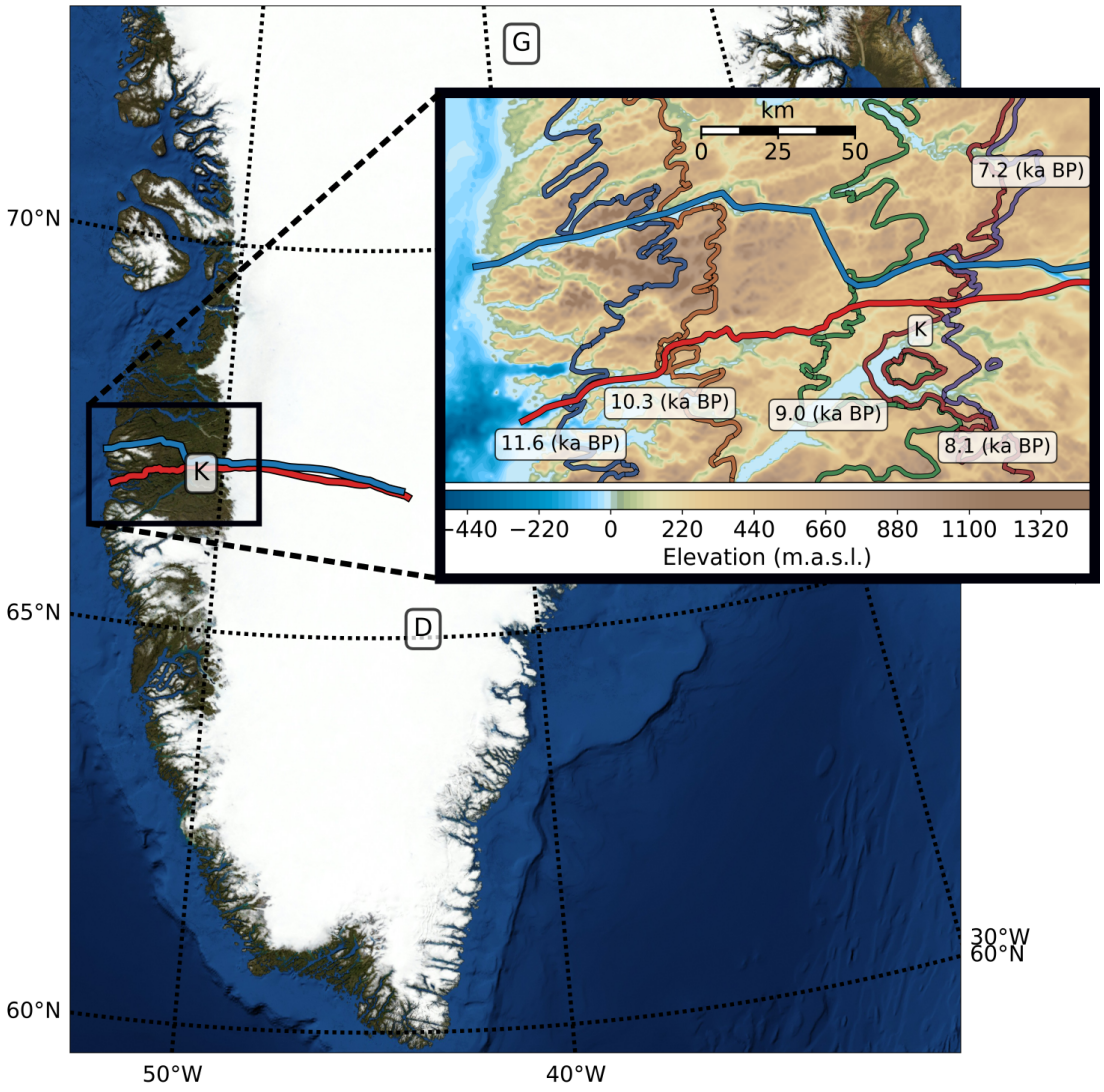

Figure 3.1: . K marks the position Kangerlussuaq , while D and G mark the locations of the Dye-3 and GISP2 boreholes respectively. Northern and southern paleo-flowlines are shown as blue and red lines running left to right. The inset shows a detailed view of the modeled region. Modern bedrock elevation is expressed in meters above sea level. Historical moraines dating from 11.6 to 7.2 ka BP are indicated by labeled lines.

3.2.5 Data Assimilation Approach

In order to assess the initial mismatch between modeled and observed retreat histories, we perform a reference experiment with $\Delta P = 0$ and ΔT estimates from both Buizert

et al. (2018) and Dahl-Jensen et al. (1998). To improve the fit to observations, we assimilate terminus position data to obtain improved estimates of Holocene precipitation anomalies. Previous modeling studies indicate that Holocene retreat in land-terminating sectors of the GrIS were dominated by surface mass balance rather than ice dynamics (Cuzzone et al., 2019; Lecavalier et al., 2014). Uncertainty in Holocene climate, and consequently surface mass balance, is therefore likely the primary cause of discrepancies between modeled and observed terminus positions.

In principle ΔP, ΔT, or both could be tuned to improve the fit between modeled and observed terminus positions. We focus on precipitation because it is more poorly constrained than temperature. In the upcoming sections, we introduce a framework for time-dependent data assimilation based on the unscented transform (UT). Sections 3.2.5 - 3.2.5 outline the basic tenets of the UT. Sections 3.2.5 - 3.2.5 outline how the UT can be applied to estimate precipitation anomalies.

Overview of the Unscented transform

In what follows, the notation $\boldsymbol{x} \sim \mathcal{N}(\boldsymbol{x_0}, P_x)$ means that $\boldsymbol{x}$ is a normally distributed random variable with mean vector $\boldsymbol{x_0}$ and covariance matrix P_x. Suppose that $\boldsymbol{x} \sim \mathcal{N}(\boldsymbol{x_0}, P_x)$, and $\mathcal{F} : \mathbb{R}^n \to \mathbb{R}^m$ is a nonlinear function. We would like to estimate the distribution of the non-Gaussian random variable

$$\boldsymbol{y} = \mathcal{F}(\boldsymbol{x}) + \boldsymbol{\epsilon}. \tag{3.5}$$

where $\boldsymbol{\epsilon} \sim \mathcal{N}(\boldsymbol{0}, R)$ is the measurement noise.

In general, the non-Gaussian probability distribution for $\boldsymbol{y}$ can be approximated using Markov chain Monte Carlo (MCMC) methods such as the Metropolis-Hastings algorithm (Chib and Greenberg, 1995). However, if the nonlinear function is time-consuming to compute, generating thousands of MCMC samples is often intractable. As a computa-

tionally efficient alternative to MCMC methods, Julier and Uhlmann (1997) introduced a method for approximating the mean and covariance of $\boldsymbol{y}$ called the unscented transform (UT) [1].

The term unscented transform has been applied somewhat broadly to a family of methods that approximate the statistical moments of a non-Gaussian random variable using a small, deterministic set of sample points called sigma points. It is known primarily in the context of the unscented Kalman filter. However, the UT can be applied more generally as an alternative to traditional MCMC methods. Sigma points and weight sets are designed to accurately estimate moments of a transformed random variable using a minimal number of function evaluations.

A set of vectors, called sigma points, are chosen with the same weighted sample mean and weighted covariance structure as $\boldsymbol{x}$. There are many algorithms for generating sigma points sets with different numbers of points and orders of accuracy. A commonly used set of $2n + 1$ sigma points is given by

$$\boldsymbol{\chi_i} = \begin{cases} \boldsymbol{x_0} & i = 0 \\ \boldsymbol{x_0} - \sqrt{n+\kappa}[\sqrt{P_x}]_i & i = 1, \cdots, n \\ \boldsymbol{x_0} + \sqrt{n+\kappa}[\sqrt{P_x}]_i & i = n+1, \cdots, 2n \end{cases} \tag{3.6}$$

with corresponding mean / covariance weights given by

$$w_i^{(m)} = w_i^{(c)} = \begin{cases} \kappa/(n+\kappa) & i = 0 \\ 1/2(n+\kappa) & \text{otherwise} \end{cases}. \tag{3.7}$$

The notation $\left[\sqrt{P_x}\right]_i$ refers to the i-th row of a matrix square root (typically computed by Cholesky factorization) of P_x, and κ is a free parameter controlling the scaling of

[1] According to Jeffrey Uhlmann, the creator of the UT, the term "unscented" was inspired by a stick of deodorant and has no technical significance.

the sigma points around the mean. Julier and Uhlmann (1997) recommend a default value of $\kappa = 3 - n$. However, κ can be fine tuned to reduce prediction errors for a given problem.

The nonlinear function $\mathcal{F}$ is applied to each sigma point to yield a set of transformed points

$$\boldsymbol{\mathcal{Y}_i} = \mathcal{F}(\boldsymbol{\chi_i}). \tag{3.8}$$

The mean $\bar{\boldsymbol{y}}$ and covariance matrix P_y of $\boldsymbol{y}$ are then estimated as weighted sums

$$\bar{\boldsymbol{y}} = \sum_{i=0}^{2n} w_i^{(m)} \boldsymbol{\mathcal{Y}_i} \tag{3.9}$$

$$P_y = \sum_{i=0}^{2n} w_i^{(c)} (\boldsymbol{\mathcal{Y}_i} - \bar{\boldsymbol{y}})(\boldsymbol{\mathcal{Y}_i} - \bar{\boldsymbol{y}})^T + R. \tag{3.10}$$

A visual example of this algorithm is shown in Figure 3.2.

Bayesian Inference using the UT

Given a measurement $\boldsymbol{y_o}$, we would like to estimate the posterior distribution

$$P(\boldsymbol{x}|\boldsymbol{y_o}) \propto P(\boldsymbol{y}|\boldsymbol{x})P(\boldsymbol{x}). \tag{3.11}$$

Using an approach called statistical linearization (Sarkka, 2013) the joint distribution for $[\boldsymbol{x},\ \boldsymbol{y}]^T$ can be approximated by

$$\begin{bmatrix} \boldsymbol{x} \\ \boldsymbol{y} \end{bmatrix} \sim \mathcal{N}\left(\begin{bmatrix} \boldsymbol{x} \\ \boldsymbol{\mu} \end{bmatrix}, \begin{bmatrix} P_x & P_{xy} \\ P_{xy}^T & P_y \end{bmatrix} \right) \tag{3.12}$$

with

$$\boldsymbol{\mu} = \sum_i w_i^{(m)} \boldsymbol{\mathcal{Y}_i} \tag{3.13}$$

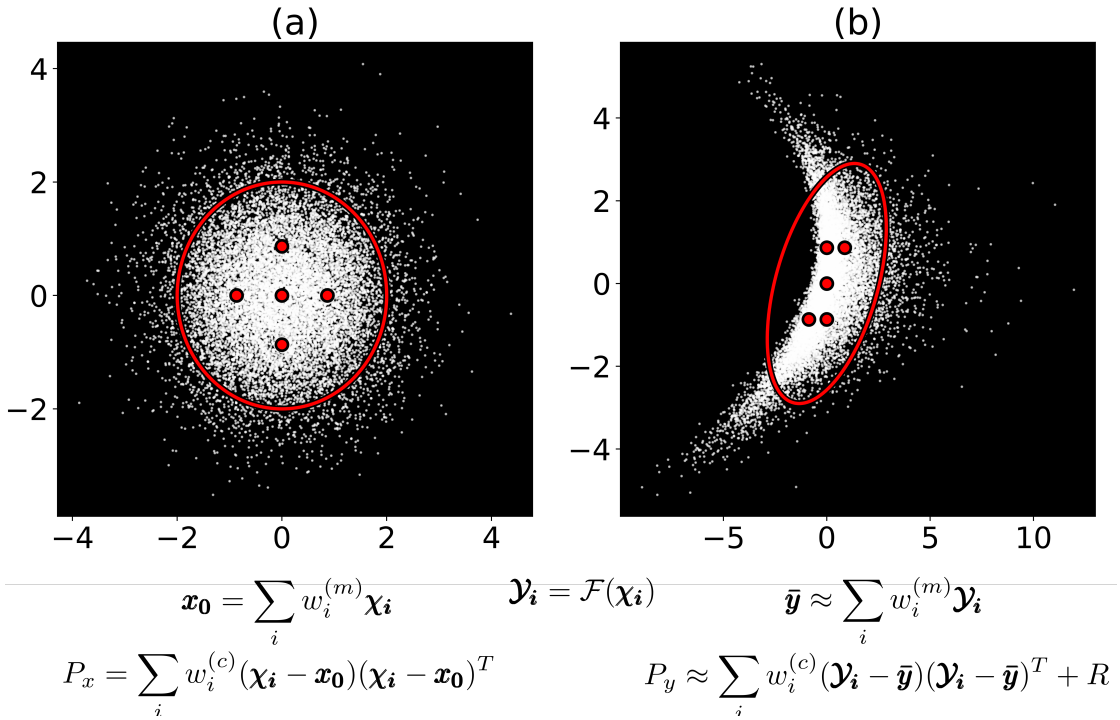

Figure 3.2: (a) White points are samples from a 2D Gaussian distribution $\boldsymbol{x} \sim \mathcal{N}(\boldsymbol{0}, I)$. The red ellipse represents the covariance of the distribution, while red points are sigma points $\boldsymbol{\chi_i}$ used for the unscented transform (UT). (b) White points are samples from the transformed, non-Gaussian distribution for $\boldsymbol{y} = \mathcal{F}(\boldsymbol{x}) + \boldsymbol{\epsilon}$ with $\boldsymbol{\epsilon} \sim \mathcal{N}(\boldsymbol{0}, R)$. Red points are transformed sigma points $\boldsymbol{\mathcal{Y}_i} = \mathcal{F}(\boldsymbol{\chi_i})$. UT approximations of the mean $\bar{\boldsymbol{y}}$ and covariance P_y of $\boldsymbol{y}$ are estimated via weighted sums of transformed sigma points.

$$P_y = \sum_i w_i^{(c)} (\boldsymbol{\mathcal{Y}_i} - \boldsymbol{\mu})(\boldsymbol{\mathcal{Y}_i} - \boldsymbol{\mu})^T + R \tag{3.14}$$

$$P_{xy} = \sum_i w_i^{(c)} (\boldsymbol{\mathcal{X}_i} - \boldsymbol{x_0})(\boldsymbol{\mathcal{Y}_i} - \boldsymbol{\mu})^T. \tag{3.15}$$

Here, $\boldsymbol{\mathcal{X}_i}$ and $\boldsymbol{\mathcal{Y}_i} = \mathcal{F}(\boldsymbol{\mathcal{X}_i})$ are sigma points and transformed sigma points respectively. Matrices P_y and P_{xy} are known as the measurement covariance and cross covariance respectively.

Given a measurement $\boldsymbol{y_0}$, the joint distribution then easily yields a Gaussian approximation of the posterior distribution. Letting

$$K = P_{xy} P_y^{-1} \tag{3.16}$$

we have

$$\boldsymbol{x'} = \boldsymbol{x_o} + K\left[\boldsymbol{y_o} - \boldsymbol{\mu}\right] \tag{3.17}$$

$$P' = P_x - KP_yK^T \tag{3.18}$$

where $\boldsymbol{x'}$ and P' are approximations of the posterior mean and covariance respectively. Readers familiar with Kalman filters might recognize that $\boldsymbol{x'}$ and P' are computed using a Kalman "update" step given a measurement $\boldsymbol{y_o}$ and Kalman gain K (Sarkka, 2013).

Assimilating Glacier Length Observations

Time-dependent data assimilation using the UT involves running the ice sheet model with a set of different precipitation anomaly histories, each corresponding to a different sigma point. This is followed by a post-processing step, which incorporates the ice sheet terminus chronology data via a correction of the prior mean vector and covariance matrix. Implementation of the unscented transform is straightforward and easily parallelizable since each model run is independent. In the following section, we outline the mathematical details of this process.

We seek to find ΔP histories that match the observed retreat history on both flowlines. An optimal solution should reproduce the observed retreat history within uncertainty, while not overfitting the data. We discretize the problem by estimating the precipitation anomaly at times $t_1, t_2, \cdots, t_n$ ranging from 11.6 - 0 ka BP. In practice, we use a regular grid of 44 points, spaced roughly 250 years apart. Precipitation anomaly values at these time points are denoted by $\Delta p_1, \Delta p_2, \cdots, \Delta p_n$ respectively and assembled in a vector

$$\boldsymbol{\Delta p} = [\Delta p_1, \Delta p_2, \cdots, \Delta p_n]^T. \tag{3.19}$$

Given a multivariate Gaussian prior $\boldsymbol{\Delta p} \sim \mathcal{N}(\boldsymbol{\Delta p_0}, P_0)$, which encodes assumptions about the structure of the precipitation anomaly (section 3.2.5), we would like to estimate

the mean and covariance of the posterior distribution

$$P(\boldsymbol{\Delta p}|\boldsymbol{\ell_0}) \propto P(\boldsymbol{\ell_0}|\boldsymbol{\Delta p})P(\boldsymbol{\Delta p}). \tag{3.20}$$

Here, the measurement vector

$$\boldsymbol{\ell_0} = [\ell_1, \ell_2, \cdots, \ell_m]^T \tag{3.21}$$

contains measured glacier lengths at discrete points in time. Our procedure for defining the measurement mean $\boldsymbol{y_o}$ and covariance R are discussed in section 3.2.5.

We can think of the ice sheet model as a function that maps precipitation anomaly inputs to glacier length outputs with some additive observation noise

$$\boldsymbol{\ell} = \mathcal{F}(\boldsymbol{\Delta p}) + \boldsymbol{\epsilon}. \tag{3.22}$$

Discrete precipitation anomaly values are linearly interpolated for input into the ice-dynamics model, which has time steps on the order of months. The function $\mathcal{F}$ returns glacier lengths at the same m discrete times as in $\boldsymbol{\ell_0}$.

To predict the posterior distribution, we use the methods outlined in sections 3.2.5 and 3.2.5. First, sigma points are generated based on the prior distribution for $\boldsymbol{\Delta p}$. To reduce computational costs, we use a minimal set of $n + 1 = 45$ sigma points $\boldsymbol{\mathcal{P}_i}$ with corresponding weights $w_i^{(m)} = w_i^{(c)}$ generated using the method presented in Menegaz et al. (2011). Their method includes one free parameter $0 < w_0 < 1$, which can be tuned to reduce prediction errors. While this method has a lower order of accuracy than other methods, we find it often produces comparable results to other larger sigma point sets in practice.

Sigma points are propagated through the model to obtain transformed points $\boldsymbol{\mathcal{L}_i} = \mathcal{F}(\boldsymbol{\mathcal{P}_i})$. In this context, sigma points $\boldsymbol{\mathcal{P}_i}$ correspond to different time-dependent precip-

itation anomaly histories, while the transformed points $\boldsymbol{\mathcal{L}_i}$ correspond to the resulting glacier length histories given those precipitation anomalies as input (Figure 3.3). The structure of the sigma points reflects the mathematical formulation of the Menegaz et al. (2011) sigma points. Hence they are not merely random samples from the prior distribution.

Transformed sigma points are computed simultaneously in parallel, using one core per sigma point. After all transformed sigma points have been computed, the mean and covariance of the posterior distribution are estimated as outlined in Section 3.2.5. In parallel, this procedure takes roughly the same amount of time as a single forward model run. Unlike a standard filtering approach to data assimilation, all measurement data is incorporated simultaneously rather than time step by time step. For that reason, the Kalman update step corrects the entire time-dependent precipitation history at once. Moreover, unlike in Kalman smoothing, we approximate the full posterior distribution rather rather than the probability distributions

$$\begin{matrix} P(\Delta p_i|\boldsymbol{\ell_0}) \\ i = 1, \cdots, n \end{matrix}. \tag{3.23}$$

Note that the variables Δp_k with $k \neq i$ are marginalized out of the Kalman smoothing distributions. The use of time-dependent sigma points distinguishes our approach from standard Kalman filtering or Kalman smoothing approaches, and does not rely on the assumptions that states (Δp_i's) and measurements (ℓ_i's) satisfy the Markov property.

Gaussian Process Prior for Regularization

We adopt a Gaussian process prior (Rasmussen, 2004) to control the temporal smoothness of ΔP. A Gaussian process can be thought of as a distribution over functions. That is, random samples from a Gaussian process are functions rather than individual

points or vectors. A collection of random variables $\{f(t) : t \in \mathcal{T}\}$ is said to be drawn from a Gaussian process with mean function $m(\cdot)$ and covariance function $k(\cdot, \cdot)$ if for any finite set of elements $t_1, \cdots, t_n \in \mathcal{T}$, the random variables $f(t_1), \cdots, f(t_n)$ have the distribution

$$\boldsymbol{f} \sim \mathcal{N}(\boldsymbol{m}, K) \tag{3.24}$$

with

$$\boldsymbol{f} = [f(t_1), f(t_2), \cdots, f(t_n)]^T, \tag{3.25}$$

$$\boldsymbol{m} = [m(t_1), m(t_2), \cdots, m(t_n)]^T, \tag{3.26}$$

and

$$K = \begin{bmatrix} k(t_1, t_1) & \cdots & k(t_1, t_n) \\ \vdots & \ddots & \vdots \\ k(t_n, t_1) & \cdots & k(t_n, t_n) \end{bmatrix}. \tag{3.27}$$

The set $\mathcal{T}$ is called the index set, and specifies the domain of the Gaussian process. Here, the index set represents points in time.

The prior distribution for $\boldsymbol{\Delta p}$ has mean vector $\boldsymbol{\Delta p_0}$ and covariance matrix $P_0 = K$ of the form shown in Equation 3.27. We use a squared exponential covariance function

$$k(t,\ t') = \sigma_p^2 \exp\left(\frac{(t - t')^2}{2\tau^2}\right) \tag{3.28}$$

where σ^2 is a scaling constant, and τ is a characteristic time scale. Variables Δp_i and Δp_k are more highly correlated the closer they are in time. In effect, this acts as a form of temporal regularization, in which smooth precipitation history functions are preferred over less smooth ones. We discuss the choice of the mean $\boldsymbol{\Delta p_0}$ in section 3.3.2.

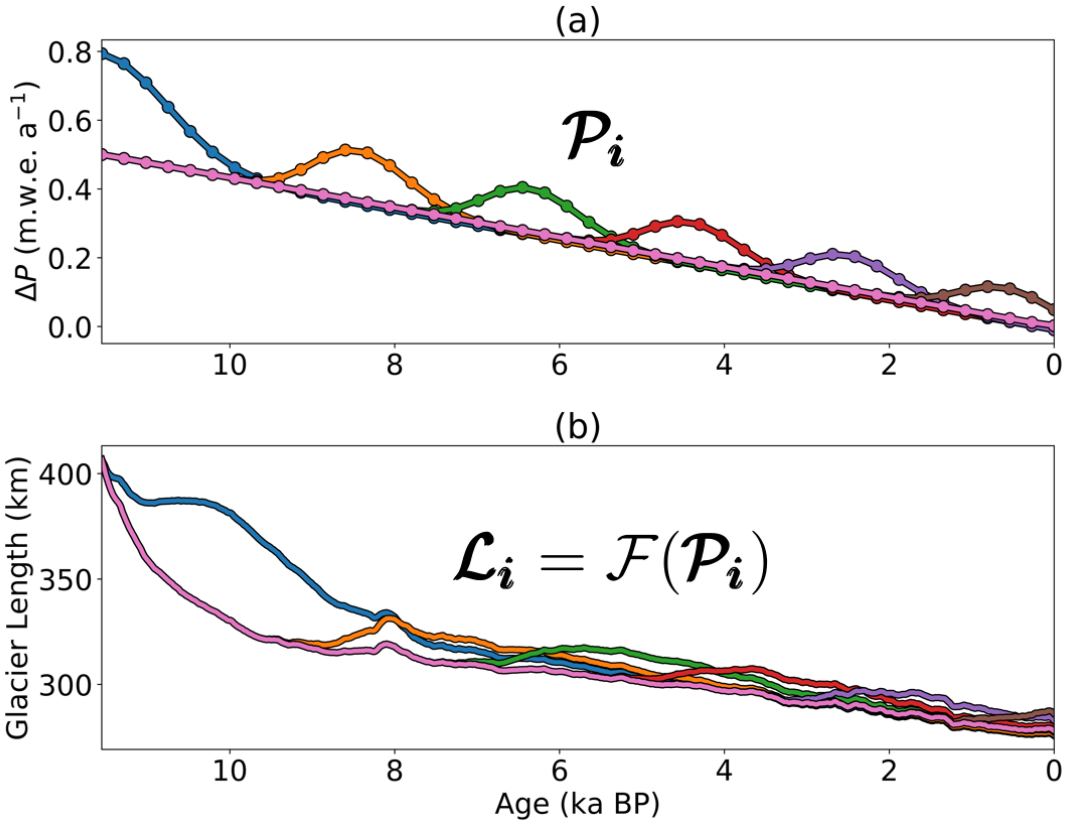

Figure 3.3: (a) A subset of 6 out of a total of 45 Menegaz et al. (2011) sigma points $\boldsymbol{\mathcal{P}_i}$ representing different precipitation anomaly histories. (b) Six corresponding glacier length histories $\boldsymbol{\mathcal{L}_i}$, or transformed sigma points, obtained by inputting the sigma points $\boldsymbol{\mathcal{P}_i}$ into the ice dynamics model $\mathcal{F}$.

Measurement Mean and Variance

Observations of terminus position are available roughly every 1000 years between 11.6 and 7.2 ka BP, with a gap from 7.2 ka BP to present. In contrast, model time steps are on the order of months. Due to these disparate time scales, we use the following procedure to estimate the measurement mean $\boldsymbol{\ell_0}$ and covariance matrix R on a time scale more appropriate for the ice sheet model.

We define a Gaussian process prior of "candidate" glacier length histories $\ell_p(t)$ as follows. The mean function $\hat{\ell_p}(t)$ is obtained by linearly interpolating between glacier

length observations. The Brownian covariance kernel for the Gaussian process is defined by

$$k_p(t, t') = \sigma_\ell^2 \min(t, t'). \tag{3.29}$$

Candidate retreat histories are generated by drawing random samples from the Gaussian process. The Brownian covariance kernel results in random glacier length histories that are somewhat noisy, but correlated over shorter time scales (Figure **??**). Candidate length histories are resampled so that the mean moraine formation times and uncertainties match the observations in Young et al. (view). Hence, highly implausible candidate histories are rejected. The average length and variance of this culled set of samples is computed at a series of time slices to obtain a plausible measurement mean $\boldsymbol{\ell_0}$ and diagonal measurement covariance matrix R (Figure 3.4).

Iterative Optimization Procedure

Optimizations are conducted in multiple passes. In the first pass, the measurement covariance matrix R is multiplied by a factor of 1/4 so that the measurements are initially weighted more than the prior. This produces a reasonable fit to the data, even given a poor initial estimate of ΔP. The optimal precipitation anomaly from a given iteration is used as the prior mean in the next iteration. We use the same prior covariance matrix P_0 for regularization in each iteration. After two to three iterations, modeled and observed terminus positions match within measurement uncertainty (Section 3.3). In our experience, the results of iteration are not dependent on the choice of prior mean in the first iteration, but we find that convergence can be improved by choosing a sensible initial guess as in Section 3.3.2.

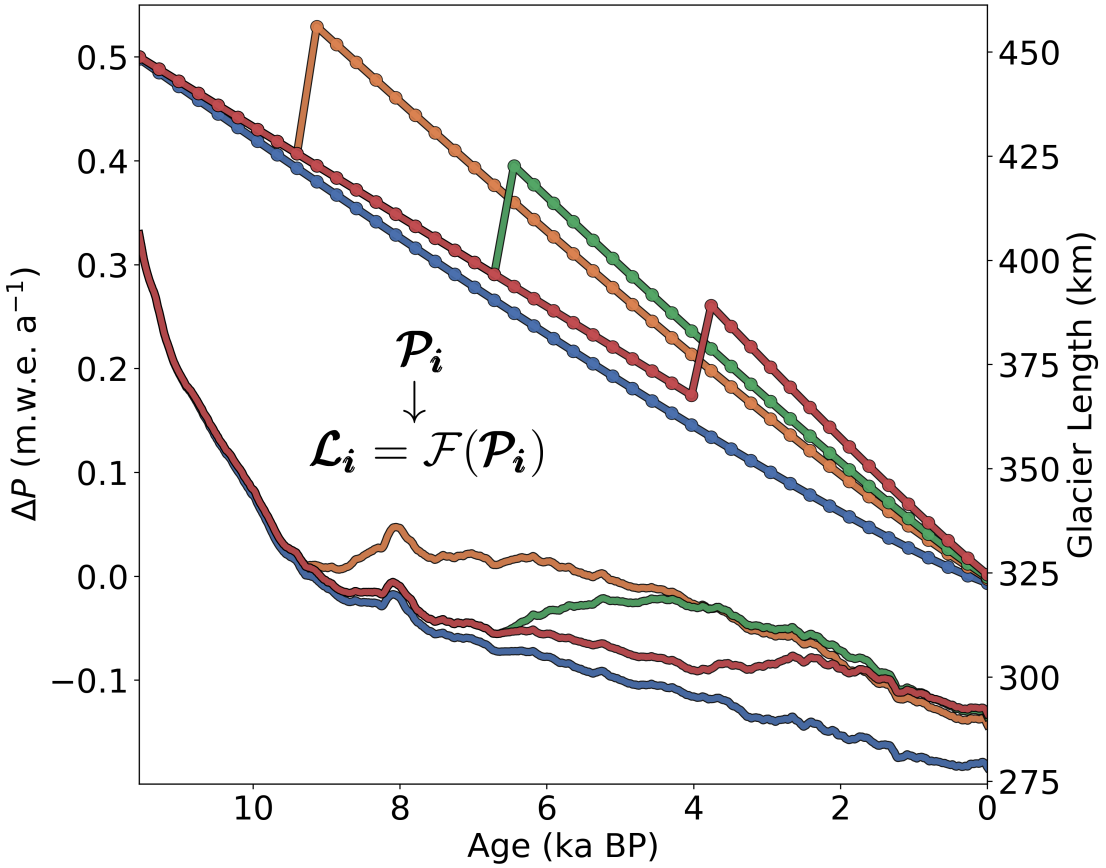

Figure 3.4: The measurement mean $\boldsymbol{\ell_0}$ (solid black line) and 95% confidence bands (gray shaded region) for the northern flowline are estimated by generating random retreat histories with the same mean moraine formation ages and variances as the observations. The green, blue, and orange lines represent four random plausible retreat histories. Red dots denote the estimated mean moraine formation ages, while red lines show 95% confidence intervals.

Approach to Sensitivity Testing

As described, the data assimilation method accounts for measurement but not model uncertainty. It can easily be extended to account for uncertainties in the ice flow and PDD model parameters. We define an augmented state vector

$$\boldsymbol{u} = [\boldsymbol{\Delta p},\ \boldsymbol{\theta}]^T \tag{3.30}$$

where $\boldsymbol{\theta}$ is a vector of scalar parameters including the natural logarithm of the rate factor for ice, the basal traction parameter, a parameter controlling precipitation scaling with temperature, and the PDD melt rate parameters for ice and snow

$$\boldsymbol{\theta} = [\ln(A),\ \beta^2,\ \lambda_p,\ \lambda_i,\ \lambda_s]^T. \tag{3.31}$$

The prior distribution for the augmented state vector is given by

$$\boldsymbol{u} \sim \mathcal{N}\left(\begin{bmatrix}\boldsymbol{\Delta p_o}\\ \boldsymbol{\theta_0}\end{bmatrix}, \begin{bmatrix}P_0 & 0\\ 0 & \Theta\end{bmatrix}\right) \tag{3.32}$$

where $\boldsymbol{\theta_0}$ is the parameter mean vector and Θ is a diagonal matrix containing parameter variances.

The unscented transform is applied to the augmented function

$$\boldsymbol{\ell} = \hat{\mathcal{F}}(\boldsymbol{u}) + \boldsymbol{\epsilon} \tag{3.33}$$

to obtain estimates of the joint distribution for $[\boldsymbol{\Delta p},\ \boldsymbol{\theta},\ \boldsymbol{\ell}]^T$ and the conditional distribution for $[\boldsymbol{\Delta p},\ \boldsymbol{\theta}]^T \mid \boldsymbol{\ell_0}$. Since parameters are included as state variables, sigma points reflect a variety of precipitation histories and parameter sets. A model run for a particular sigma point is initialized from an appropriate steady state using the parameter set for that point.

3.2.6 Model Initialization

Model runs are initialized by tuning the precipitation anomaly to obtain a steady state at 12.6 ka BP, with a margin position 5 km beyond the 11.6 ka BP moraine. We invert for a precipitation anomaly time series that forces a retreat of 5 km over 1000 years to obtain an initial ice sheet configuration with the correct terminus position at 11.6 ka BP

(Figure 3.5). This initialization procedure is intended to ease the ice sheet out of steady state in order to avoid strong transient effects at the beginning of model runs.

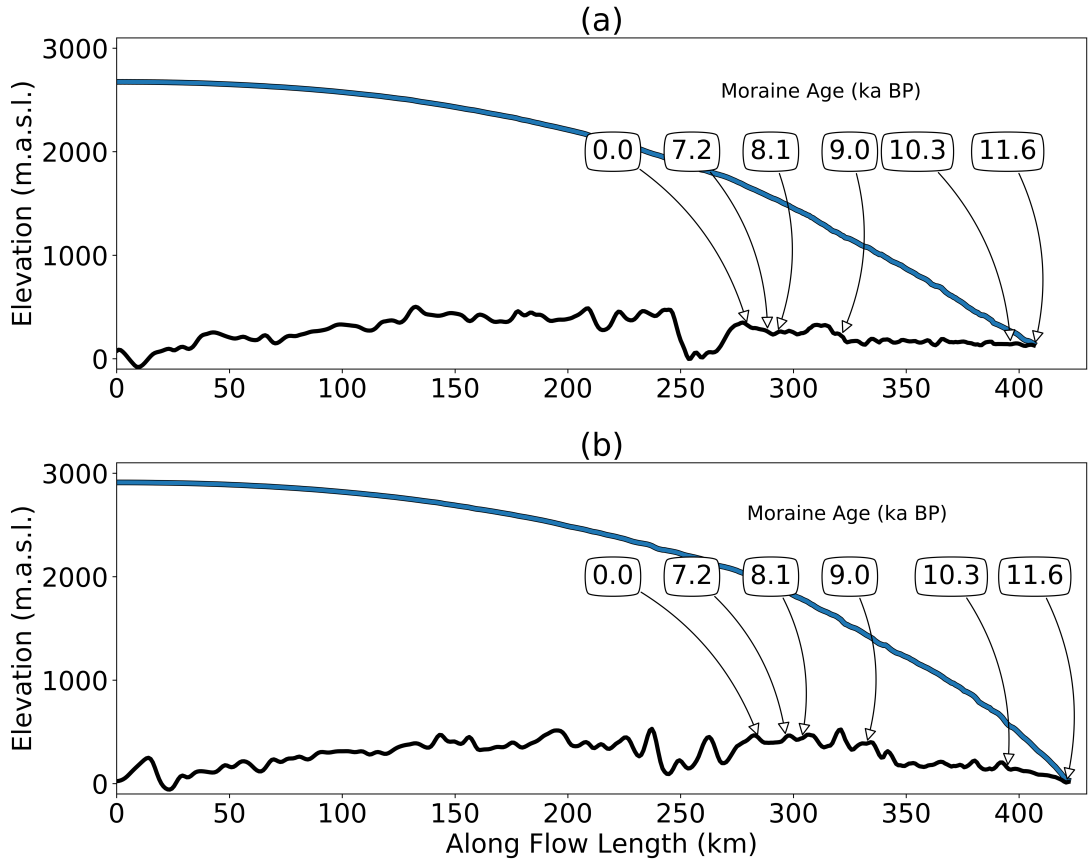

Figure 3.5: Initial ice sheet configurations for the northern (a) and southern (b) paleo-flowlines. Solid black and blue lines represent the bedrock elevation and ice surface respectively. Moraine positions are indicated by arrows with associated ages expressed in thousands of years before present.

3.3 Results

3.3.1 Reference Experiment

To assess the initial misfit between modeled and observed Holocene retreat, the model is forced with ΔT reconstructions from Buizert et al. (2018) and Dahl-Jensen et al. (1998)

and a zero precipitation anomaly. Precipitation is scaled with temperature according to Equation 3.4, neglecting possible influences from changing Arctic sea ice cover, atmospheric circulation, or other unknown climate factors. Modeled ice retreat is far more rapid than observed on both flowlines (Figure 3.8). Colder temperatures during the early Holocene (Figure 3.8 a) lead to a somewhat more plausible retreat history using the Dahl-Jensen et al. (1998) temperature forcing versus the Buizert et al. (2018) forcing. However, by 8 ka BP, ice has retreated inland of the present day margin in both reconstructions.

3.3.2 Precipitation Anomaly Inversions

We estimate precipitation anomalies on the northern and southern flowlines using both the Buizert et al. (2018) and Dahl-Jensen et al. (1998) temperature reconstructions. Given the rapid retreat in the reference experiment, we expect that a positive precipitation anomaly will be required to match observed terminus positions in the early Holocene. Therefore, in the first round of optimization, we assume a prior mean of the form

$$\Delta P = \frac{1}{2}(1 - \hat{\tau}) \tag{3.34}$$

where $\hat{\tau}$ is a rescaled time variable that increases from zero at 11.6 ka BP to one at 0 ka BP. The results of the iterative optimization procedure are insensitive to the prior mean selected in the first iteration. Using a sigma point scaling parameter $w_0 = 0.5$ for the Menegaz et al. (2011) sigma point set ensures that a wide region around the mean is explored in each iteration.

Positive precipitation anomalies are predicted throughout most of the Holocene for both temperature reconstructions (Figure 3.6). While differences between the northern and southern flowlines are relatively minor, there are significant differences in precipitation between the Buizert et al. (2018) and Dahl-Jensen et al. (1998) inversions. In the

Buizert et al. (2018) inversion, the largest precipitation anomalies (up to 1 m.w.e. a^{-1}) occur during the early Holocene. Precipitation remains relatively high during the HTM (10 - 6 ka BP), but dips before the 8.2 ka BP cold event. For the Dahl-Jensen et al. (1998) inversion, ΔP is relatively low during the early Holocene, but increases during the HTM (8.5 - 3 ka BP). Unlike the Buizert et al. (2018) inversion, there is an evident trend between HTM warming and increased snowfall (Figure 3.9).

Forcing the model with mean estimated precipitation anomalies yields plausible retreat histories on both flowlines. Modeled and observed retreat chronologies match within within uncertainty (Figure 3.8). A significant fraction of Holocene precipitation (typically $> 90\%$) falls as snow. Hence, a positive precipitation anomaly can be interpreted directly as additional snowfall / accumulation. Average HTM snowfall is around 35% higher than modern in both temperature reconstructions (Figure 3.9). However, overall trends in Holocene snowfall differ between reconstructions.

3.3.3 Sensitivity Testing

We assess the sensitivity of Holocene precipitation anomalies to modeling uncertainties by performing an HTM inversion using the methodology described in Section 3.2.5. To obtain accurate uncertainty estimates, we use a fifth order accurate sigma point set based on Li et al. (2017) (Appendix 3.A), as we find that the second order Menegaz et al. (2011) set likely underestimates covariance. Inversions are performed on the northern flowline using the Buizert et al. (2018) temperature reconstruction. Model runs are initialized from steady states around at 10.5 ka BP, 500 years prior to the Buizert et al. (2018) HTM. Prior and posterior parameter values are reported in Table 3.3.

Mean HTM precipitation anomalies are within 2 cm.w.e. a^{-1} of the inversion presented in section 3.3.2 (Figure 3.10). Parameter uncertainties contribute to uncertainty in ΔP. Overall, however, temperature uncertainty is far more significant than uncertainty in model parameters. Differences in model initialization do not significantly

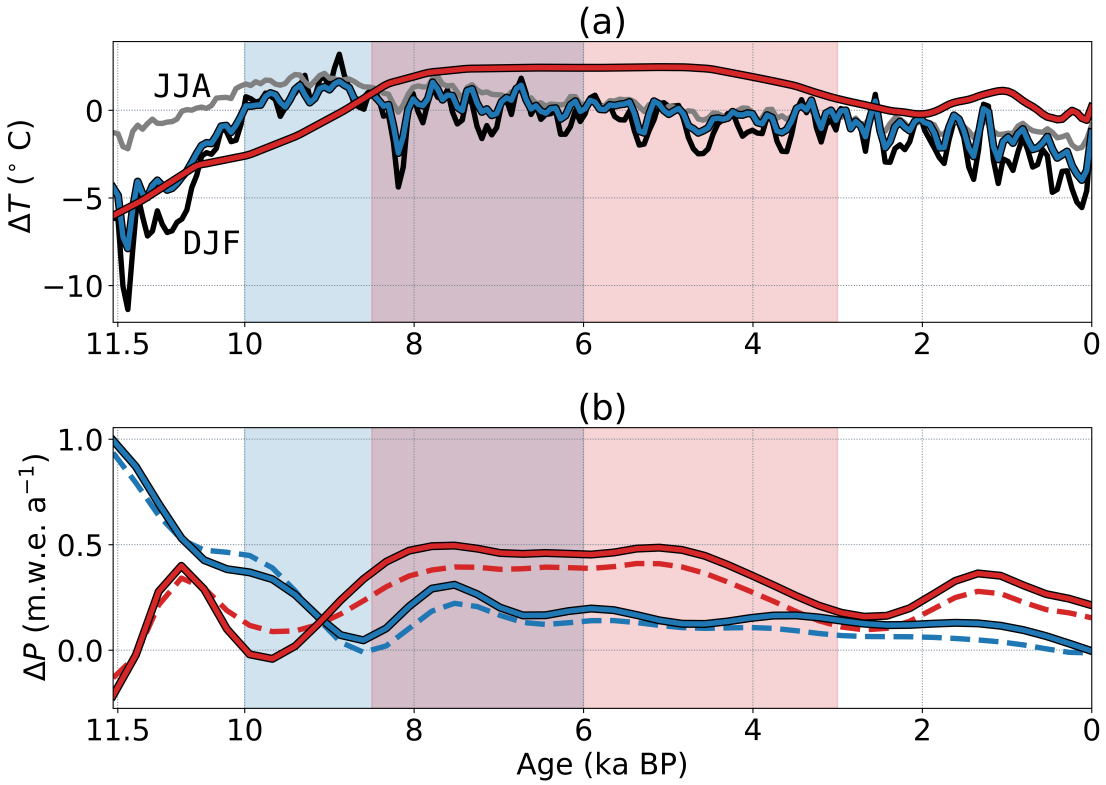

Figure 3.6: (a) Buizert et al. (2018) and Dahl-Jensen et al. (1998) mean annual temperature anomalies are shown as blue and red lines respectively. Gray and Black lines show average December, January, February (DJF) and June, July, August (JJA) temperature anomalies for the Buizert et al. (2018) reconstruction. Shaded blue / pink regions demarcate the extent of the HTM for the Buizert et al. (2018) and Dahl-Jensen et al. (1998) reconstructions. (b) Estimated precipitation anomaly histories for the Buizert et al. (2018) and Dahl-Jensen et al. (1998) inversions are shown by blue and red lines respectively. Solid lines show estimates for the northern flowline, while dashed lines are for the southern flowline.

impact the results of the inversion. Although sensitivity tests are initialized from steady states at 10.5 ka BP, while inversions in Section 3.3.2 are initialized from a transient state at 11.6 ka BP, the mean HTM precipitation anomalies are nearly identical. Estimated posterior parameter values are also similar to the assumed prior values (Table 3.3).

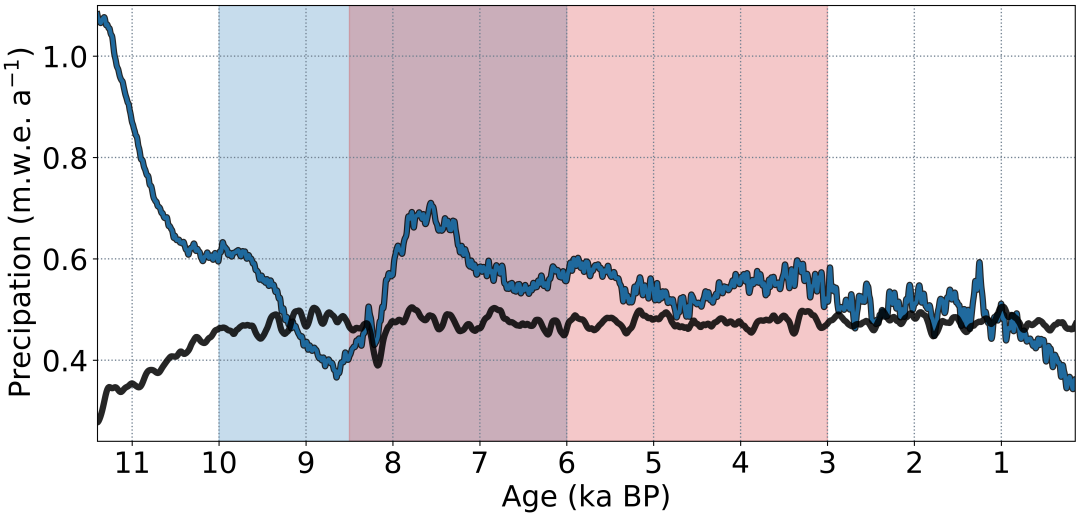

Figure 3.7: Average precipitation (both solid and liquid) on the northern flowline from the Buizert et al. (2018) reconstruction (black line), which is based on the TraCE-21ka coupled ocean-atmosphere general circulation model of the last deglaciation, versus estimated precipitation derived in this work based on reconciling the modeled and observed retreat chronologies (blue line).

3.4 Discussion

We infer changes in Holocene precipitation in the Kangerlussuaq region of western Greenland using a new chronology of ice sheet terminus position from Young et al. (view) and an inverse modeling procedure based on the unscented transform. We find that scaling precipitation with temperature via the Clausius–Clapeyron equation (Equation 3.4) results in excessively fast retreat during the early Holocene for both the Buizert et al.

Table 3.3: Summary of primary model parameters used in this work. Default values are provided where applicable. Prior parameter uncertainties assumed for the sensitivity test are shown in the 2σ column.

Description	**Symbol**	**Prior Mean**	**2σ Range**	**Posterior Mean**	**Units**
Ablation rate, snow	λ_s	5×10^{-3}	3 - 7 $\times10^{-3}$	2.8 $\times10^{-3}$	m.w.e. C^{-1} d $^{-1}$
Ablation rate, ice	λ_i	8×10^{-3}	6 - 10 $\times10^{-3}$	8.9 $\times10^{-3}$	m.w.e. C^{-1} d^{-1}
Precipitation param.	λ_p	7 $\times10^{-2}$	5 - 9 $\times10^{-2}$	9.8 $\times10^{-2}$	C^{-1}
Rate factor	A	3.5 $\times10^{-25}$	2.1 - 5.7 $\times10^{-25}$	2 $\times10^{-25}$	s^{-1} Pa^{-3}
Basal traction	β^2	1.2×10^{-3}	1.1 - 1.3 $\times10^{-3}$	1.2 $\times10^{-3}$	Pa a m^{-1}

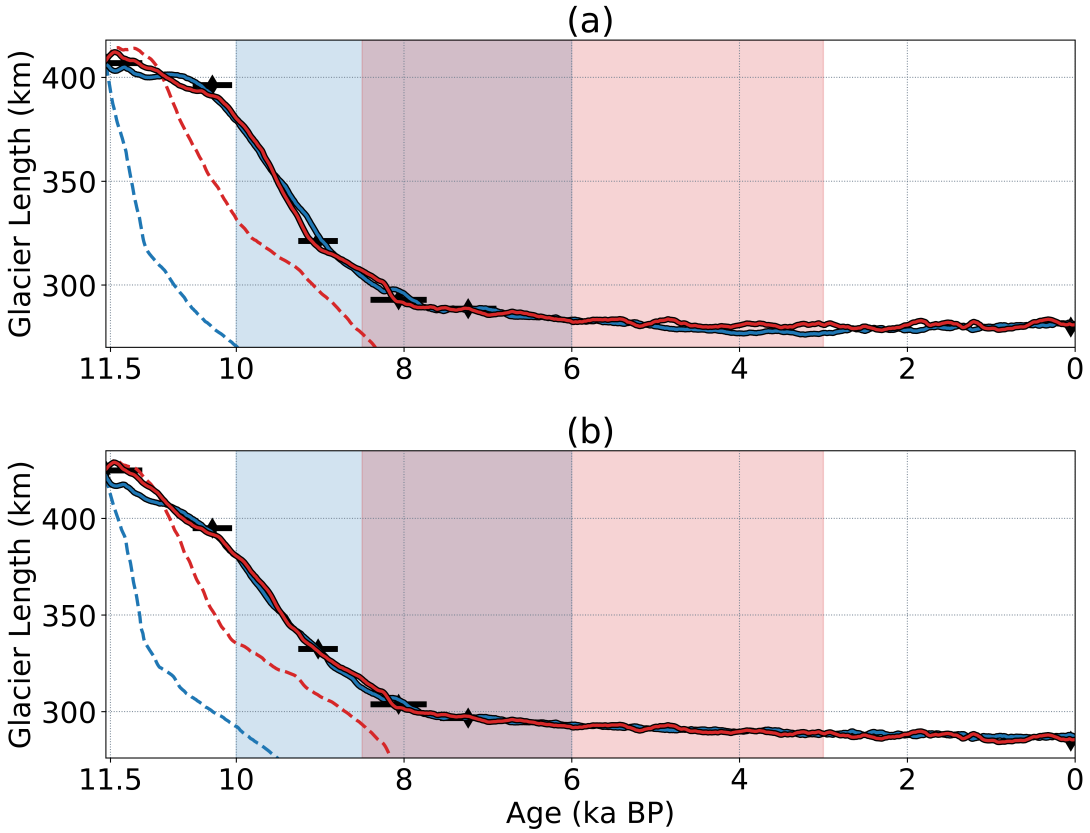

Figure 3.8: Modeled retreat histories for the northern (a) and southern (b) flowlines using a variety of ΔT and ΔP forcings. Blue and red lines show modeled retreat using Buizert et al. (2018) and Dahl-Jensen et al. (1998) temperature forcings respectively. Dashed lines show the results of forcing the model with $\Delta P = 0$, while solid lines show the results of using optimal estimated precipitation anomalies. Black diamonds / bars show reconstructed terminus positions along with 95% confidence intervals. Shaded blue / pink regions demarcate the extent of the HTM for the Buizert et al. (2018) and Dahl-Jensen et al. (1998) reconstructions respectively.

(2018) and Dahl-Jensen et al. (1998) temperature reconstructions. Thus, temperature driven changes in precipitation / accumulation alone are not sufficient to reproduce the observed pattern of retreat. Inversions show that adding precipitation throughout the Holocene and specifically during the HTM yields a good fit to observations (Figures 3.6, 3.8). Since a large fraction of precipitation falls as snow, a positive precipitation anomaly can be interpreted fairly directly as an increase in accumulation beyond what

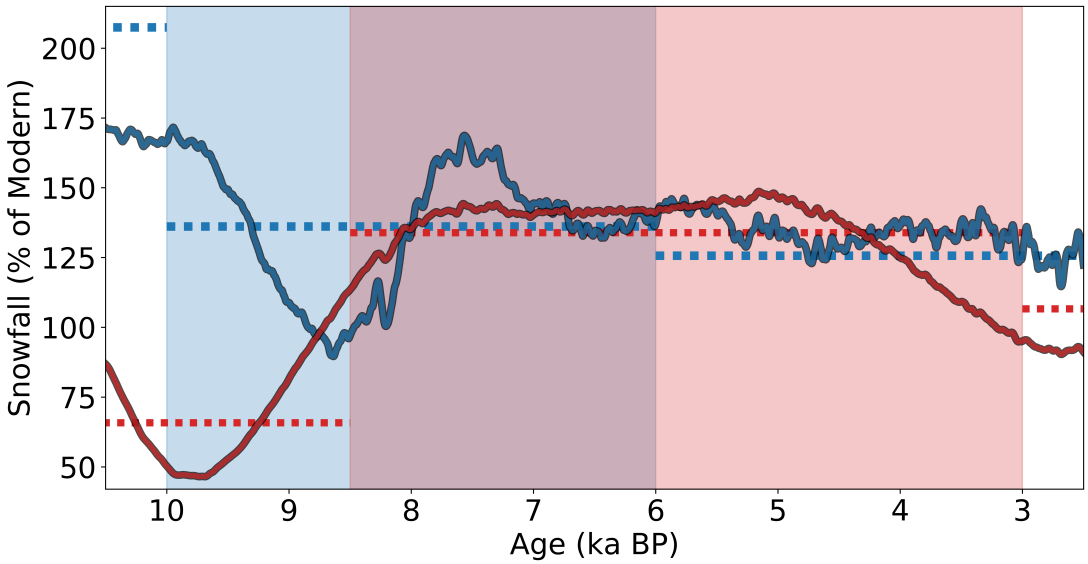

Figure 3.9: HTM snowfall averaged across the northern and southern flowlines for the Buizert et al. (2018) (solid blue line) and Dahl-Jensen et al. (1998) (solid red line) inversions. Shaded blue / pink regions demarcate the extent of the HTM for the Buizert et al. (2018) and Dahl-Jensen et al. (1998) reconstructions respectively. Dashed lines show pre-HTM, HTM, and post-HTM average snowfall for each inversion.

would be expected from temperature changes alone.

There are considerable differences in predicted precipitation anomalies depending on the assumed temperature history. Inversions using the Buizert et al. (2018) temperature reconstruction show generally decreasing snowfall through the Holocene. Due to high snowfall in the early Holocene (nearly 100% higher than modern) and a dip in HTM precipitation associated with the 8.2 ka BP cold event, average HTM snowfall roughly matches the overall Holocene average, which is about 35% above modern. In contrast, inversions using the Dahl-Jensen et al. (1998) temperature reconstruction show a clear trend between HTM warming and increased snowfall (Figure 3.9). This trend could be interpreted as a transient increase in snowfall due to reduced Arctic sea ice cover or changes in atmospheric circulation during the HTM.

A large positive ΔP correction during the early Holocene in the Buizert et al. (2018) inversion likely reflects the dependence of precipitation on temperature. Low temper-

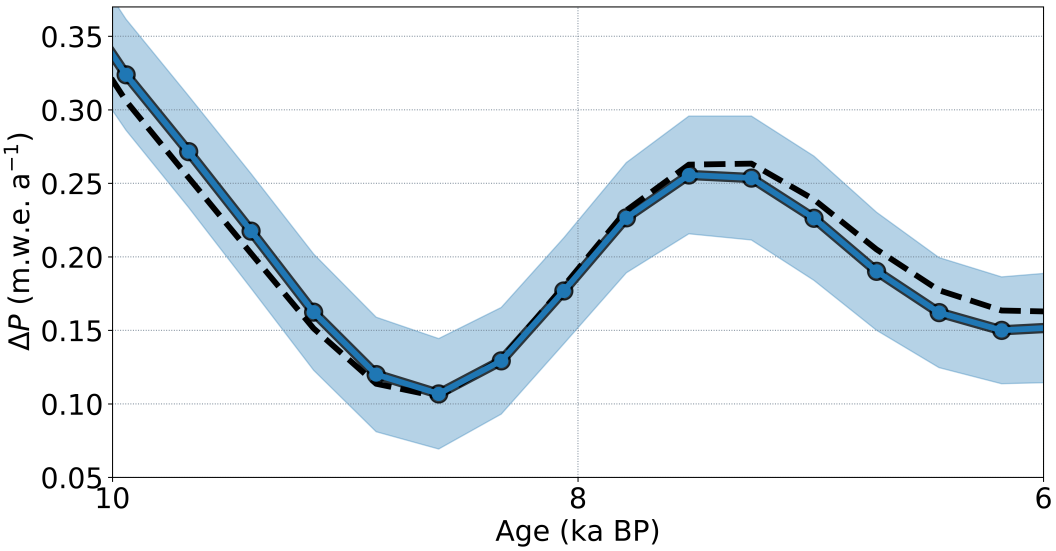

Figure 3.10: The blue line / shaded region show the estimated mean ΔP and 95% confidence bands for the sensitivity test, accounting for uncertainty in a number of ice-flow and PDD model parameters. The black dashed line shows the mean estimated ΔP from a previous inversion assuming no uncertainty in model parameters.

atures during the early Holocene result in low precipitation. Without an additional moisture source to increase snowfall, the ice sheet retreats far more rapidly than observed. In the Dahl-Jensen et al. (1998) reconstruction, warming occurs more gradually in the early Holocene. Accumulation and ablation are more closely balanced, resulting in a smaller precipitation anomaly correction from 11.6 to 10 ka BP.

When interpreting results of precipitation inversions, it is important to consider that the Buizert et al. (2018) and Dahl-Jensen et al. (1998) reconstructions are obtained using different methodologies. The Greenland-wide Buizert et al. (2018) reconstruction is obtained by merging the TraCE-21ka coupled ocean-atmosphere general circulation model of the last deglaciation (Liu et al., 2009; He et al., 2013) with borehole temperature reconstructions at GISP2, NGRIP, and NEEM. Our estimated precipitation history in the Kangerlussuaq region is significantly different from TraCE-21ka, particularly during the early Holocene and parts of the HTM (Figure 3.7). In contrast to Buizert et al.

(2018), the Dahl-Jensen et al. (1998) temperature reconstruction at GRIP offers only a pointwise estimate containing no explicit spatial or seasonal information.

While the Buizert et al. (2018) temperature reconstruction is arguably more suitable for our purposes, since it resolves spatial and seasonal patterns in ΔT, there is still considerable uncertainty in temperature, particularly near the ice margins. Despite this, there is some consensus between the Buizert et al. (2018) and Dahl-Jensen et al. (1998) inversions. For example, average HTM snowfall is roughly 35% higher than modern in both cases (Figure 3.9).

Predicted HTM precipitation anomalies are not particularly sensitive to uncertainties in the ice sheet or PDD model parameters, or to the initialization procedure. In the sensitivity test presented in Section 3.3.3, model runs are initialized using steady states at 10.5 ka BP. Runs in the full Holocene inversions in Section 3.3.2, which use fixed parameter sets, are initialized from a transient state at 11.6 ka BP. Even considering these differences in model initialization, estimated HTM precipitation anomalies are comparable in all inversions (Figure 3.10). Additionally, ΔP does not appear to be sensitive to uncertainties in bedrock geometry, as inversions conducted with a static bedrock geometry yielded similar results to inversions accounting for isostatic uplift.

3.4.1 Conclusions

The Unscented Transform as a Data Assimilation Method

Significant strides have been made in time-dependent data assimilation in glaciology using adjoint based methods. Goldberg and Heimbach (2013) infer the initial thickness and basal conditions for a synthetic ice sheet given snapshots of ice thickness at discrete times. Larour et al. (2014) demonstrate a data assimilation framework within the Ice Sheet System Model (ISSM), capable of obtaining temporal estimates of surface mass balance and basal friction given surface altimetry.

In contrast to adjoint based approaches, the unscented transform (UT) does not require computing the Jacobian or Hessian of an objective function, or special checkpointing code for time-dependent problems. Adjoint based methods are advantageous for extremely high-dimensional problems, as the required number of model runs is independent of the number of parameters. However, the UT provides more accurate uncertainty estimates than linearization (Julier and Uhlmann, 1997). Hessian information can be used to improve uncertainty estimates (Isaac et al., 2015). However, this methodology uses purely local approximations to the nonlinear function around the maximum a posteriori probability (MAP) estimator, which may affect the quality of uncertainty estimates.

The unscented transform has advantages over Markov chain Monte Carlo methods for inference problems with a relatively small number of unknown parameters (< 1000 or so parameters). In this work, we optimize for $n = 44$ parameters representing precipitation anomaly values at discrete points in time. Since function evaluations at each sigma point are independent, the UT is trivially parallelizable. Consequently, on a high end desktop, the iterative optimization process presented in Section 3.2.5 takes roughly the same amount of time as performing three successive forward model runs.

MCMC methods can be parallelized to some extent by utilizing multiple interacting Markov chains running in parallel (e.g. Chowdhury and Jermaine, 2018) or by combining samples from independent chains in a post processing step (e.g. Neiswanger et al., 2013). Nonetheless, computational bottlenecks persist in MCMC methods since individual Markov chains are inherently serial. Consequently, UT approximations to the posterior distribution can be generated hundreds to thousands of times faster for small parameter sets.

A drawback of the UT is that its accuracy is inherently limited by using a predetermined number of sample points. In our case, for example, using a minimal set of $n + 1$ sigma points for n unknown parameters yields accurate mean estimates but appears to

underestimate covariance when compared to a higher order cubature method. Without testing multiple sigma point sets and scaling parameters, it can be difficult to assess the accuracy of UT estimates of the posterior. MCMC methods, in contrast, can provide arbitrarily accurate estimates of the posterior given sufficient computation time. Moreover, they can resolve the full posterior distribution rather than computing its moments as in the UT.

An alternative to traditional MCMC methods is to use surrogate models or emulators (Gong and Duan, 2017). Here, a computationally inexpensive surrogate model is trained to approximate the output of a more complex model function. The surrogate model can then be used in place of the full model for the purpose of MCMC sampling, significantly reducing the overall computational cost. A few types of surrogate models have already been applied to glaciological problems including deep neural networks (Tarasov et al., 2012) and Gaussian processes (e.g. Chang et al., 2016; Pollard et al., 2016).

Surrogate models require an initial training phase. Pollard et al. (2016), for example, perform 625 ice sheet model runs using combinations of four unknown simulation parameters. A Gaussian process surrogate model is then fitted to this training data in order to interpolate the model in parameter space for inference. The number and selection of training points significantly affects the performance of the surrogate model.

Interestingly, there is a strong connection between the unscented transform and Gaussian process surrogate models. It can be shown that sigma points for the UT are optimal training points for a Gaussian process surrogate model in the sense of minimizing the variance of the expected value of the posterior distribution (Sarkkä et al., 2016). While the details are technical, one can think of UT sigma points as optimal training points given that (i) the prior distribution is a multivariate Gaussian and (ii) the Gaussian process surrogate model has a polynomial covariance function.

Modeling Conclusions

Our work follows a number of previous observationally constrained paleo ice sheet modeling studies (e.g. Tarasov and Peltier, 2002; Lecavalier et al., 2014; Calov et al., 2015). Perhaps most relevant to this work is Lecavalier et al. (2014), who model the deglaciation of Greenland from the Last Glacial Maximum using a 3-D thermomechanically coupled ice sheet model. Model runs in Lecavalier et al. (2014) are informed by constraints on relative sea level, ice core thinning, and LGM ice sheet extent.

In contrast to previous modeling studies, the computational efficiency of the flowline model outlined in Brinkerhoff et al. (2017) makes time-dependent data-assimilation, sensitivity testing, and robust uncertainty estimation tractable. Sensitivity testing indicates that estimated precipitation is insensitive to parameter uncertainties in the PDD and ice-dynamics models. This conclusion supports earlier findings showing that modeled Holocene retreat in land terminating sectors of the GrIS is more sensitive to surface mass balance than other factors like the flow law or basal sliding (Cuzzone et al., 2019; Lecavalier et al., 2014).

A drawback of our modeling approach is that we cannot account for inherently map plane effects such as changes in ice flow direction, or convergent / divergent flow in or out of the assumed flow path. These factors likely contribute to small discrepancies in estimated precipitation anomalies between the northern and southern flowlines (Figure 3.6). Beyond computational efficiency, there are number of reasons why a flowline model is appropriate for our purposes. The modern flow field near Kangerlussuaq can be characterized by relatively simple east-to-west flow, and there is an absence of strongly convergent flow into outlet glaciers. Given the low bedrock relief in the region, and the surface mass balance dominated retreat pattern (Van Tatenhove et al., 1996; Cuzzone et al., 2019), it is reasonable to assume that the flow regime was similar during the Holocene.

In this work, we do not treat temperature as a random variable with its own covari-

ance structure. However, differences between the Buizert et al. (2018) and Dahl-Jensen et al. (1998) inversions indicate that temperature is the dominant source of uncertainty in ΔP. This result underscores the importance of generating improved, regionally specific, temperature reconstructions constrained by proxy records. More regionally specific estimates of temperature would help to decrease uncertainty in the estimated precipitation history.

Despite lingering uncertainties, our modeling results indicate that the Holocene thermal maximum was accompanied by elevated snowfall, which slowed ice retreat in the Kangerlussuaq region of the GrIS. Inversions conducted using both the Buizert et al. (2018) and Dahl-Jensen et al. (1998) temperature reconstructions show average HTM snowfall around 35% higher than modern. More specifically, in the Dahl-Jensen et al. (1998) inversion, there is a clear trend between HTM warming and increased accumulation, which could be interpreted as transient increase in precipitation due to reduced Arctic sea ice cover or changes in atmospheric circulation.

Appendices

3.A A Higher Order Method for Estimating Covariance

Estimating the mean and covariance of the posterior distribution requires approximating Gaussian weighted expectation integrals of the form

$$E[\mathcal{F}(\boldsymbol{x})] = \int_{\mathbb{R}^n} \mathcal{F}(\boldsymbol{x})\mathcal{N}(\boldsymbol{x} \mid \mathbf{0}, I)\, d\boldsymbol{x} \tag{3.35}$$

via numerical integratation rules, also called cubature rules, which approximate the expectation integral as a weighted sum

$$E[\mathcal{F}(\boldsymbol{x})] \approx Q[\mathcal{F}(\boldsymbol{x})] = \sum_{i=1}^{N} w_i \mathcal{F}(\boldsymbol{\chi_i}). \tag{3.36}$$

Here, the notation $\mathcal{N}(\boldsymbol{x} \mid \mathbf{0}, I)$ refers to a Gaussian probability density function evaluated at the point $\boldsymbol{x}$. General Gaussian weight functions $\mathcal{N}(\boldsymbol{x} \mid \boldsymbol{x_0}, P_x)$ are handled by changing variables. Letting $\sqrt{P_x}$ be a matrix square root of the covariance matrix, we have

$$\begin{aligned} &\int_{\mathbb{R}^n} \mathcal{F}(\boldsymbol{x})\mathcal{N}(\boldsymbol{x} \mid \boldsymbol{x_0}, P_x)\, d\boldsymbol{x} \\ &= \int_{\mathbb{R}^n} \mathcal{F}(\boldsymbol{x_0} + \sqrt{P_x}\,\boldsymbol{\xi})\mathcal{N}(\boldsymbol{\xi} \mid \mathbf{0}, I)\, d\boldsymbol{\xi}. \end{aligned} \tag{3.37}$$

Cubature rules, including the unscented transform, are constructed to exactly inte-

grate polynomial functions $\mathcal{F}(\boldsymbol{x})$ up to a certain degree d. Suppose that $\boldsymbol{x} = [x_1, x_2, \cdots, x_n]^T$ is a point in $\mathbb{R}^n$. A monomial of degree d refers to a function $x_1^{i_1} x_2^{i_2} \cdots x_n^{i_n}$ where the exponents are non-negative integers that sum to d. A polynomial of degree d is a linear combination of monomials with highest degree d.

Li et al. (2017) describe a fifth-order cubature rule using fully symmetric sets of sigma points. A set $X = \{\boldsymbol{\chi_1}, \boldsymbol{\chi_2}, \cdots, \boldsymbol{\chi_N}\}$ is fully symmetric if it is closed under the operations of coordinate position and sign permutations. Their cubature rule has the form

$$\begin{aligned} Q[\mathcal{F}(\boldsymbol{x})] &= w_1 \mathcal{F}(0, 0, \cdots, 0) \\ &+ w_2 \sum_{\text{full sym}} \mathcal{F}(\lambda, 0, \cdots, 0) \\ &+ w_3 \sum_{\text{full sym}} \mathcal{F}(\lambda, \lambda, 0, \cdots, 0). \end{aligned} \tag{3.38}$$

The notation $\sum_{\text{full sym}} \mathcal{F}(\cdot)$ refers to a sum of the function $\mathcal{F}$ evaluated at all points in the fully symmetric set generated by the given point.

Due to the symmetry of the sigma points and the Gaussian weight function, all moments (that is, integrals of Gaussian weighted monomial functions) containing an odd order exponent are automatically satisfied. Exploiting this fact, and the symmetries of the sigma points, it can be shown that satisfying the remaining moment constraint equations up the fifth order reduces to solving the following system of four equations in four unknowns w_1, w_2, w_3 and λ

$$\begin{aligned} E[1] &= w_1 + 2n w_2 + 2n(n-1) w_3 \\ E[x_i^2] &= 2\lambda^2 w_2 + 4(n-1)\lambda^2 w_3 \\ E[x_i^4] &= 2\lambda^4 w_2 + 4(n-1)\lambda^4 w_3 \\ E[x_i^2 x_j^2] &= 4\lambda^4 w_3. \end{aligned} \tag{3.39}$$

By slightly modifying this cubature rule

$$\begin{aligned} Q[\mathcal{F}(\boldsymbol{x})] &= w_1 \mathcal{F}(0, 0, \cdots, 0) \\ &+ w_2 \sum_{\text{full sym}} \mathcal{F}(\lambda_1, 0, \cdots, 0) \\ &+ w_3 \sum_{\text{full sym}} \mathcal{F}(\lambda_2, \lambda_2, 0, \cdots, 0) \end{aligned} \tag{3.40}$$

we introduce a new free parameter λ_2 that allows scaling of the sigma points about the mean. The new moment constraint equations become

$$\begin{aligned} E[1] &= w_1 + 2nw_2 + 2n(n-1)w_3 \\ E[x_i^2] &= 2\lambda_1^2 w_2 + 4(n-1)\lambda_2^2 w_3 \\ E[x_i^4] &= 2\lambda_1^4 w_2 + 4(n-1)\lambda_2^4 w_3 \\ E[x_i^2 x_j^2] &= 4\lambda_2^4 w_3. \end{aligned} \tag{3.41}$$

Using that $E[1] = 1$, $E[x_i^2] = 1$, $E[x_i^4] = 3$, and $E[x_i^2 x_j^2] = 1$ we obtain

$$\begin{aligned} \lambda_1 &= \frac{\lambda_2 \sqrt{n-4}}{n - \lambda_2^2 - 1} \\ w_2 &= \frac{4-n}{2\lambda_1^4} \\ w_3 &= \frac{1}{4\lambda_2^2} \\ w_1 &= 1 - 2nw_2 - 2n(n-1)w_3 \end{aligned} \tag{3.42}$$

with $n > 4$ and $n - \lambda_2^2 - 1 \neq 0$. A drawback of the original cubature rule, as well our modified version here, is that it requires negative weights, which can lead to numerical instability.

Bibliography

Abe-Ouchi, A., Segawa, T., and Saito, F. (2007). Climatic conditions for modelling the Northern Hemisphere ice sheets throughout the ice age cycle.

Alley, R. B., Meese, D. A., Shuman, C. A., Gow, A. J., Taylor, K. C., Grootes, P. M., White, J. W., Ram, M., Waddington, E. D., Mayewski, P. A., and Zielinski, G. A. (1993). Abrupt increase in Greenland snow accumulation at the end of the Younger Dryas event. *Nature*.

Bahadory, T. and Tarasov, L. (2018). LCice 1.0-a generalized Ice Sheet System Model coupler for LOVECLIM version 1.3: Description, sensitivities, and validation with the Glacial Systems Model (GSM version D2017.aug17). *Geoscientific Model Development*.

Bintanja, R. and Selten, F. M. (2014). Future increases in Arctic precipitation linked to local evaporation and sea-ice retreat. *Nature*.

Blatter, H. (1995). Velocity and stress fields in grounded glaciers: a simple algorithm for including deviatoric stress gradients. *Journal of Glaciology*.

Box, J. E. (2013). Greenland ice sheet mass balance reconstruction. Part II: Surface mass balance (1840-2010). *Journal of Climate*.

Brinkerhoff, D., Truffer, M., and Aschwanden, A. (2017). Sediment transport drives tidewater glacier periodicity. *Nature Communications*.

Buizert, C., Keisling, B. A., Box, J. E., He, F., Carlson, A. E., Sinclair, G., and DeConto, R. M. (2018). Greenland-Wide Seasonal Temperatures During the Last Deglaciation. *Geophysical Research Letters*.

Calov, R., Robinson, A., Perrette, M., and Ganopolski, A. (2015). Simulating the Greenland ice sheet under present-day and palaeo constraints including a new discharge parameterization. *Cryosphere*.

Caron, L., Ivins, E. R., Larour, E., Adhikari, S., Nilsson, J., and Blewitt, G. (2018). GIA Model Statistics for GRACE Hydrology, Cryosphere, and Ocean Science. *Geophysical Research Letters*.

Chang, W., Haran, M., Applegate, P., and Pollard, D. (2016). Calibrating an Ice Sheet Model Using High-Dimensional Binary Spatial Data. *Journal of the American Statistical Association*.

Chib, S. and Greenberg, E. (1995). Understanding the metropolis-hastings algorithm. *American Statistician*.

Chowdhury, A. and Jermaine, C. (2018). Parallel and Distributed MCMC via Shepherding Distributions. *Proceedings of the Twenty-First International Conference on Artificial Intelligence and Statistics*, 84:1819–1827.

Cuzzone, J. K., Schlegel, N. J., Morlighem, M., Larour, E., Briner, J. P., Seroussi, H., and Caron, L. (2019). The impact of model resolution on the simulated Holocene retreat of the southwestern Greenland ice sheet using the Ice Sheet System Model (ISSM). *Cryosphere*.

Dahl-Jensen, D., Mosegaard, K., Gundestrup, N., Clow, G. D., Johnsen, S. J., Hansen, A. W., and Balling, N. (1998). Past temperatures directly from the Greenland Ice Sheet. *Science*.

Goldberg, D. N. and Heimbach, P. (2013). Parameter and state estimation with a time-dependent adjoint marine ice sheet model. *Cryosphere*.

Gong, W. and Duan, Q. (2017). An adaptive surrogate modeling-based sampling strategy for parameter optimization and distribution estimation (ASMO-PODE). *Environmental Modelling and Software*, 95:61–75.

He, F., Shakun, J. D., Clark, P. U., Carlson, A. E., Liu, Z., Otto-Bliesner, B. L., and Kutzbach, J. E. (2013). Northern Hemisphere forcing of Southern Hemisphere climate during the last deglaciation. *Nature*.

Isaac, T., Petra, N., Stadler, G., and Ghattas, O. (2015). Scalable and efficient algorithms for the propagation of uncertainty from data through inference to prediction for large-scale problems, with application to flow of the Antarctic ice sheet. *Journal of Computational Physics*.

Johannesson, T., Sigurdsson, O., Laumann, T., and Kennett, M. (1995). Degree-day glacier mass-balance modelling with applications to glaciers in Iceland, Norway and Greenland. *Journal of Glaciology*.

Julier, S. J. and Uhlmann, J. K. (1997). New extension of the Kalman filter to nonlinear systems. *Int Symp AerospaceDefense Sensing Simul and Controls*.

Kaufman, D. S., Ager, T. A., Anderson, N. J., Anderson, P. M., Andrews, J. T., Bartlein, P. J., Brubaker, L. B., Coats, L. L., Cwynar, L. C., Duvall, M. L., Dyke, A. S., Edwards, M. E., Eisner, W. R., Gajewski, K., Geirsdóttir, A., Hu, F. S., Jennings, A. E., Kaplan, M. R., Kerwin, M. W., Lozhkin, A. V., MacDonald, G. M., Miller, G. H., Mock, C. J., Oswald, W. W., Otto-Bliesner, B. L., Porinchu, D. F., Rühland, K., Smol, J. P., Steig, E. J., and Wolfe, B. B. (2004). Holocene thermal maximum in the western Arctic (0-180 W). *Quaternary Science Reviews*.

Kobashi, T., Menviel, L., Jeltsch-Thömmes, A., Vinther, B. M., Box, J. E., Muscheler, R., Nakaegawa, T., Pfister, P. L., Döring, M., Leuenberger, M., Wanner, H., and Ohmura, A. (2017). Volcanic influence on centennial to millennial Holocene Greenland temperature change. *Scientific Reports*.

Larour, E., Utke, J., Csatho, B., Schenk, A., Seroussi, H., Morlighem, M., Rignot, E., Schlegel, N., and Khazendar, A. (2014). Inferred basal friction and surface mass

balance of the Northeast Greenland Ice Stream using data assimilation of ICESat (Ice Cloud and land Elevation Satellite) surface altimetry and ISSM (Ice Sheet System Model). *Cryosphere*.

Lecavalier, B. S., Milne, G. A., Simpson, M. J., Wake, L., Huybrechts, P., Tarasov, L., Kjeldsen, K. K., Funder, S., Long, A. J., Woodroffe, S., Dyke, A. S., and Larsen, N. K. (2014). A model of Greenland ice sheet deglaciation constrained by observations of relative sea level and ice extent. *Quaternary Science Reviews*, 102:54–84.

Li, Z., Yang, W., Ding, D., and Liao, Y. (2017). A Novel Fifth-Degree Cubature Kalman Filter for Real-Time Orbit Determination by Radar. *Mathematical Problems in Engineering*.

Liu, Z., Otto-Bliesner, B. L., He, F., Brady, E. C., Tomas, R., Clark, P. U., Carlson, A. E., Lynch-Stieglitz, J., Curry, W., Brook, E., Erickson, D., Jacob, R., Kutzbach, J., and Cheng, J. (2009). Transient simulation of last deglaciation with a new mechanism for bolling-allerod warming. *Science*.

Marcott, S. A., Shakun, J. D., Clark, P. U., and Mix, A. C. (2013). A reconstruction of regional and global temperature for the past 11,300 years. *Science*, 339(6124):1198–1201.

Menegaz, H. M., Ishihara, J. Y., and Borges, G. A. (2011). A new smallest sigma set for the Unscented Transform and its applications on SLAM. In *Proceedings of the IEEE Conference on Decision and Control*.

Miller, G. H., Brigham-Grette, J., Alley, R. B., Anderson, L., Bauch, H. A., Douglas, M. S., Edwards, M. E., Elias, S. A., Finney, B. P., Fitzpatrick, J. J., Funder, S. V., Herbert, T. D., Hinzman, L. D., Kaufman, D. S., MacDonald, G. M., Polyak, L., Robock, A., Serreze, M. C., Smol, J. P., Spielhagen, R., White, J. W., Wolfe, A. P., and

Wolff, E. W. (2010). Temperature and precipitation history of the Arctic. *Quaternary Science Reviews*.

Morlighem, M., Williams, C. N., Rignot, E., An, L., Arndt, J. E., Bamber, J. L., Catania, G., Chauché, N., Dowdeswell, J. A., Dorschel, B., Fenty, I., Hogan, K., Howat, I., Hubbard, A., Jakobsson, M., Jordan, T. M., Kjeldsen, K. K., Millan, R., Mayer, L., Mouginot, J., Noël, B. P., O'Cofaigh, C., Palmer, S., Rysgaard, S., Seroussi, H., Siegert, M. J., Slabon, P., Straneo, F., van den Broeke, M. R., Weinrebe, W., Wood, M., and Zinglersen, K. B. (2017). BedMachine v3: Complete Bed Topography and Ocean Bathymetry Mapping of Greenland From Multibeam Echo Sounding Combined With Mass Conservation. *Geophysical Research Letters*.

Mouginot, J., Rignot, E., Scheuchl, B., and Millan, R. (2017). Comprehensive annual ice sheet velocity mapping using Landsat-8, Sentinel-1, and RADARSAT-2 data. *Remote Sensing*.

Neiswanger, W., Wang, C., and Xing, E. (2013). Asymptotically Exact, Embarrassingly Parallel MCMC. *Proceeding UAI'14 Proceedings of the Thirtieth Conference on Uncertainty in Artificial Intelligence*, (1):1–16.

Pattyn, F. (2003). A new three-dimensional higher-order thermomechanical ice sheet model: Basic sensitivity, ice stream development, and ice flow across subglacial lakes. *Journal of Geophysical Research*.

Pollard, D., Chang, W., Haran, M., Applegate, P., and DeConto, R. (2016). Large ensemble modeling of the last deglacial retreat of the West Antarctic Ice Sheet: Comparison of simple and advanced statistical techniques. *Geoscientific Model Development*.

Polyak, L., Alley, R. B., Andrews, J. T., Brigham-Grette, J., Cronin, T. M., Darby, D. A., Dyke, A. S., Fitzpatrick, J. J., Funder, S., Holland, M., Jennings, A. E., Miller,

G. H., O'Regan, M., Savelle, J., Serreze, M., St. John, K., White, J. W., and Wolff, E. (2010). History of sea ice in the Arctic. *Quaternary Science Reviews*.

Rasmussen, C. E. (2004). Gaussian Processes in machine learning. *Lecture Notes in Computer Science (including subseries Lecture Notes in Artificial Intelligence and Lecture Notes in Bioinformatics)*.

Reeh, N. (1991). Parameterization of Melt Rate and Surface Temperature on the Greenland lce Sheet. *Polarforschung*.

Ritz, C., Rommelaere, V., and Dumas, C. (2001). Modeling the evolution of Antarctic ice sheet over the last 420,000 years: Implications for altitude changes in the Vostok region. *Journal of Geophysical Research Atmospheres*.

Sarkka, S. (2013). Bayesian Filtering and Smoothing. *Cambridge University Press*.

Sarkkä, S., Hartikainen, J., Svensson, L., and Sandblom, F. (2016). On the relation between Gaussian process quadratures and sigma-point methods. In *Journal of Advances in Information Fusion*.

Singarayer, J. S., Bamber, J. L., and Valdes, P. J. (2006). Twenty-first-century climate impacts from a declining Arctic sea ice cover. *Journal of Climate*.

Tarasov, L., Dyke, A. S., Neal, R. M., and Peltier, W. R. (2012). A data-calibrated distribution of deglacial chronologies for the North American ice complex from glaciological modeling. *Earth and Planetary Science Letters*.

Tarasov, L. and Peltier, W. R. (2002). Greenland glacial history and local geodynamic consequences. *Geophysical Journal International*.

Thomas, E. K., Briner, J. P., Ryan-Henry, J. J., and Huang, Y. (2016). A major increase in winter snowfall during the middle Holocene on western Greenland caused by reduced sea ice in Baffin Bay and the Labrador Sea. *Geophysical Research Letters*.

Van Tatenhove, F. G., Van Der Meer, J. J., and Koster, E. A. (1996). Implications for deglaciation chronology from new AMS age determinations in central West Greenland. *Quaternary Research*.

Wright, P. J., Harper, J. T., Humphrey, N. F., and Meierbachtol, T. W. (2016). Measured basal water pressure variability of the western Greenland Ice Sheet: Implications for hydraulic potential. *Journal of Geophysical Research: Earth Surface*.

Young, N. E., Briner, J. P., Miller, G. H., Crump, S. E., Lesnek, A. J., and Thomas, E. K. (2019, In Review). Arctic deglaciation interrupted by abrupt coolings. *Science Advances*.

Appendices

Appendix A

SHMIP : Subglacial Hydrology Intercomparison Project

A.1 Overview

I participated in the subglacial hydrology intercomparison project using a linked cavity only version of the model outlined in Chapter 1, prior to implementing channelization. SHMIP was an excellent opportunity to verify and compare my subglacial hydroloygy model to other similar models. It later allowed me to test my implementation of GlaDS (Werder et al., 2013) by directly comparing my output to an existing implementation. This chapter was previously published in the Journal of Glaciology.

A.2 Authors

B. de Fleurian, M. A. Werder, , S. Beyer, D. J. Brinkerhoff, I. De-laney, C. F. Dow, **J. Downs**, O. Gagliardini, M. J. Hoffman, R. LeB Hooke, J. Seguinot, and A. Sommers

Abstract

Subglacial hydrology plays a key role in many glaciological processes, including ice dynamics via the modulation of basal sliding. Owing to the lack of an overarching theory, however, a variety of model approximations exist to represent the different characteristics of the subglacial drainage system. The Subglacial Hydrology Model Intercomparison Project (SHMIP) provides a set of synthetic experiments to compare existing and future models. We present results of these experiments from 13 participating models with a focus on effective pressure and discharge. The results show that for many applications (e.g. steady states and annual variations, or low input scenarios) a simple model, such as an inefficient-system-only model, a flowline or lumped model, or a porous-layer model provides results comparable to those of more complex models. However, when studying short term (e.g. diurnal) variations of the water pressure, the use of a two-dimensional model incorporating physical representations of both efficient and inefficient drainage systems yields results that are significantly different from those of simpler models and should be preferentially applied. The results also emphasise the role of water storage in the response of water pressure to transient recharge. Finally, we find that the localisation of moulins has a limited impact except in regions of very sparse moulin density.

A.3 Introduction

Subglacial water flow has long been the subject of glaciological studies (see Clarke, 1987, for a historical overview). Early quantitative treatments of subglacial drainage were motivated by a diverse range of problems: Weertman (1962) considered how a water layer at the glacier base impacts sliding, Röthlisberger (1972) developed his theory of channelised flow (through R channels) in connection with hydro-power generation related work, and Nye (1976) extended R channel theory with time-dependence to investigate glacier lake outburst floods. Recent developments in subglacial drainage theory have

been driven largely by the motivation to better understand, represent, and model glacier sliding, outburst floods and subglacial sediment dynamics in models.

It is indeed this link to ice dynamics that spurred the most recent, ongoing burst of subglacial drainage model development. As of yet, we do not fully understand the impact on ice dynamics of increased surface melt in a warming climate (e.g. Vaughan et al., 2013). For glaciers and land-terminating portions of the ice sheets, an acceleration in ice flow may lead to increasingly negative mass balance by moving ice to lower, warmer, elevations (Ridley et al., 2010). In temperate glaciers, a large fraction of mean ice velocity is due to slip of the glacier over its bed (e.g. Morlighem et al., 2013; Cuffey and Paterson, 2010; Engelhardt and Kamb, 1998). This basal slip is a combination of both sliding of the glacier ice over its bed and deformation of any water saturated till layer underlying the ice (Cuffey and Paterson, 2010). Both components of slip are primarily driven by the presence of water at the base of the glacier, in particular by its pressure (e.g. van de Wal et al., 2008; Iken et al., 1993; Iken and Bindschadler, 1986). Therefore, to assess the impact of increased surface melt on ice dynamics, we need to determine the response of the subglacial system to enhanced water input; current theories and models suggest that water pressure, and hence ice flow speed, could either increase or decrease, depending on the nature of the subglacial drainage (e.g. Joughin et al., 2018; Tedstone et al., 2015; Doyle et al., 2014; Sole et al., 2013; Shannon et al., 2013).

The scarcity of data and complexity of the subglacial system makes it difficult to pinpoint the water-induced processes acting at the base of glaciers. Thus, numerous theoretical models have been developed since the 1960s to mimic the flow of water at the beds of the glaciers (e.g. Creyts and Schoof, 2009; Kamb, 1987; Walder, 1986; Nye, 1973; Röthlisberger, 1972; Weertman, 1962). These models have been motivated by specific needs, preferences, and practical considerations, leading to a plethora of models. The different approaches used make it difficult to compare the diverse theories that they implement. For example, over the last couple of decades, a number of subglacial

hydrology models have been developed that compute basal water pressure directly from meltwater input (e.g. de Fleurian et al., 2014; Werder et al., 2013; Flowers et al., 2004), and a comprehensive overview is given in Flowers (2015) . An alternative approach has been to use a pressure definition as a closing equation for the subglacial hydrology model (e.g. Kavanagh and Tarasov, 2017; Bueler and van Pelt, 2015).

This intercomparison project sets out to alleviate the problem of multiple theoretical approaches to subglacial hydrology by establishing a set of synthetic simulation suites and comparing the results of the participating models running those simulations. This should help potential model users make a more informed decision as to which model to choose for a specific application. Likewise for model developers, this may assist in assessing where further model developments are needed and provides a set of reference models against which to compare future ones.

The aim of this intercomparison is different from that of ice-sheet model intercomparison projects (Pattyn et al., 2013, 2012, 2008; Payne et al., 2000; Huybrechts et al., 1996). In the latter case, the physics of ice flow are reasonably well established , although boundary conditions remain less clear and are usually specified as parts of the setup. For subglacial hydrology, however, a complete and "true" theory is lacking. In other cases, such as the ice-thickness estimation intercomparison ITMIX (Farinotti et al., 2017), a set of measurements is available which allows the assessment of the most appropriate model to apply. Unfortunately, observations of subglacial drainage are sparse, difficult to interpret (e.g. borehole measurements, Rada and Schoof (2018)) and unlikely to fully constrain all the parameters of a subglacial drainage model (e.g. Brinkerhoff et al., 2016). Furthermore, to date, applications of subglacial drainage models to real topographies and forcings are few and often hampered by modelling difficulties. Recognising these limitations and following the line of preceding intercomparison exercises, we opted for synthetic test cases which were better able to detect differences in physical or numerical approaches through qualitative comparisons.

Note that this intercomparison does not attempt to verify or validate the results provided by the participating models. Instead, SHMIP aims to provide a set of benchmark experiments tailored to compare existing and future subglacial hydrologic model in spite of their varied implementations. This intercomparison will also indicate which models will likely be appropriate for certain applications in subglacial hydrology. All results of this SHMIP exercise are openly accessibly at de Fleurian et al. (2018).

We first give a brief overview of subglacial drainage modelling and describe the physics implemented by the participating models. We then describe the approach taken by SHMIP and the different suites of experiments, before presenting results from the 13 models. Finally, we provide a synthesis of model results, and discuss strengths and potential shortcomings based on these results.

A.4 The wide variety of subglacial hydrology models

By design, this intercomparison exercise allowed participation of any model that calculates effective pressure (defined as ice overburden pressure minus subglacial water pressure).The project thus attracted a wide range of models: from a zero dimensional lumped element model to models simulating the entire two dimensional glacier bed. Models ranged from ones developed in the 1980s to others under current development and from models simulating one component of the system, for instance R channels, to models coupling several components. Table A.1 gives an overview of the participating models.

The components of the drainage system are commonly classified into two types: inefficient (slow) drainage, and efficient (fast) drainage, with the former usually represented as a distributed system and the latter as a channelised system (e.g. Flowers, 2015). This difference is a consequence of how the steady-state of each system transforms under increasing discharge: in an inefficient system pressure increases, because steeper pressure

Table A.1: Summary of the participating models. The model label is defined as the two initials of the experimenter; if the used model was published/written by someone else, then one initial of the first author is appended (e.g. *cdf*); models implemented by the experimenter from a published model are cited as "from: original publication"; two different models of the same experimenter are distinguished by a subscript number; two submissions of the same model using different parameters are distinguished by a prime. "Suites" lists the Suites for which model results were submitted. "Dim." gives the number of spatial dimensions of the model, which is used in the text to differentiate between them, i.e. 0D, 1D or 2D models. "Model Type" is a brief description of the type of model, which is used throughout the text; these are defined within the section "Subglacial hydrology modelling". "Parameters different from Table A.3" shows which parameters have been changed from the base-case Run, please refer to the supplementary for parameters of the models requiring tuning. "PDMP" states if the model introduces a pressure dependence to the melting point

Label	Experimenter and Citation	Suites	Dim.	Model type	Params different from Table A.3	PDMP
db	D. Brinkerhoff Brinkerhoff et al. (2016)	A,D–F	0D	conduit	$e_v = 10^{-3}$ (A,D) $e_v = 10^{-2}$ (E–F)	No
id	I. Delaney from: Kessler and Anderson (2004)	A–C, E,F	1D	conduit	$c_t = 0$	No
rh	R. LeB Hooke from: Röthlisberger (1972)	A,E	1D	one-channel (steady state only)	None	No
cdf	C. Dow Pimentel and Flowers (2010)	A	1D	macroporous-sheet /one-channel	see supplementary N tuned on A5	Yes
jd	J. Downs from: Hewitt (2011)	A–E	2D	cavity-sheet	$k_s = 10^{-2}$ (A6,B,C)	No
jsb	J. Seguinot Bueler and van Pelt (2015)	A–F	2D	cavity-sheet	$e_v = 10^{-3}$ (A–D) $e_v = 10^{-2}$ (E–F)	No
as	A. Sommers Sommers et al. (2018)	A–C, E,F	2D	cavity-sheet (with melt opening)	see supplementary N tuned on A3	Yes
sb	S. Beyer Beyer et al. (2017)	A–D	2D	(one) porous-layer	see supplementary N tuned on A3 and A5	No
bf	B. de Fleurian de Fleurian et al. (2016)	A–F	2D	(dual) porous-layer	see supplementary N tuned on A3 and A5	No
mh_1	M.J. Hoffman Hoffman and Price (2014)	A	2D	cavity-sheet /one-channel	None	No
mh_2	M.J. Hoffman Hoffman et al. (2018b)	A-D	2D	cavity-sheet /channels	$e_v = 10^{-3}$ (A–D)	Yes
og	O. Gagliardini Gagliardini and Werder (2018)	A–F	2D	cavity-sheet /channels	None	Yes
og'	O. Gagliardini Gagliardini and Werder (2018)	E,F	2D	cavity-sheet /channels	$c_t = 0$	No
mw	M.A. Werder Werder et al. (2013)	A–F	2D	cavity-sheet /channels	None base-case	Yes
mw'	M.A. Werder Werder et al. (2013)	C,D	2D	cavity-sheet /channels	$e_v = 10^{-4}$	Yes

gradients are required to conduct the increased discharge; conversely, in an efficient system pressure decreases, as the system's capacity increases sufficiently to allow operation at lower gradients.

In many of the participating models the inefficient component of the drainage system is based, at least partially, on a linked cavity drainage system using, either discrete elements (Kessler and Anderson, 2004) or a 2D sheet (Hewitt, 2011). The efficient component, if it is included, is usually represented by Röthlisberger channels (R channels) following Röthlisberger (1972). The *cdf* model uses a different type of water sheet (or inefficient system) based on Flowers et al. (2004). Two models (*bf* and *sb*) pursue a different strategy modelling the drainage as a porous aquifer in order to approximate discharge through both the inefficient and and efficient system. In the following section, the different types of drainage systems are briefly described. For a more in-depth comparison of subglacial drainage models, refer to the excellent review paper by Flowers (2015).

A.4.1 Subglacial hydrology modelling

Common to all participating models is the use of a conservation of water equation, which takes the form :

$$\frac{\partial h}{\partial t} + \nabla \cdot \mathbf{q} = m, \tag{A.1}$$

where h is the local size of the water body (height, area or volume, depending on the formulation), q is the water flux, and m is a source term (accounting for meltwater input from the surface via the englacial system as well as water produced by geothermal flux, by frictional heat from sliding, and by heat produced by dissipation in the subglacial flow). The second common ingredient is the use of a "water flow law" relating q with hydraulic potential gradient $\nabla\phi$ using a linear (Darcy flow) or nonlinear relation (Darcy-Weisbach

or Manning)

$$\mathbf{q} \propto \nabla\phi \quad \text{or} \quad \mathbf{q} \propto \sqrt{\nabla\phi}, \tag{A.2}$$

where the hydraulic potential $\phi = p_w + \rho_w g z$ is the sum of water pressure p_w and elevation potential (with water density ρ_w, acceleration due to gravity g and elevation z). The factor of proportionality may depend on other state variables, in particular h. Both these equations can be applied in 2D (a sheet), in 1D (a channel or width integrated water sheet), or in 0D (integrated over the whole domain).

However, these are only two equations for three unknowns q, ϕ, and h, so a third equation is needed to close the mathematical description of the subglacial drainage system. Typically, this equation describes the size of the drainage space. The different participating models implement this third equation in various ways, discussed in the following subsections. Furthermore, some models couple two drainage types together.

A.4.2 Sheet drainage

Over the years several formulations of water draining through a distributed system, often called a sheet drainage system, have been proposed (e.g. Creyts and Schoof, 2009; Kamb, 1987; Walder, 1986; Weertman, 1962). The participating models use two types of sheet-like drainage. The first, proposed by Flowers and Clarke (2002), is an empirical relation between water sheet thickness h and water pressure p_w based on data from Trapridge Glacier (Canada)

$$p_w = p_i \left(\frac{h}{h_c}\right)^{\frac{7}{2}}, \tag{A.3}$$

where p_i is ice overburden pressure and h_c is a critical sheet thickness. A model implementing this type of sheet drainage system will be referred to as a *macroporous-sheet model* (Table A.1).

The second formulation used by some of the participating models is based on a linked cavity drainage system (Kamb, 1987; Walder, 1986). In a 1D setting, this formulation

was advanced by Kessler and Anderson (2004) and Schoof (2010). Hewitt (2011) then generalised it to 2D by using a cavity height averaged over a suitably large patch of the glacier bed. The formula takes the form of a rate equation for h (cavity cross sectional area in 0D and 1D or average sheet height in 1D and 2D) that, when saturation is assumed, reads:

$$\frac{\partial h}{\partial t} = v_o - v_c, \tag{A.4}$$

where v_o is an opening rate, typically dependent on the sliding rate and bed roughness, and v_c is a closure rate due to ice creep. One possible form is

$$v_o = h_r u_b \quad \text{and} \quad v_c = \frac{2A}{n^n} h N^n, \tag{A.5}$$

where h_r is the bed roughness height, u_b is the ice sliding speed, A is the ice rate factor, n is Glen's exponent, and $N = p_i - p_w$ is the effective pressure. A model implementing this type of sheet drainage system will be referred to as a *cavity-sheet model* (Table A.1).

Note that in most models the opening term, v_o, does not contain the energy dissipation term (c.f. next section) which was in the original description (Kamb, 1987; Walder, 1986), as its implementation is not trivial (Dow et al., 2018) and it can lead to mathematical issues such as runaway growth of drainage space (Schoof et al., 2012). As an exception, model *as* does include opening by melt from dissipation, in conjunction with a different approach to the momentum equation (eq. A.2) (Sommers et al., 2018). For a more detailed overview of sheet-like drainage consult the excellent overview given in Bueler and van Pelt (2015).

A.4.3 Channelised drainage

The classic theory of channelised subglacial drainage, through R channels, was developed by Röthlisberger (1972) and Shreve (1972). Further work extended the theory to include time dependence and also water temperature as a free variable (Spring and

Hutter, 1982; Nye, 1976), and to enable the use of broad low conduits, rather than semi-circular ones (Hooke et al., 1990). Whereas other theories of channelised drainage exist, such as canals (Walder and Fowler, 1994) (although these can also be considered as a type of distributed system), all of the participating models implementing channelised drainage use R channels. Furthermore, none of the participating models include water temperature as a state variable and instead assume that water temperature is always either at the pressure melting point or at 0°C. The equation describing the channel cross-sectional area S is similar to the cavity-sheet equation

$$\frac{\partial S}{\partial t} = V_o - V_c. \tag{A.6}$$

The closure V_c is again by ice creep and is identical to eq. (A.5) (replacing h by S). Conversely, channel opening is due to ice melt at the channel walls

$$V_o = \frac{-Q\,\phi' + c_t c_w \rho_w\, Q\, p'_w}{\rho_i L}, \tag{A.7}$$

where the prime $'$ is short for the spatial derivative $\frac{\partial}{\partial s}$ along the channel, c_t is the Clapeyron slope, c_w the heat capacity of water, ρ_i the density of ice, and L the latent heat of fusion. The first term in the numerator is the energy dissipation in the flow (i.e. mechanical energy converted to thermal energy by the flow). The second term takes into account the changes in sensible heat due to pressure melting point variations, with the Röthlisberger constant $c_t c_w \rho_w \approx 0.3$. This second term can be neglected if the water is assumed to be always at 0°C. A model implementing this type of R channel drainage will be referred to as a *one-channel model*, if it involves only one channel, or a *channels model*, if it involves a network of channels (Table A.1).

The equations of a single cavity (eq. (A.4)) and an R channel (eq. (A.6)) can be combined into one

$$\frac{\partial S}{\partial t} = v_o + V_o - V_c \tag{A.8}$$

(Kessler and Anderson, 2004), sometimes termed a conduit (Schoof, 2010), thus giving a drainage element that opens both by sliding and by melting. When opening by sliding dominates, the system behaves like a cavity; otherwise it is like an R channel. A model implementing this type of drainage system will be referred to as a *conduit model* (Table A.1).

Equations (A.1), (A.2), and (A.6) describe a single R channel. However, the subglacial system is thought to consist of a network of these channels. Relatively recent advances (Hewitt, 2013; Werder et al., 2013; Schoof, 2010) have made the simulation of such a network of R channels possible.

A.4.4 Porous layer drainage

The approach to modelling a network of R channels described above has several drawbacks, such as having to resolve each channel with the mesh and having no obvious continuum limit. This, among other things, inspired the development of porous layer drainage models. Such models do not try to simulate the drainage system as described by the theory presented above but instead use one or several porous layers as being equivalent to different types of subglacial drainage. Porous layers are usually considered an inefficient drainage system (Shoemaker, 1986), but with proper parameter choice these layers can be configured to be as transmissive as highly efficient systems (Teutsch and Sauter, 1991). These models also rely on mass-conservation (eq. (A.1)) and Darcy flow (eq. (A.2)). To close the model, either a fixed layer thickness h is assumed, or the layer evolves as a function of the pressure.

Two main approaches are used to simulate systems with different efficiencies within this porous layer framework. In the first, several layers with different conductivities are used. In the second a single layer is used and the conductivity (the constant of proportionality in eq. (A.2)) is allowed to evolve. The porous layer models included here

assume a non-zero compressibility (β), which adds a significant amount of storage S_s:

$$S_s = \rho_w g \omega h \beta \tag{A.9}$$

where ω is the porosity of the layer. A model implementing this type of drainage system will be referred to as a *porous-layer model* (Table A.1).

A.4.5 Additional drainage elements

Additional drainage elements, such as drainage through till (e.g. Flowers and Clarke, 2002) are incorporated in some subglacial drainage models. In the participating models, the only additional process included is the variation of water storage as a function of water pressure. The storage in the englacial system is considered to be well connected to the subglacial system (i.e. the englacial water table height corresponds to the subglacial water head). This necessitates a modification of the conservation equation (eq. (A.1))

$$\frac{\partial h}{\partial t} + \frac{\partial h_e}{\partial t} + \nabla \cdot q = m, \tag{A.10}$$

to include the thickness of the effective storage component h_e, which is given in terms of the water pressure $h_e = e_v \frac{p_w}{\rho_w g}$ in which e_v is the englacial void fraction.

A.4.6 Coupling of components

Subglacial drainage is thought to occur through different types of drainage systems, co-evolving in space and time and exchanging water (e.g. Iken and Truffer, 1997). To approximate this complex behaviour, many models couple multiple system components together. One example is the conduit mentioned above (eq. (A.8)), combining an R channel and a cavity. Table A.1 gives an overview over the coupled systems of each model. Additional details on each model are given in the supplementary mate-

rials. A model implementing several types of drainage systems will be referred to as the combination of systems it implements e.g. *cavity-sheet/(one-)channel model* and *macroporous-sheet/one-channel model* (Table A.1).

A.5 Intercomparison design and setup

The present intercomparison project deviates from many previous ones involving other components of the ice dynamic system, as there is no established theory of subglacial drainage, nor are there any sufficiently dense datasets that would allow reasonably conclusive comparisons with reality. This scenario prevents both validation and verification of the models participating in the intercomparison (Oreskes et al., 1994). With these limitations in mind, we designed the intercomparison around six synthetic Suites of experiments (labelled from A to F) each consisting of a set of four to six numerical experiments, subsequently referred to as *Runs*. The setup and detailed instructions are available online[1] and the website contents are included in the supplementary material. The Suites are designed to allow a wide variety of models to take part in the intercomparison and to test a large range of scenarios. This design allowed the participation of 13 models that completed some or all of the experiments. The main requirement was that models should output the effective pressure, which is used as the main diagnostic variable throughout the intercomparison. This approach excludes models based on a routing-approach (e.g. Le Brocq et al., 2009) and the till-layer based models (e.g. Bougamont et al., 2014). These alternative models do not explicitly compute effective pressures but instead use a pressure field unrelated to the state of the drainage system.

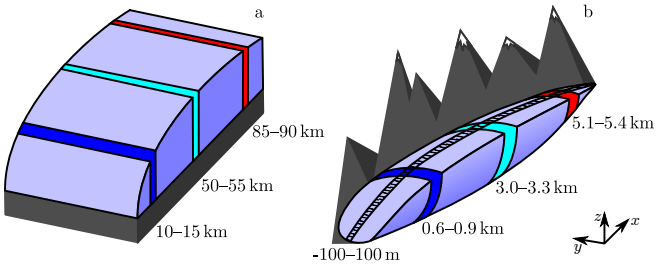

Figure A.1: Sketches of the topographies used, (a) 100 km long synthetic ice sheet margin with a maximum thickness of 1500 m, and (b) 6 km long synthetic valley glacier with a 600 m altitude difference between summit and terminus. The coloured and hatched bands are the regions used in presentation of the results.

Table A.2: List of symbols and fixed parameters used in the definition of the Suites of experiments.

Name	Value and units	Symbol
Bed elevation	m	z_b
Surface elevation	m	z_s
Glacier outline	m	y_o
Time coordinate	s	t
Spatial coordinates	m	x, y
Lapse rate	$-0.0075\,\mathrm{Km}^{-1}$	$\frac{\mathrm{d}T}{\mathrm{d}z}$
Day	$24 \times 3600\,\mathrm{s}$	s_d
Year	$365 \times s_d\,\mathrm{s}$	s_y
Degree day factor	$0.01/s_d\,\mathrm{mK}^{-1}\mathrm{s}^{-1}$	DDF

A.5.1 Topographies

The intercomparison uses two different synthetic glacier topographies (Fig. A.1). The first (Fig. A.1a), used for Suites A to D is a synthetic representation of a land-terminating ice sheet margin as seen, for instance, in Werder et al. (2013). The ice-sheet domain is 100 km long (in the x direction) and 20 km wide (in the y direction), with a flat bed, parabolic ice surface, and a maximum ice thickness of 1500 m:

$$\begin{aligned} z_s(x,y) &= 6\,(\sqrt{x+5000} - \sqrt{5000}) + 1, \\ z_b(x,y) &= 0, \end{aligned} \tag{A.11}$$

[1] `https://shmip.bitbucket.io/`

where z_s and z_b are the surface and bed elevation in metres, and x and y are the horizontal spatial coordinates in metres. To avoid numerical issues, the minimum ice thickness is 1 m.

The second topography (Fig. A.1b), used for the Suites E and F, is a synthetic valley-glacier geometry inspired by Bench Glacier, Alaska, USA (e.g. Fudge et al., 2008). The glacier is 6 km long and 1 km wide, with a difference in altitude between the terminus and the head of 600 m. Its shape is given by the following two equations:

$$\begin{aligned} z_s(x,y) &= 100\,\sqrt[4]{x+200} + \frac{x}{60} - \sqrt[4]{2\times 10^{10}} + 1, \\ z_b(x,y,\gamma) &= f(x,\gamma) + g(y)\; h(x,\gamma), \end{aligned} \tag{A.12}$$

in which γ is a parameter controlling the bed overdeepening, and f, g and h are helper functions defined as follows:

$$\begin{aligned} f(x,\gamma) &= \frac{z_s(6000,0) - 6000\,\gamma}{6000^2}x^2 + \gamma\, x, \\ g(y) &= 0.5\times 10^{-6}\;|y|^3, \\ h(x,\gamma) &= \frac{\left(-\frac{4.5\,x}{6000}+5\right)\;\Big(z_s(x,0) - f(x,\gamma)\Big)}{z_s(x,0) - f(x,\gamma_b) + 10^{-16}}, \end{aligned} \tag{A.13}$$

where $\gamma_b = 0.05$ is the parameter that is used as a reference γ and which gives the closest matching bed elevation to that of Bench Glacier. By design, the glacier boundary is the same for all γ and its half-width is given by

$$y_o(x) = g^{-1}\left(\frac{z_b(x,0) - f(x,\gamma_b)}{h(x,\gamma_b) + 10^{-16}}\right). \tag{A.14}$$

Table A.3: Physical parameters appearing in the drainage model description with the values to be used, as applicable, for the simulations (eq. (A.1)– (A.10), upper part). Additional reference parameters from GlaDS-model (lower part).

Name	Value	Symbol
Water density	$1000\,\mathrm{kg\,m^{-3}}$	ρ_w
Glacier Density (ice+firn)	$910\,\mathrm{kg\,m^{-3}}$	ρ_i
Acceleration of gravity	$9.8\,\mathrm{m\,s^{-2}}$	g
Latent heat of fusion	$334\,\mathrm{kJ\,kg^{-1}}$	L
Specific heat capacity water	$4220\,\mathrm{J\,kg^{-1}K^{-1}}$	c_w
Clausius-Clapeyron constant	$7.5\times10^{-8}\,\mathrm{K\,Pa^{-1}}$	c_t
Glen's n	3	n
Ice flow constant[a]	$3.375\times10^{-24}\,\mathrm{Pa^{-3}\,s^{-1}}$	A
Ice sliding speed	$1\times10^{-6}\,\mathrm{ms^{-1}}$	u_b
Bedrock bumps height	$0.1\,\mathrm{m}$	h_r
Englacial void fraction	0 (A–D) or 10^{-3} (E,F)	e_v
Bedrock bump wave-length	$2\,\mathrm{m}$	l_r
Turbulent flow exponent α	5/4	α
Turbulent flow exponent β	3/2	β
Sheet "conductivity"	$0.005\,\mathrm{m^{7/4}\,kg^{-1/2}}$	k_s
Sheet-width contributing to R channel melt	2 m	l_c
R channel "conductivity"[b]	$0.1\,\mathrm{m^{3/2}\,kg^{-1/2}}$	k_c

[a]Where the ice flow constant is for a closure relation as described in eq. (A.5)
[b]equivalent Darcy-Weisbach $f = 0.195$ for semi-circular channel

A.5.2 Boundary conditions

For the two geometries, the boundary conditions are prescribed to give a realistic distribution of water pressure. The most important boundary is the margin of the ice sheet ($x = 0\,\mathrm{km}$) or terminus of the glacier ($x = y = 0\,\mathrm{km}$) where the water pressure is required to be null. The flux at this boundary is then free to evolve. All the other boundaries are treated as zero-flux boundaries.

A.5.3 Parameters and optional tuning

The two topographies are complemented by a set of physical parameters (see Table A.3), which are used in the cavity-sheet/channels drainage formulations (eq. (A.1)–(A.10)).

Experimenters using models that implement this cavity-sheet/channels formulation (or a very similar one) were instructed to use the provided parameters in their model Runs. Note that the englacial void fraction e_v is different for Suites A–D and Suites E–F.

However, a wider range of physics is incorporated in the participating subglacial hydrology models (and presumably future models that may use this intercomparison as a test setup), and this requires additional and/or different parameters. This further hampers an intercomparison of models based on different physics. To circumvent this difficulty, models whose parameters are not captured in Table A.3 are tuned to the width-averaged effective pressure output of two reference Runs of a model employing the cavity-sheet/channels formulation (GlaDS model, *mw*, tuning instructions[2]). Optionally, modellers could also tune using the provided width-averaged sheet and channel discharge. The chosen reference Runs are two steady state Runs with low and high recharge (Runs 3 and 5 from Suite A, Figure A.2m) that correspond to a sheet-only state and to a channelised state of model *mw*, respectively. The models that used tuning are *cdf* (only A5), *jd* (only A5, for high discharge), *as* (only A3), *sb*, and *bf* (a red label in Figure A.2 indicates a tuned model, with the white outline showing the tuned Runs). Most tuned models only used the provided effective pressure but model *as* which was also roughly tuned to discharge. Note that the tuning was optional and that lack of tuning would not preclude participation. However, no model with parameters diverging from that of the reference model were submitted without tuning. Nevertheless, the prescribed tuning is unlikely to constrain all parameters of a subglacial drainage model, for instance any parameters reflecting transient behaviour will not be constrained. However, we feel that this tuning strategy presents a balance between making the model outputs comparable without requiring models employing other physics to over-fit and thus pushing them into a regime that is not representative for them. Finally, results that are different from the reference Run do not mean that the corresponding model is less correct, but merely

[2] `https://shmip.bitbucket.io/instructions.html\#sec-1-2`

Table A.4: List of variable parameters for each Suite of experiment Runs. See the description of each Suite for more information on the parameters.

Suite	Varying parameter	Run: 1	2	3	4	5	6
A	water input m ($\mathrm{m\,s^{-1}}$)	7.93×10^{-11}	1.59×10^{-9}	5.79×10^{-9}	2.5×10^{-8}	4.5×10^{-8}	5.79×10^{-7}
B	number of moulins	1	10	20	50	100	n/a
C	relative amplitude R_a	1/4	1/2	1	2	n/a	n/a
D	temperature offset ΔT ($^\circ C$)	-4	-2	0	2	4	n/a
E	bed parameter γ	0.05	0	-0.1	-0.5	-0.7	n/a
F	temperature offset ΔT ($^\circ C$)	-6	-3	0	3	6	n/a

different.

A.5.4 Suite A: steady state

The six Runs of Suite A are based on the ice-sheet topography (eq. (A.11) and Fig. A.1a) with a steady and spatially uniform water input. The primary objective of Suite A (beside providing a base-case for tuning) is to produce results for a simple steady-state in terms of effective pressure and discharge. The input increases by four orders of magnitude from a low value corresponding to basal melt production (Run A1, $m \simeq 2.5\,\mathrm{mm\,a^{-1}}$) to a high water input based on the peak water discharge driven by surface melt as observed in Greenland (Run A6, $m \simeq 50\,\mathrm{mm\,d^{-1}}$ (Smith et al., 2017), see Table A.4).

A.5.5 Suite B: localised input

The importance of input localisation is investigated in Suite B. To test this, the spatially uniform input that was used in Run A5 is instead fed into an increasing number of moulins (i.e. point inputs). The number of moulins increases from one (B1) to 100 (B5) between which the discharge is equally partitioned (see Table A.4). The location of the moulins is randomly generated for each Run and then used in all of the different models. Experimenters running 1D models were instructed to collapse the moulins onto a single

flowline. Additionally a distributed input, as in Run A1, is included to represent basal melt.

A.5.6 Suite C: diurnal cycle

The effect of short time scale dynamics, as represented by the diurnal melt cycle, on the response of the subglacial drainage system is targeted by Suite C. The starting point for the Runs of this Suite is the steady state achieved in Run B5 (steady input into 100 moulins). The different Runs are performed with diurnal melt cycles of increasing amplitude with recharge into each moulin given by

$$R(t, R_a) = \max\left(0,\, M_{in}\left[1 - R_a \sin\left(\frac{2\pi t}{s_d}\right)\right]\right), \tag{A.15}$$

where t is the time in seconds, s_d the number of seconds per day and $M_{in} = 0.9\,\mathrm{m^3 s^{-1}}$ the background moulin input from Run B5 (see Table A.4). The models were to be run until a periodic state was reached. The relative amplitude of the forcing R_a ranges from 0.25 for Run C1 to 2 for Run C4 (see Table A.4). For Run C4, the negative input values given by the high amplitude of the signal are cut off (see supporting Fig. S9) and this Run, therefore, has an overall higher water input than C1 to C3 ($\sim$20% of volume increase). As in B5, a uniform and constant background input equal to the recharge of A1 is applied.

A.5.7 Suite D: seasonal cycle

The long time scale (seasonal) evolution of the drainage system, is investigated in Suite D. It uses initial conditions from Run A1, which represent the water input during winter. From this starting point, a seasonal cycle is applied to the water input and the model is run until a periodic annual state is achieved. The forcing is computed from a simple

degree day model driven by a temperature parameterisation. The temperature at 0 m elevation is given by

$$T(t) = -16\cos\left(\frac{2\pi t}{s_y}\right) - 5 + \Delta T. \tag{A.16}$$

The Runs of this Suite are achieved by increasing the mean annual temperature, the value of ΔT, from -4°C to 4°C (see Table A.4).

The distributed recharge is then computed from the following degree day model formulation

$$R(z_s, t) = \max\left(0,\, DDF\,\left(T(t) + z_s\frac{\mathrm{d}T}{\mathrm{d}z}\right)\right), \tag{A.17}$$

where $\frac{\mathrm{d}T}{\mathrm{d}z} = -0.0075$ Km^{-1} is the lapse rate and $DDF = 0.01/86400\,\mathrm{m\,K^{-1}s^{-1}}$ is the degree day factor (Table A.2). As in Suites B and C, a uniform and constant basal melt input equal to that of A1 is applied in all Runs.

A.5.8 Suite E: overdeepening of valley topography

Suite E is designed to investigate the effect of bed slope on the models. The common base for this Suite is the synthetic valley topography (eq. (A.12) and Fig. A.1b). In the different Runs of this Suite the shape of the bed topography is altered to define a more or less pronounced overdeepening (Table A.4 and Fig. A.6k). The water input is constant and uniformly distributed at twice the rate of Run A6 ($m \simeq 100\,\mathrm{mm\,d^{-1}}$). Note that reference parameters for the valley Runs results in a non-zero storage (Table A.3).

A.5.9 Suite F: seasonal cycle on valley topography

Suite F runs a seasonal water forcing—mirroring Suite D—for the synthetic valley glacier using the baseline value of the topography parameter $\gamma = \gamma_b$. First the models are run to a steady state with water input as in A1. This steady state is then used as an initial condition for all of the Runs. Following this, a seasonal forcing as specified

with eqs. (A.16) and (A.17) is applied using temperature offsets between -6°C and 6°C (Table A.4).

A.6 Results

The objective of this study is to illuminate the differences between various subglacial hydrology formulations to show how these differences affect model results. Our evaluation focuses on effective pressure as that is the principal coupling to ice dynamics, which in turn is a primary motivation behind subglacial drainage studies. All of the submitted results are open source and can be accessed at de Fleurian et al. (2018) for further investigation. We condense the results into three types of figures: steady-state with distributed recharge (Suites A and E, Figs. A.2 and A.6), steady-state with moulin input (Suite B, Fig. A.3), and transient simulations (Suites C, D and F, Figs. A.4, A.5 and A.7). Figures A.3, A.4, A.5 and A.7 present only one or two Runs in detail on which we focus the discussion. However, the figures for the other Runs are provided in the supplementary material as well as numerous additional figures for each Run and model.

Steady-state Suites A and E (Figs. A.2 and A.6) are evaluated using the percentage of flux in the efficient system and the width-averaged effective pressure (N). The full width is used in Suite A and a band of 200 m width, indicated by the hatched band in Figure A.1b, is used in Suite E. The former is calculated, in most models, as the ratio of width-averaged channelised flux to total flux. This ratio is straightforward to compute for models that calculate the flux separately in the two systems, but for models relying on a single system to model both efficient and inefficient drainage another quantity is used as a proxy: for *sb*, the flux is considered to pass through the efficient drainage system when the transmitivity is above $0.1\,\mathrm{m^2 s^{-1}}$; for *as*, *db*, and *id* the ratio of melt opening rate to total opening rate is used; for *jd*, *rh* and *jsb* no proxy-quantity was

calculated as they are single system models. In our analysis, we classify the drainage system as efficient if more than 10% of the discharge is through the efficient system; at this stage the effective pressure begins to be characteristic of an efficient system with increase in flux leading to increase in effective pressure.

We evaluate Suite B, also at steady-state, by looking at the change between Runs B1 and B4, which use localised moulin input, as compared to Run A5, which uses the same total input but distributed uniformly (Fig. A.3).

Suites C, D and F are transient models. Their width-averaged effective pressures are evaluated in three bands as displayed in Figure A.1 Their width-integrated discharge is evaluated in either the lowermost band (C) or all three bands (D,F) (Figs. A.4, A.5 and A.7). Additionally, the phase lag is calculated between the recharge forcing and effective pressure signal, as well as the effective pressure amplitude.

A.6.1 Suite A: steady state

The effective pressure distribution and the type of system (inefficient in blue or efficient in red) is presented in Figure A.2. Moving upglacier from the terminus, all model Runs—except the lumped model *db* and those with an effective pressure close to zero on the whole domain—show a steep increase of effective pressure over the initial 10 km. This pressure distribution is driven by the ice sheet geometry and the terminus boundary conditions. Farther upglacier, all of the model outputs follow the widely acknowledged rule that, in a steady-state, a higher discharge leads to decreasing N if the system is inefficient and to increasing N if the system is efficient. This can be observed in Figure A.2 both as the discharge increases with proximity to the terminus, and as the specified recharge increases (from A1 to A6).

The different treatments of the subglacial drainage system lead to some variations in the results. The 0D model *db* demonstrates channelisation in A5 but no corresponding increase in effective pressure either in A5 or the higher discharge A6. The channel and

conduit models (rh and id, respectively) show a bias towards a more efficient drainage system, which is expected from their formulation. The effect of the single cavity of the conduit model id is clearly seen in A1 (and the upstream region in A2 and A3) where the effective pressure increases with a decrease in discharge. The channel (rh) and conduit (id) models also produce higher N for Run A6 than the fully channelised cavity-sheet/channels models (mh_2, og and mw), because all water is conducted through a single R channel, whereas the cavity-sheet/channels models have several parallel R channels (see supporting Figs. S145, S156, S177).

The cavity-sheet models (jd, jsb, as, mw, mh_1, mh_2 and og) show a shallow effective pressure gradient between 10 and ∼70 km before it increases again near the upglacier domain boundary. Of those models, the ones using a cavity-sheet drainage system exclusively (jd and jsb), have lower effective pressure in the higher discharge Runs (A4-A6) compared to the models that also incorporate an efficient system. For the cavity-sheet model jd, the tuning to A5 does not yield significant improvement in the results of Run A6 (where the tuned values are used). The cavity-sheet model as produces effective pressure values positioned between those of the cavity-sheet and of the cavity-sheet/(one-)channel models, due to the inclusion of opening by melt across the entire domain, allowing efficient drainage to develop.

The models using tuning (cdf, jd, as, sb and bf) obtain a reasonable fit to their target input scenarios with a better fit for the higher input scenarios (when targeted). Using the tuned parameters, cdf and bf show effective pressures largely above that of the reference simulation mw for Runs A1 and A2 (or in the case of cdf, A3, as A1 and A2 did not converge in the cdf model), and show no shallow gradient region in the middle of the domain. Results from sb and cdf closely follow those of mw for Run A6 while bf did not converge for this Run. The porous-layer models sb and bf predict more channelisation for A4 than the reference results of mw. The different approaches to the porous approximation are particularly clear in this Suite where the single layer model

allowing variations in transmitivity (sb) closely follows the results of mw with slightly lower effective pressure. Compared to this, the fixed transmitivity of the inefficient layer in bf model yield unrealistically large effective pressure under low water input.

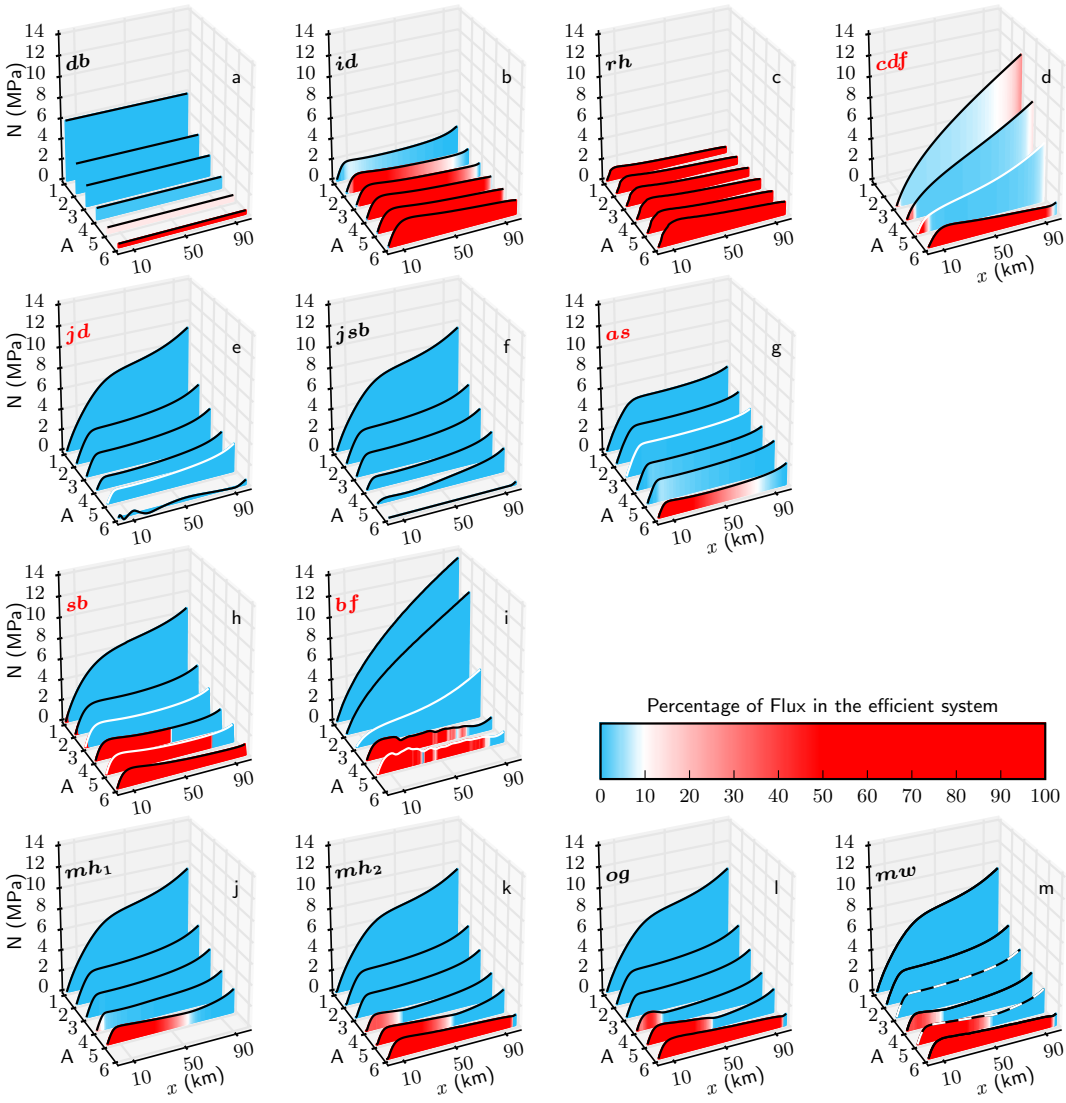

Figure A.2: Suite A results: mean value of the effective pressure (N) versus distance from the terminus (x) for all Runs (axis labelled A). Each submission is displayed in its own panel with the submission label printed. The results with the black and white dashed outline are the reference simulations used for tuning. Models that were tuned to any of the reference simulations have their submission name in red and the fitted Run(s) are highlighted with a white outline. The colours represent the level of channelisation of the drainage system. Here a shift from inefficient to efficient drainage system occurs when 10% of the total flux is drained by the efficient drainage system.

A.6.2 Suite B: steady state with moulin input

Suite B examines the impact of localised recharge on effective pressure distribution. This is achieved by recharging the system through an increasing number of moulins while keeping a constant overall input. We show results for Runs B1 and B4 (Fig. A.3), in which recharge is through 1 and 50 moulins, respectively (other Runs in supporting Figs. S1-5). Figure A.3 shows the difference in effective pressure between Run B1 and A5 in the left column, and that between Run B4 and A5 in the right column.

The results show two clearly different behaviours. In Runs B3 to B5, with 20, 50 and 100 moulins, respectively, the impact of the localised input on effective pressure is relatively small as can be seen in the example of Run B4 shown in Figure A.3j–r. All models that provided results for this Run show a similar response with the amplitude of the difference between A5 and B4 ranging from almost nothing for *id* to ± 0.5 MPa. In contrast, the lower moulin count Runs B1 and B2 (1 and 10, respectively), produce distinctive spatial variability in their outputs (see B1 in Fig. A.3a–i.). For those Runs, the largest difference from A5 is upstream of the highest moulin where the effective pressure increases, reaching values at least twice as large as that of A5 at the highest point of the domain. Downstream of the highest moulin, the pressure distributions are much closer to that of Run A5 with a maximum variation of $\sim$10% of the ice overburden pressure. We attribute this pattern to the limited discharge, provided only by basal melt, upstream of the highest moulin. In general, in models with only an inefficient system, effective pressure is lower than in A5 below the uppermost moulin (negative values). The other models have higher effective pressure. It is interesting to note that the effective pressure drops locally at moulin locations in all 2D models (Fig. A.3b–i and k–r); this appears as small spikes along the lower bound of the pressure envelope (see also supplementary material).

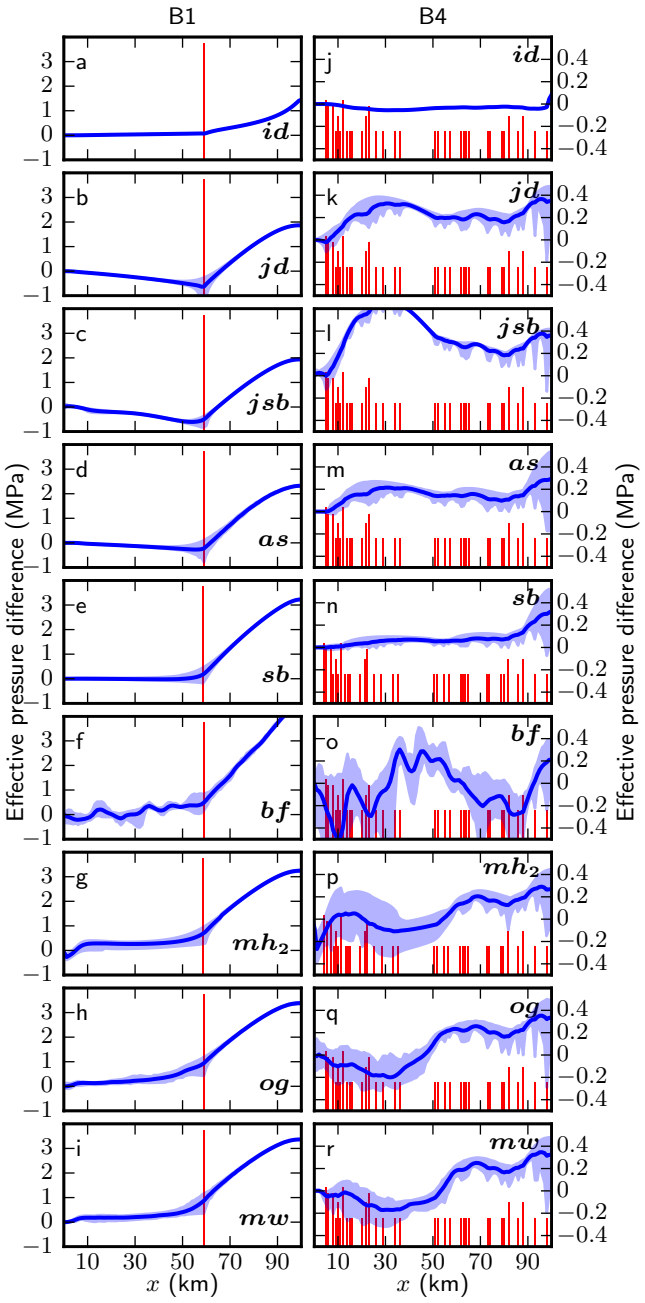

Figure A.3: Suite B results: the left column shows the difference in effective pressure between Run B1 and reference Run A5 (with same total recharge in both Runs). The right column shows the difference in effective pressure between Run B4 and A5. The differences are such that higher effective pressure in B yield positive values. The width-averaged difference is the solid blue line, and width-minimum and maximum difference are given by the light blue band. The red bars indicate moulin locations, their height scaled with the logarithm of input; the bars that are higher in Run B4 (right) are because multiple moulins are located at the same x-coordinate. Note that the scale of the effective pressure difference is different between the two columns.

A.6.3 Suite C: diurnal cycle

Suite C probes the time evolution of effective pressure and discharge in response to a diurnal melt-water forcing using the moulins of B5 as input locations (Fig. A.4). Our discussion focuses on Run C3 and the other Runs are plotted in supporting Figures S6-9.

The primary difference between the models is the magnitude of the simulated diurnal effective pressure variation (Fig. A.4b–k), which is chiefly dependent on the amount of available englacial and/or subglacial water storage. Participants running a model including a storage component were instructed to set it to zero. However, many models require some amount of storage for numerical reasons and therefore retained non-zero storage for this Suite. Models with no storage (*id*, *jd*, *as*, *og*, *mw*) show large effective pressure amplitude and minimal lag (1-2 h) between maximum recharge and minimum N (Fig. A.4A–J). This pressure amplitude increases with the forcing amplitude hence lowering the daily averaged effective pressure with respect to that of B5. Conversely, models including a storage component (*jsb*, *sb*, *bf*, mh_2, mw') have a very small effective pressure amplitude and the lag is ∼6 h. This leads to a daily mean value of the effective pressure that is close to the steady-state value of Run B5. The impact of available water storage amount is nicely illustrated by the two submissions of the same model *mw* and mw', the former using no storage, the latter using storage (Fig. A.4j,k). Note that the models *jsb* and mh_2 acquire their storage-like behaviour from solving a regularised pressure equation (Bueler and van Pelt, 2015) without actually storing water.

The same variations, or lack thereof, between storage and no-storage models also appear in the width-integrated discharge of the lower band (Fig. A.4l–u). The cavity-sheet/channels models with little storage (*og* and *mw*) show a larger amplitude in the efficient system discharge, because the recharge via moulins directly feeds that system. The cavity-sheet/(one-)channel models (mh_2, *og*, *mw* and mw') show a partitioning of the discharge with roughly 2/3 in the efficient and 1/3 in the inefficient system. In model *as*, most of the flux is through the inefficient system with a slight increase in efficient

drainage when the recharge is at its maximum. Conversely, the two porous-layer models conduct most or all of the discharge in the efficient system.

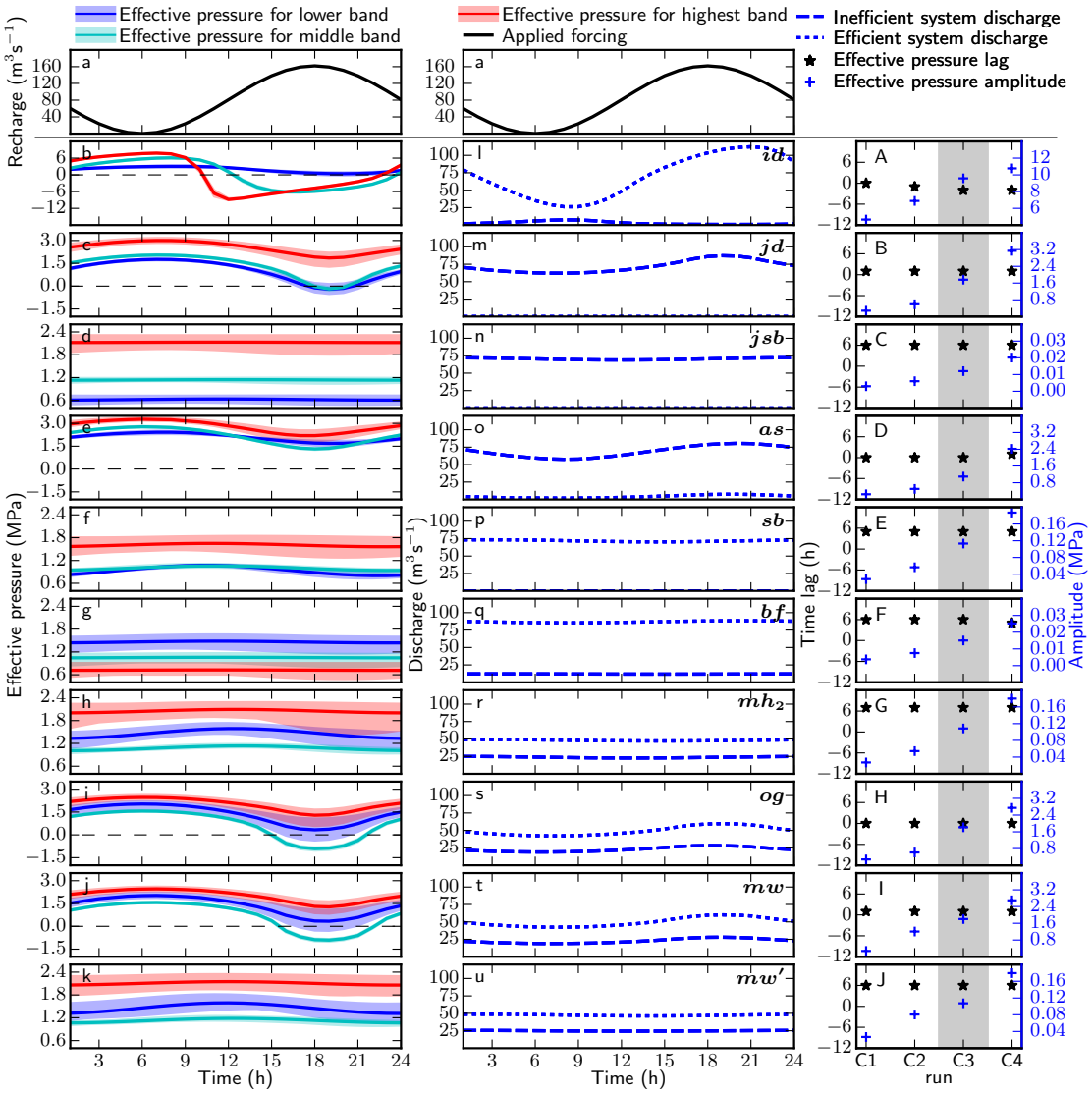

Figure A.4: Suite C results: left and centre columns show Run C3 with a panel for each submission, right column shows all Runs. The top row shows total recharge for the whole domain (a). Each row shows the results of one model (model label in the middle column). The left column (b to k) shows the evolution of the mean effective pressure in the three bands as defined in Figure A.1a. The coloured line shows the mean value and the shading represents the spread within the band. The dashed black line marks zero effective pressure. The middle column (l to u) shows the evolution of the discharge in the inefficient (dashed) and efficient (dotted) drainage system for the lower band. The right column (A to J) shows the time lag between maximum recharge and minimum effective pressure (black stars) and amplitude of the effective pressure variation (blue crosses) averaged over the entire domain for Runs C1 through C4. Note that the scale for amplitude of effective pressure variations varies between models. The greyed region in the right column identifies the Run plotted in the two left columns.

A.6.4 Suite D: seasonal cycle

Suite D investigates the influence of seasonal forcing on the subglacial drainage system. This Suite uses a distributed recharge with increasing amplitude of the seasonal recharge from D1 to D5. We focus the discussion on the Run D3 (Fig. A.5) which is presented similar to the results of Suite C. The other Runs of this Suite are plotted in supporting Figures S10-14.

During winter, the effective pressure in all of the model Runs is ∼3 to 8 MPa with lower N in the lower bands (first column of Fig. A.5). This is in contrast to recorded winter pressures (e.g. van de Wal et al., 2015), which tend to show effective pressures close to zero.

When the recharge increases in spring, the effective pressure drops in all models reproducing the commonly known spring event (Röthlisberger and Lang, 1987), which propagates upstream and reaches the highest band (90 km from the front) by mid-summer. In some bands, the models that do not cap N at zero obtain negative effective pressures, in many instances persisting for several months, during this phase. For all of the models aside from the double porous-layer (bf), the amplitude of the effective pressure drop is similar over the whole domain, whereas the bf model shows a notably smaller amplitude in the highest band of the domain.

The different models recover from this spring event in different ways. The main difference is the ability of the two-components model to develop an efficient system, which is observed on the distribution of the discharge between the two systems (middle column Figure A.5). The cavity-sheet/(one-)channels models initially carry most of the discharge in the distributed system before transitioning—but only in the lower band—to channelised drainage. The mh_2 model shows a later transition than the other three cavity-sheet/channels models (og, mw, mw'). The cavity-sheet/one-channel model (mh_1) still discharges a sizeable amount of water through its inefficient system when the channel is active (see supporting Figure S11 to compare D2 Runs). For the double

porous-layer model (bf) and the single component models where a threshold is fixed to define efficient drainage (db and sb), the shift to efficient drainage occurs earlier in the season compared to the cavity-sheet/(one-)channels models. This shift is also more widespread, reaching as high as the middle band where the cavity-sheet/(one-)channels models show an efficient drainage only in the lower band. The cavity-sheet models show an asymmetric discharge with an increase that is slower than the recharge increase and a steeper discharge decrease at the end of the melt season.

The results of the higher storage Run mw' (compared to mw) indicate that higher storage leads to a lower effective pressure during winter and a delayed drop in the effective pressure in the highest band (red). Similar outputs occur with the porous layer models (sb and bf), but not with the models using storage as a means of stabilisation (jsb and mh_2).

The rightmost column of Figure A.5 shows the amplitude of the effective pressure variations and the time lag between the time of maximum recharge and minimum effective pressure for all D Runs. All models show similar trends for those two values: the effective pressure minimum occurs earlier as the water recharge increases (from D1 to D5). For most models, the effective pressure minimum follows peak recharge with lower recharge intensities, and precedes peak recharge with higher recharge intensities. The amplitude of the effective pressure variation also increases as discharge increases, except in the 0D model (db). The latter is because the effective pressure in model db is restricted to positive values, thus limiting the amplitude of the response already for Run D1.

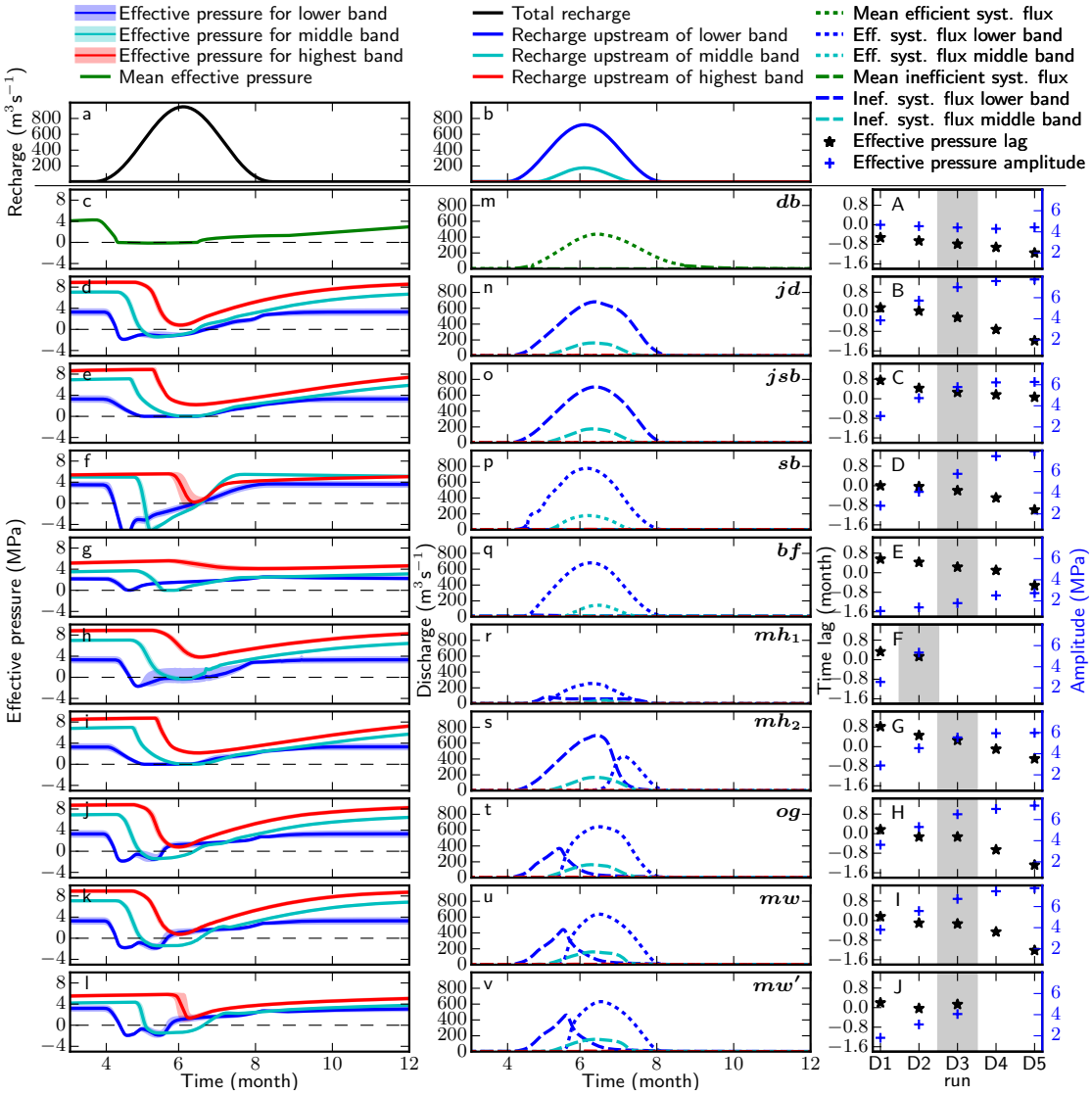

Figure A.5: Suite D results presented as in Figure A.4 but with the following differences: Middle column plots discharge at all three bands defined in Figure A.1a. The greyed region in the last column identifies the Run plotted in the two left columns.

A.6.5 Suite E: overdeepening of valley topography

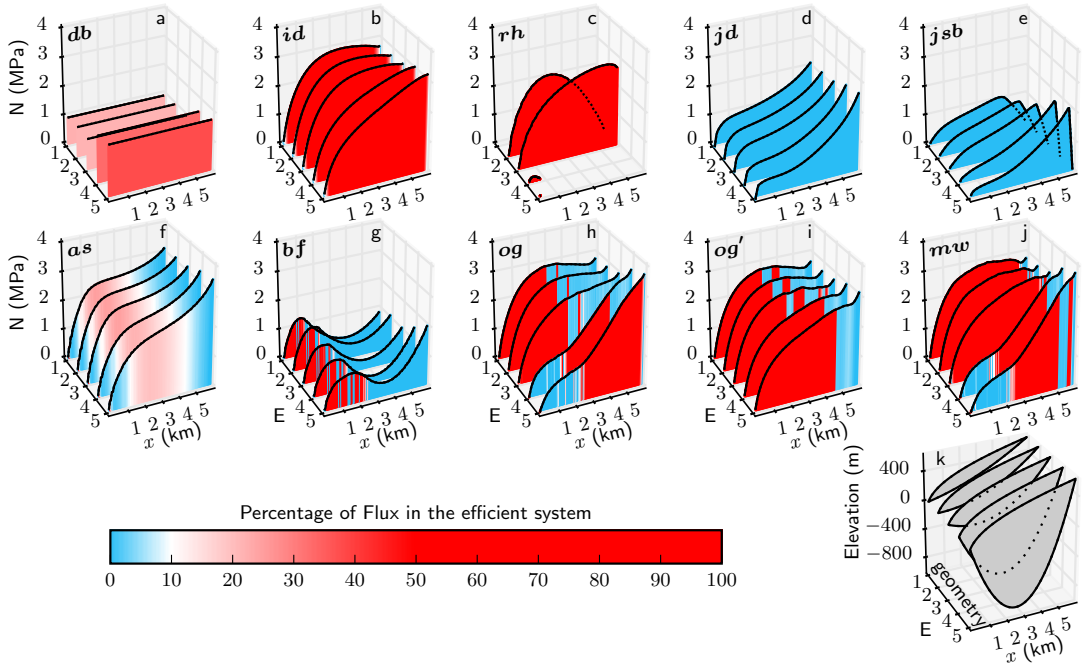

Figure A.6: Suite E results presented as in Figure A.2. The centreline topography used for each Run is shown in panel k. For the 2D models, the effective pressure and the fraction of the flux in the efficient system are calculated by averaging values in a 200 m wide band along the centre-line (hatched band in Figure A.1b).

Suite E tests the influence of an overdeepening on the simulated steady-state drainage system (Fig. A.6). This Suite is performed with the synthetic valley glacier topography shown in Figure A.1b. The main impact of an overdeepening should come through the pressure dependence of the melt-opening term (second term of eq. (A.7)), which at the supercooling threshold (e.g. Werder, 2016) should lead to shutdown of R channels. The overdeepenings in the topography for Runs E1 to E3 are not sufficient to reach the supercooling threshold. This threshold first appears in the geometry for Run E4.

The R channel shutdown is seen in the channel model *rh*: for Run E3 the model produces positive effective pressures throughout; however for E4 the model channel shuts down at ∼1 km and N drops to 0, at which point the model fails. The *id* model

has similar physics as rh but does not include the pressure-melt term in eq. (A.7). Consequently, the overdeepening has very little influence on the shape of the effective pressure curve as the (constant) surface slope is then the dominating influence.

Similarly, the cavity-sheet models jd and jsb that have no pressure-melt dependence (eq. (A.5)), show little impact of the overdeepening, producing positive effective pressures throughout. The pronounced difference between jd and jsb, particularly towards the upper glacier, is due to the fact that the jsb model constrains water pressure to always be positive. This means that effective pressure has to go to zero at all boundaries (where ice thickness is zero), including the upper glacier margin. All other 1D and 2D models that submitted results for Suite E (and F) ignore such constraints and generally produce negative water pressures in part of the valley glacier domain (see supplementary material). The as model, which is also a cavity-sheet model but includes opening by melt and a pressure dependent term, shows small effects due to the overdeepening. The different discharge formulation used in this model allows for representation of laminar and turbulent flow regimes, as well as the wide transition between them, producing smooth transitions between inefficient and efficient systems. As the topography deepens, more of the bed is in a flow regime closer to laminar (i.e. lower Reynolds number, with linear dependence on potential gradient). This represents weakening of efficient system (or channel shutdown) as the overdeepening becomes deeper, and is apparent in the extension of the downstream blue region (inefficient system) from E1 to E5 in Figure A.6f.

The cavity-sheet/channels models (og and mw) show no negative effective pressures, unlike rh, even though they do contain the pressure-melt term. However, N is reduced markedly in Runs E4 and E5, in which the supercooling threshold is exceeded and in the same region the drainage system transitions from efficient for $x > 2\,\mathrm{km}$ to inefficient for $0 < x < 2\,\mathrm{km}$. This means that the channel system does shut down and that the water is then carried in the cavity-sheet (and also in channels along the sides of the

overdeepening, compare supporting Figures S162 and S166 for example). og' is similar to og but the pressure-melt term is turned off. This model, again, therefore shows very little impact of the overdeepening and the efficient system operates over the full length of the glacier.

The porous-layer model bf shows a pronounced impact of the valley topography, N changes only slightly as the overdeepening is enlarged, so the bed topography has little impact. The model suggests that an efficient drainage system would exist between the margin and $x = 2\,\mathrm{km}$, transitioning to an inefficient system at $x > 2\,\mathrm{km}$. This causes the effective pressure to drop to a minimum at $x = 4\,\mathrm{km}$.

For the 0D model (db), which has no pressure-melt term, the effective pressure is similar for the first three Runs and then rises slightly for the last two. This is unlike the other models, which all show a decrease in effective pressure (albeit only a small one when there is no pressure-melt term). This effect may be caused by the use of an averaged topography in this lumped model.

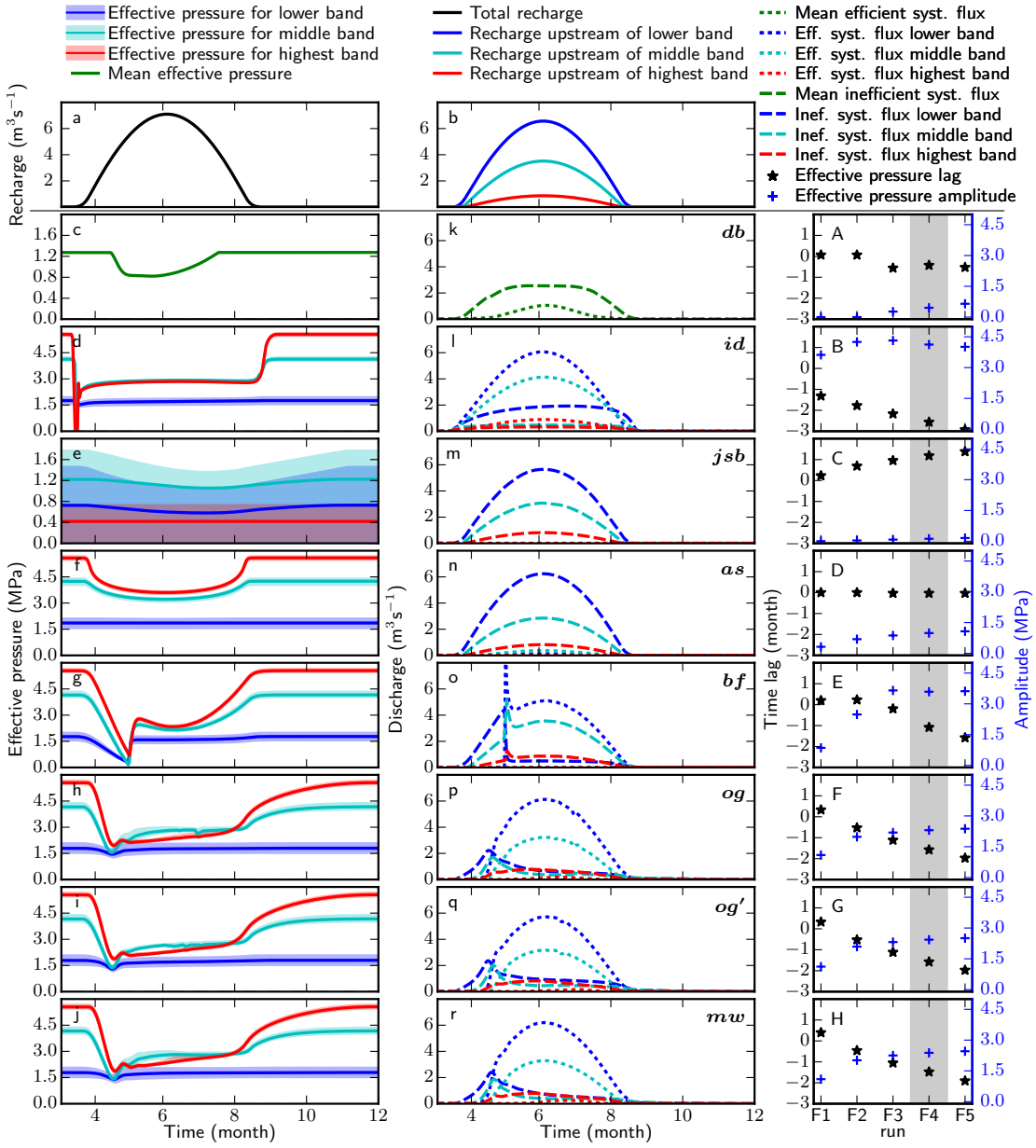

Figure A.7: Suite F results presented as in Figure A.5. The left and middle columns display results of Run F4. The three bands for which results are plotted are marked in Figure A.1b.

A.6.6 Suite F: seasonal cycle on valley topography

Suite F has the same objective as Suite D—to explore the seasonal drainage cycle—but with the valley-glacier topography of E1, without an overdeepening (Fig. A.1). The results are presented in the same style as Suites C and D with the discussion focusing on Run F4 (Fig. A.7 and supplementary material).

During winter, the effective pressure in all models is relatively high and markedly higher than during times of meltwater input (left column). The lowest N is produced by the jsb model, particularly at the highest elevation. This is again because this model constrains the water pressure to be positive, as mentioned above. This is also why the spread in effective pressures in the jsb model is the largest of all models (light coloured bands in Figure A.7e), as N is forced to zero at the lateral margins. All other models have very little lateral spread in effective pressure and they yield negative water pressures towards the margins.

As in Suite D, the models approximate a spring event when recharge sets in. However in the case of this geometry, there are larger variations in the shape of the pressure drop and its subsequent recovery. The 0D model db and the cavity-sheet models as and jsb show a gradual decrease in effective pressure. The ample water storage in model jsb explains this smoother evolution, while the low discharge through the efficient system of as model clarifies the evolution of its effective pressure. For the conduit model, id, the effective pressure response drops sharply in all elevation bands. This is followed by a rapid recovery to a steady summer value. The cavity-sheet/channels models og, og' and mw show a pronounced drop over about one month with a slight recovery after channelisation initiates (see discharge plot in middle column of Fig. A.7). These models then enter a summer mode in which the effective pressure rises slowly and steadily during the melt season. The porous-layer model, bf, shows a more gradual drop to almost zero effective pressure and then a rapid recovery as the efficient layer is activated. This is also clearly visible in the discharge plots.

At the end of the summer, the return to the winter state happens at different rates. In models db, id, as and bf the return occurs simultaneously with recharge shutdown. The cavity-sheet/channels models og, og' and mw and the cavity-sheet model jsb recover much more slowly over the course of a few months. Notice, too, that in the cavity-sheet/channels model og, og' and mw, there is a clear difference in the slope of the effective pressure between the summer regime and the return to the winter state at the end of the melt season.

The dynamic response to the different magnitudes of forcings Runs F1 to F5 (right column), shows that in most models the time of minimum effective pressure (taken as an average over the whole domain) leads the time of maximum recharge by around one month; this lead time increases with recharge intensity. Similarly, the amplitude of the effective pressure increases with increased forcing. Exceptions to this are: jsb, for which effective pressure lags recharge and the amplitude stays very low; and as, which shows an increasing amplitude but zero lag, because zero storage is used by this model in this Suite.

A.7 Discussion

The SHMIP exercise consists of six Suites of four to six Runs each. The Suites are designed to facilitate a comparison of several different models of the subglacial drainage system. The experiments were designed to enable participation of a wide variety of models, with the only requirement being that the effective pressure was computed. This excluded some models, notably the routing-type models which use a hydraulic potential (and thus effective pressure) that is independent of the state of the drainage system (e.g. Le Brocq et al., 2009); as well as the models that only consider local water balances, such as subglacial till models (e.g. Tulaczyk et al., 2000; Bougamont et al., 2014). Nonetheless, our publicly available results could be re-interpreted in terms of discharge only and

compared with outputs of those types of models.

To allow a comparison of models with different physical approaches, two reference simulations are provided. This allowed participation of models requiring tuning. The choice of the reference Runs (ice sheet geometry, steady state and uniform input Runs A3 and A5) is such that fitting to these results should not bias the rest of the intercomparison, in which simulations with different characteristics are presented. Likewise, the choice of a cavity-sheet/channels model for this reference simulation (mw) is motivated by the fact that this approach is the most widespread and therefore these reference models give a set of parameters for the bulk of existing models. The tuning procedure (or need for tuning) was left to the discretion of the experimenter and was not a mandatory step of the intercomparison. Note that models that are tuned use parameter values that are similar to those used in other studies conducted with these same models.

The 13 participating models show a broad agreement between each other in all Suites. In particular, they agree with one of the fundamental theoretical considerations of subglacial drainage: in an inefficient drainage system a discharge increase will lead to a decrease in steady-state effective pressure and conversely, in an efficient drainage system, a discharge increase will lead to an increase in steady-state effective pressure (Fig. A.2). Conversely, none of the models produce the low effective pressure that is usually observed during winter (e.g. Wright et al., 2016). The more specific responses of the models are generally comparable across groups of models incorporating similar physics (see "Model type" in Table A.1). In view of the complexity in analysing and interpreting the published subglacial hydrology records (e.g. Rada and Schoof, 2018), our discussion of the SHMIP results focuses primarily on an intercomparison of the model outputs. A direct comparison to observations is beyond the scope of this study and is left to a future SHMIP.

A large number of models use a cavity-sheet drainage system (jd, jsb, as, mh_1, mh_2, og, mw), which leads to consistent results for all of these in low recharge scenarios

(A1–A3, winter period of D and F). The 0D conduit model *db* also produces results consistent with the cavity-sheet models for those scenarios. The other models show different behaviours at low recharge: the two layered porous-layer models (bf) as well as macroporous-sheet model (cdf) produce much higher effective pressures than the cavity-sheet models. This is because the conductivity of the inefficient drainage system in these models does not adapt to the discharge of the system. Conversely, the 1D channel or conduit models (rh, id), which are designed for higher recharge scenarios, show much lower effective pressure at low discharge, which is consistent with R channel. The scaling of the transmitivity to a cavity opening formulation in the single layer porous model (sb) allows a reduction in the layer conductivity at low discharge yielding effective pressure distributions closer to those of mw.

For higher recharge Runs, the response of the models with and without an efficient drainage component diverge as can be seen in Suite A (Run A4 to A6) and E1 and E2 (which have no overdeepening). Notably, the representation of the efficient drainage system in the porous-layer models seems to capture the dynamics observed in the cavity-sheet/channels models for Suite A rather well. However, although the differences between cavity-sheet-only and cavity-sheet/channels models are large for the steady state Runs (Suites A, B and E), they are much smaller for seasonal forcings (Suites D and F). For example, jd is very similar to mw in Suite D except in the band closest to the margin (10–15 km, Fig. A.5). The likely cause of this is that the transient "summer" states in Suites D and F are far from a steady-state channelised system. This means that in those seasonal Runs the distributed system drains more of the subglacial discharge than it would in a steady-state corresponding to a high magnitude summer recharge. This interpretation can be supported by field measurements. Based on borehole observations in a land-terminating area of the Greenland Ice Sheet, Meierbachtol et al. (2013) suggested that channels do not reach further inland than approximately 20 km. In the same region, tracer experiments suggest that the channelised system extends inland at least 41 km

but not as far as 57 km (Chandler et al., 2013).

The impact of topography on steady-states can be seen by comparing results of the high recharge Runs of Suite A (A5, A6) with the Run E1 (or E2) of Suite E, in which there is no overdeepening and recharge is similar. The channel models (*db*, *id*, *rh*, *og*, *mw*) produce about double the values of effective pressure in E1 versus A6 (e.g. *id* in Figure A.2b vs. Figure A.6b). This is due to the steeper surface slopes and shorter glacier length in the valley domain. Similarly, the cavity-sheet-only models (*jd*, *jsb*, *as*) produce effective pressures near zero in A6, whereas in E1 they are ∼1 MPa, again due to the influence of topography.

The moulin-recharge Suite B illustrates that the impact of localised input on average effective pressure is relatively minor in all models, with variations usually less than 10% of the ice overburden pressure. However, there is one exception: it matters where the upper moulin is located, as above that moulin the effective pressure is much higher than predicted by a uniform input. The farthest inland location where water reaches the glacier bed is indeed a topic of current studies (e.g. Hoffman et al., 2018a; Gagliardini and Werder, 2018; Poinar et al., 2015). Introducing localised inputs also modifies the local effective pressure (with lower effective pressure at the moulin locations) and the distribution of the efficient channelised drainage system (see supplementary figures). This decrease of effective pressure at moulin locations is consistent with observations that hydraulic head is higher in the vicinity of moulins (Andrews et al., 2014; Gulley et al., 2012).

The transient Runs illustrate the importance of storage (in the sense of a direct functional relationship between pressure and storage as in eq. (A.10)) and also of storage-like effects that can arise from numerical regularisation. In the diurnal-variation Suite, C, storage impacts the amplitude of the pressure variation, with results ranging from almost zero (high storage) to 13 MPa (no storage) (Fig. A.4). These amplitudes can be compared with observations from Haut Glacier d'Arolla (Gordon et al., 1998), where

amplitudes varying from 0 to 0.9 MPa were observed in a cluster of boreholes. Note that two models, jsb and mh_2, do not implement actual storage but use a storage-like term to regularise the pressure equation (see Bueler and van Pelt, 2015). This results in some of the same effects as actual storage. The discharge also has a muted diurnal variation, compared with recharge, as storage increases. Therefore, observations of recharge and proglacial discharge could help further constrain the storage capacity of a glacier drainage system (e.g. Brinkerhoff et al., 2016; Bartholomew et al., 2012; Huss et al., 2007).

For the seasonal forcings (Suites D and F), storage has a lesser impact as the drainage system has more time to react to the more gradual change in recharge. In the mw model, increasing storage (mw') leads to lower effective pressure during the winter and also to a delayed but sharper response in spring in the two higher elevation bands. The former is due to increased water flow (and thus lower N) during winter as more water can be released from storage. The latter is due to the dampening effect that increased storage has on the subglacial water pressure response.

The seasonal-forcing Runs of all models produce an effective pressure that is high, higher, in fact than at any time during the melt season (except for the porous-layer models in the highest elevation band in Suite D, Figure A.5f,g). This is contrary to many borehole observations (e.g. Rada and Schoof, 2018; Dow et al., 2011; Fudge et al., 2005), which show a shutdown of the drainage system leading to effective pressures around zero. There has been some recent progress in modelling such a shutdown (Rada and Schoof, 2018; Dow et al., 2018; Downs et al., 2018; Hoffman et al., 2016) but none of the participating models include such processes. An alternative view is that the participating models, as well as many others, only simulate a well-connected system which could potentially persist at high effective pressures throughout the winter with a footprint, however, small enough that it is rarely observed.

All the models show pronounced "spring events", with low effective pressure as the surface melt forcing sets in (Iken and Bindschadler, 1986), in both Suites D and F. The

effective pressure then increases again as the drainage system adjusts to the higher flux. Of note is that this increase in effective pressure also occurs in models with only an inefficient system, such as jd (Fig. A.5d). This is because an inefficient system will also (transiently) respond to an increase in recharge with an effective pressure drop and a subsequent rise as the drainage space and thus the efficiency increases (eq. (A.4)), as explained in Hoffman and Price (2014). The duration of the effective pressure drop varies from less than a month to several months. These pressure drops are consistent with observed speed-up events ranging from one to several months depending on the location of the measurements (van de Wal et al., 2015; Hoffman et al., 2011; Bartholomew et al., 2010).

Most models reach negative effective pressures in Suite D for extended periods of time in both the lower and middle band. The models that do not reach negative N either constrain it to be positive (db, jsb, mh_2) or, in the case of bf, instantly activate the efficient drainage system when $N = 0$ is reached (this activation can be seen nicely in Figure A.7o). The positivity of N is arguably the more realistic behaviour as month-long periods of negative effective pressures over the large areas predicted by the other participating models is not observed and would have a much more dramatic impact on ice dynamics than "spring events". However, probably none of the models capture the drainage system dynamics correctly as N approaches zero , as then uplift of the ice, including non-local effects due to elastic and viscous behaviours, should occur (Walker et al., 2017; Tsai and Rice, 2010). Note that in the seasonal Suite, F, zero or negative effective pressures are reached only very briefly by bf and id. All others models have $N > 0.7\,\mathrm{MPa}$. Again this is due to the larger surface slopes and shorter length of the valley topography compared to the topography of Suite D.

The simulated transitions back to the winter state at the end of the melt season are of varying temporal length. The porous-layer models recover very quickly, in less than a month for Suite D and even more rapidly for F, afterwards the effective pressure only

increases slightly. The cavity-sheet models, in addition to the 0D-conduit model, *db*, react much more slowly. In Suite D they transition to the winter state over three to four months. The large-scale effective pressure considered in SHMIP (mean value over an altitudinal band rather than local effective pressure) is not necessarily suited for direct comparison with observations. However, the idea of different "stages" (Rada and Schoof, 2018) is particularly helpful. The transition of effective pressure back to its winter level can be compared to "stage 2", which lasts around a month and is approximately represented in our seasonal Suite F for the valley glacier topography. This result, however, depends on the interpretation of both the model results and the field observations and will be open for debate until more efficient ways to compare modelled and measured effective pressure are developed.

Of the participating models, the most physically complex models are the cavity-sheet/channels models. They largely reproduce theoretically expected behaviours as explained above. This is why we picked the outputs of such a model as tuning benchmarks (Runs A3 and A5 of *mw*). The models that used this tuning were the ones which use implementations based on different draining components: the macroporous-sheet model (*cdf*), the porous-layer models (*sb*, *bf*), a cavity-sheet model including energy dissipation (*as*), and another cavity-sheet model (*jd*) in only a subset of the experiments. None of the participating models incorporated physically based theories of drainage other than cavity(-sheets) and R channels. Thus, models involving canals (Walder and Fowler, 1994) or other distributed drainage types (e.g. Creyts and Schoof, 2009) are not represented.

Models that implement only a cavity-sheet show shortcomings when applied to higher input scenarios, producing effective pressures that are too low. However, in the seasonal Runs, which are likely the most realistic forcings in this intercomparison exercise, they are not much different from the cavity-sheet/channels models even though recharge is high in mid summer. This high input can, in the case of these cavity-sheet only models,

be accommodated by the increase in efficiency of the cavity-sheet system. This shows that they are probably applicable to many situations. However, they lack the fast rebound of the effective pressure in their frontal region, which might be quite relevant for ice dynamics (e.g. van de Wal et al., 2015). On the other hand, they benefit from less model complexity and from a clearer mathematical foundation, in the sense that they approximate a continuum solution (Bueler and van Pelt, 2015). The *as* model gains wider applicability by introducing the pressure melting-opening term (e.g. Run A6). The momentum equation used in this model facilitates the transition between flow regimes, thus allowing the process of self-organised channelisation to occur stably, while including the melt term everywhere (Sommers et al., 2018). Previous model formulations found the inclusion of a melt term to be problematic (Schoof et al., 2012) albeit possible (Dow et al., 2018).

The porous-layer models yield results that are similar to those of the cavity sheet/channels models for many of the Suites. The *sb* model is able to generate quite complex effective pressure variations with a single layer model. The double layer approach of bf is applicable to the steeper valley glacier topography and produces a response comparable to that of the cavity sheet/channels models in Suite F.

The results from the 0D, conduit model (*db*) show that simplification can be pushed far. The overall behaviour of the model is qualitatively in line with the more complex cavity sheet/channels models. However, the results of this model are biased toward lower effective pressure and compare better to values in the lower region of the domain than to the overall mean value of the spatially distributed models. This could be due not only to the design of the model itself, but also to the chosen parameterisation or chosen topography. Also notable is the fact that the *db* model is one of the few subglacial drainage models that has been rigorously fit to observations using Bayesian methods (Brinkerhoff et al., 2016); most other models have only been hand-tuned (if at all) to fit observations (e.g. Koziol and Arnold, 2018; de Fleurian et al., 2016).

The three 1D models (rh, cdf, id) show results consistent with the theories they implement. Their shortcomings are likely related more to approximations of the theory than to the fact they are implemented in only one dimension. This is in part due to the fairly one-dimensional geometries of our test Suites. The performance of these models suggests that 1D models are valuable in settings where geometry can be reduced to a flow line with insignificant lateral variation.

A.8 Conclusion

Thirteen models participated in this first Subglacial Hydrology Hodel Intercomparison Project (SHMIP). They incorporate a wide range of different drainage system types, with a focus on inefficient drainage through linked-cavities, efficient drainage through R channels, and approximations of both of these systems by using drainage through porous-layers. All participating models were required to calculate effective pressure distributions. Models incorporating other physically based theories of drainage such as canals (Walder and Fowler, 1994) or other distributed drainage types (e.g. Creyts and Schoof, 2009) did not participate. While routing models were excluded, since they fail to compute effective pressure, which is a diagnostic variable in our tests.

The test Suites of SHMIP cover a range of scenarios similar to those to which subglacial drainage models are currently applied . The Suites use synthetic, idealised topographies of a land-terminating ice-sheet margin and a mountain glacier, with idealised recharge forcing, ranging from steady input to seasonal and diurnal variations. However, a few interesting and relevant scenarios are not included, such as the classic test case of jokulhlaups (e.g. Flowers et al., 2004; Clarke, 2003; Nye, 1976). A tidewater glacier test-case is also missing, although such a case would be interesting in both Greenland-like and Antarctica-like scenarios (e.g. Dow et al., 2016). Considering realistic modelling, some more complex forcings, such as a seasonal forcing with superimposed diurnal variations,

and also real glacier topography would be of interest. These will be useful test targets to be included in a future iteration of SHMIP.

This intercomparison project provides a qualitative comparison of several state-of-the-art and legacy subglacial hydrology models. The use of a two-component model is strongly advised when considering high recharge scenarios, complex topographies, or observing short term variations in the subglacial hydrological system. For larger systems with low water fluxes, the use of a cavity-sheet only model should be considered as they achieve results comparable to more complex cavity-sheet/channels models. These cavity-sheet/channels models are required when the dynamics of the efficient system is important, as in valley glaciers, or when recharge is constant enough to let channels develop. Porous layer models are a viable approximation to the more physically realistic approaches in that they capture, qualitatively, the inefficient and efficient system dynamics, but a careful assessment of their parameters and flux formulations should be performed to ensure that they accurately represent the flow regime corresponding to the recharge applied to the model.

This intercomparison reveals that the effect of localised drainage is important on small scales but does not have a significant impact on the overall distribution of water pressure. However, special care should be taken when specifying the location of the highest-altitude input point, as this altitude has a significant effect on the subglacial water pressure downstream.

Experiments introducing diurnal and seasonal variations emphasise the impact of water storage on the results of the models and more particularly on the timing of their response in terms of pressure. This could enable the parameterisation of storage from observations of the lag between water input and pressure response, and also put a constraint on models which introduce storage as part of their equations (as the porous layer models for example) or as a stabilisation mechanism (as in mh_1 for example).

Another well-known and important point, also highlighted by this exercise, is the need

to use appropriate model parameters. However, these parameters are often largely unknown and future efforts should focus on inferring them from observations (e.g. Brinkerhoff et al., 2016; Werder et al., 2010), or through other means such as laboratory experiments. Once these techniques of parameter inversion of subglacial drainage models become more established and reliable, a SHMIP exercise using observational data will become viable.

A.9 Contribution statement

B.dF. and M.A.W. designed the experiments, ran their respective models, analysed the model results and wrote the paper. All the other co-authors ran their respective models and provided feedback both on the intercomparison design and paper writing.

A.10 Acknowledgements

B.dF. and M.A.W. want to thank everyone that took part in the discussions leading to SHMIP (Tim Creyts, Ian Hewitt, Christian Schoof, Gwenn Flowers, Jesse Johnson, Ed Bueler, Ugo Nanni, Angelika Humbert, Alison Banwell, Ian Willis, Stephen Price and others). B.dF. was supported by the European Research Council under the European Community 7th Framework Programme (FP7/2007–2013)/ERC under Grant Number 610055 (ICE2ICE) and computations were performed on resources provided by UNINETT Sigma2 - the National Infrastructure for High Performance Computing and Data Storage in Norway S.B. was supported by the GreenRISE project, a project funded by Leibniz-Gemeinschaft: WGL Pakt für Forschung SAW2014-PIK-1. I.D. was supported by the Swiss National Science Foundation (SNSF) National Research Programme (NRP) 70 “Energy Turnaround”, Project No.153927. C.D. was supported by the Canada Research Chairs Programme and the Natural Sciences and Engineering Re-

search Council of Canada (Discovery - RGPIN-03761-2017) J.D. wants to thank Jesse Johnson for his help in implementing the model, he was funded for this work by NSF grant 1543533. O.G. was supported by the Agence Nationale pour la Recherche (ANR) through the SUMER project (Blanc SIMI 6-2012). M.J.H. was supported by the Laboratory Directed Research and Development Early Career Research Program at Los Alamos National Laboratory (20160608ECR). J.S. was supported by the Swiss National Science Foundation (SNSF) grant no. 200021-153179/1 to M. Funk and the Swiss National Supercomputing Centre (CSCS) allocation no. s573 to J. Seguinot. A.S. was supported primarily by a NASA Earth and Space Science Fellowship (NNX14AL24H), and thanks Harihar Rajaram and Mathieu Morlighem for their invaluable contributions to model formulation and development. The authors want to thank two anonymous reviewers and the editor F. Pattyn for constructive comments that help to improve this manuscript.

Bibliography

Andrews, L. C., Catania, G. A., Hoffman, M. J., Gulley, J. D., Luethi, M. P., Ryser, C., Hawley, R. L., and Neumann, T. A. (2014). Direct observations of evolving subglacial drainage beneath the greenland ice sheet. *Nature*, 514(7520).

Bartholomew, I., Nienow, P., Mair, D., Hubbard, A., King, M. A., and Sole, A. (2010). Seasonal evolution of subglacial drainage and acceleration in a Greenland outlet glacier. *Nat. Geosci.*, 3(6):408–411.

Bartholomew, I., Nienow, P., Sole, A., Mair, D., Cowton, T., and King, M. A. (2012). Short-term variability in Greenland Ice Sheet motion forced by time-varying meltwater drainage: Implications for the relationship between subglacial drainage system behavior and ice velocity. *J. Geophys. Res.*, 117(F3):F03002.

Beyer, S., Kleiner, T., Aizinger, V., Rückamp, M., and Humbert, A. (2017). A confined–

unconfined aquifer model for subglacial hydrology and its application to the north east Greenland ice stream. *The Cryosphere Discussions*, 2017:1–24.

Bougamont, M., Christoffersen, P., Hubbard, A. L., Fitzpatrick, A. A., Doyle, S. H., and Carter, S. P. (2014). Sensitive response of the Greenland Ice Sheet to surface melt drainage over a soft bed. *Nature Comms.*, 5.

Brinkerhoff, D. J., Meyer, C. R., Bueler, E., Truffer, M., and Bartholomaus, T. C. (2016). Inversion of a glacier hydrology model. *Ann. Glaciol.*, 57(72):84–95.

Bueler, E. and van Pelt, W. (2015). Mass-conserving subglacial hydrology in the Parallel Ice Sheet Model version 0.6. *Geoscientific Model Development*, 8(6):1613–1635.

Chandler, D., Wadham, J., Lis, G., Cowton, T., Sole, A., Bartholomew, I., Telling, J., Nienow, P., Bagshaw, E., Mair, D., et al. (2013). Evolution of the subglacial drainage system beneath the Greenland Ice Sheet revealed by tracers. *Nat. Geosci.*, 6(3):195–198.

Clarke, G. (2003). Hydraulics of subglacial outburst floods: new insights from the Spring-Hutter formulation. *J. Glaciol.*, 49(165):299–313.

Clarke, G. K. C. (1987). A short history of scientific investigations on glaciers. *J. Glaciol.*, special issue:4–24.

Creyts, T. T. and Schoof, C. G. (2009). Drainage through subglacial water sheets. *J. Geophys. Res.*, 114(F4):F04008.

Cuffey, K. M. and Paterson, W. S. B. (2010). *The Physics of Glaciers, 4th Edition*. Elsevier, Oxford.

de Fleurian, B., Gagliardini, O., Zwinger, T., Durand, G., Le Meur, E., Mair, D., and Råback, P. (2014). A double continuum hydrological model for glacier applications. *The Cryosphere*, 8(1):137–153.

de Fleurian, B., Morlighem, M., Seroussi, H., Rignot, E., van den Broeke, M. R., Munneke, P. K., Mouginot, J., Smeets, P. C. J. P., and Tedstone, A. J. (2016). A modeling study of the effect of runoff variability on the effective pressure beneath Russell Glacier, West Greenland. *J. Geophys. Res*, 121(10).

de Fleurian, B., Werder, M. A., Beyer, S., Brinkerhoff, D. J., Delaney, I., Dow, C. F., Downs, J., Gagliardini, O., Hoffman, M. J., Hooke, R. L., Seguinot, J., and Sommers, A. N. (2018). Results from the SHMIP exercise. e-collection.

Dow, C. F., Karlsson, N. B., and Werder, M. A. (2018). Limited impact of subglacial supercooling freeze-on for Greenland Ice Sheet stratigraphy. *Geophys. Res. Lett.*, 45(3):1481–1489.

Dow, C. F., Kavanaugh, J. L., Sanders, J. W., Cuffey, K. M., and MacGregor, K. R. (2011). Subsurface hydrology of an overdeepened cirque glacier. *J. Glaciol.*, 57(206):1067–1078.

Dow, C. F., Werder, M. A., Nowicki, S., and Walker, R. T. (2016). Modeling Antarctic subglacial lake filling and drainage cycles. *The Cryosphere*, 10(4):1381–1393.

Downs, J., Johnson, J., Harper, J., Meierbachtol, T., and Werder, M. (2018). Dynamic hydraulic conductivity reconciles mismatch between modeled and observed winter subglacial water pressure. *J.Geophys. Res.*, 123(4):818–836.

Doyle, S. H., Hubbard, A., Fitzpatrick, A. A. W., van As, D., Mikkelsen, A. B., Pettersson, R., and Hubbard, B. (2014). Persistent flow acceleration within the interior of the Greenland Ice Sheet. *Geophys. Res. Lett.*, 41(3):899–905.

Engelhardt, H. and Kamb, B. (1998). Basal sliding of Ice Stream B, West Antarctica. *J. Glaciol.*, 44(147):223–230.

Farinotti, D., Brinkerhoff, D. J., Clarke, G. K. C., Fürst, J. J., Frey, H., Gantayat, P., Gillet-Chaulet, F., Girard, C., Huss, M., Leclercq, P. W., Linsbauer, A., Machguth, H., Martin, C., Maussion, F., Morlighem, M., Mosbeux, C., Pandit, A., Portmann, A., Rabatel, A., Ramsankaran, R., Reerink, T. J., Sanchez, O., Stentoft, P. A., Singh Kumari, S., van Pelt, W. J. J., Anderson, B., Benham, T., Binder, D., Dowdeswell, J. A., Fischer, A., Helfricht, K., Kutuzov, S., Lavrentiev, I., McNabb, R., Gudmundsson, G. H., Li, H., and Andreassen, L. M. (2017). How accurate are estimates of glacier ice thickness? Results from ITMIX, the Ice Thickness Models Intercomparison eXperiment. *The Cryosphere*, 11(2):949–970.

Flowers, G. E. (2015). Modelling water flow under glaciers and ice sheets. *Proc. R. Soc. A*, 471(2176):1–41.

Flowers, G. E., Bjornsson, H., Palsson, F., and Clarke, G. K. C. (2004). A coupled sheet-conduit mechanism for jökulhlaup propagation. *Geophys. Res. Lett.*, 31(5):1–4.

Flowers, G. E. and Clarke, G. K. C. (2002). A multicomponent coupled model of glacier hydrology - 1. Theory and synthetic examples. *J. Geophys. Res.*, 107(B11):2287.

Fudge, T. J., Harper, J. T., Humphrey, N. F., and Pfeffer, W. T. (2005). Diurnal water-pressure fluctuations: timing and pattern of termination below Bench Glacier, Alaska, USA. *Ann. Glaciol.*, 40(1):102–106.

Fudge, T. J., Humphrey, N. F., Harper, J. T., and Pfeffer, W. T. (2008). Diurnal fluctuations in borehole water levels: configuration of the drainage system beneath Bench Glacier, Alaska, USA. *J. Glaciol.*, 54(185):297–306.

Gagliardini, O. and Werder, M. A. (2018). Influence of an increasing surface melt over decadal timescales on land terminating outlet glaciers. *J. Glaciol.*, pages 1–11.

Gordon, S., Sharp, M., Hubbard, B., Smart, C., Ketterling, B., and Willis, I. (1998). Sea-

sonal reorganization of subglacial drainage inferred from measurements in boreholes. *Hydrol. Process.*, 12(1):105–133.

Gulley, J. D., Grabiec, M., Martin, J. B., Jania, J., Catania, G., and Glowacki, P. (2012). The effect of discrete recharge by moulins and heterogeneity in flow-path efficiency at glacier beds on subglacial hydrology. *J. Glaciol.*, 58(211):926–940.

Hewitt, I. J. (2011). Modelling distributed and channelized subglacial drainage: the spacing of channels. *J. Glaciol.*, 57(202):302–314.

Hewitt, I. J. (2013). Seasonal changes in ice sheet motion due to melt water lubrication. *Earth Planet. Sci. Lett.*, 371-372(0):16 – 25.

Hoffman, M. and Price, S. (2014). Feedbacks between coupled subglacial hydrology and glacier dynamics. *J. Geophys. Res.*, 119(3):414–436.

Hoffman, M. J., Andrews, L. C., Price, S. F., Catania, G. A., Neumann, T. A., Lüthi, M. P., Gulley, J., Ryser, C., Hawley, R. L., and Morriss, B. (2016). Greenland subglacial drainage evolution regulated by weakly connected regions of the bed. *Nature Comms.*, 7.

Hoffman, M. J., Catania, G. A., Neumann, T. A., Andrews, L. C., and Rumrill, J. A. (2011). Links between acceleration, melting, and supraglacial lake drainage of the western greenland ice sheet. *J. Geophys. Res.*, 116, F04035:1–16.

Hoffman, M. J., Perego, M., Andrews, L. C., Price, S. F., Neumann, T. A., Johnson, J. V., Catania, G., and Lüthi, M. P. (2018a). Widespread moulin formation during supraglacial lake drainages in Greenland. *Geophys. Res. Lett.*, 45(2):778–788.

Hoffman, M. J., Perego, M., Price, S. F., Lipscomb, W. H., Jacobsen, D., Tezaur, I., Salinger, A. G., Tuminaro, R., and Zhang, T. (2018b). MPAS-Albany Land Ice

(MALI): a variable resolution ice sheet model for earth system modeling using Voronoi grids. *Geoscientific Model Development Discussions*, pages 1–47.

Hooke, R. L., Laumann, T., and Kohler, J. (1990). Subglacial water pressure and the shape of subglacial water conduits. *J. Glaciol.*, 36(122):67–71.

Huss, M., Bauder, A., Werder, M., Funk, M., and Hock, R. (2007). Glacier-dammed lake outburst events of Gornersee, Switzerland. *J. Glaciol.*, 53(181):189–200.

Huybrechts, P., Payne, A., and the EISMINT Intercomparison Group (1996). The EISMINT benchmarks for testing ice-sheet models. *Ann. Glaciol.*, 23:1–14.

Iken, A. and Bindschadler, R. A. (1986). Combined measurements of subglacial water pressure and surface velocity of Findelengletscher, Switzerland: conclusions about drainage system and sliding mechanism. *J. Glaciol.*, 32(110).

Iken, A., Echelmeyer, K., Harrison, W., and Funk, M. (1993). Mechanisms of fast flow in Jakobshavns-Isbræ, West Greenland. 1. measurements of temperature and water-level in deep boreholes. *J. Glaciol.*, 39(131):15–25.

Iken, A. and Truffer, M. (1997). The relationship between subglacial water pressure and velocity of Findelengletscher, Switzerland, during its advance and retreat. *J. Glaciol.*, 43(144):328–338.

Joughin, I., Smith, B. E., and Howat, I. (2018). Greenland ice mapping project: Ice flow velocity variation at submonthly to decadal time scales. *The Cryosphere*, 12(7):2211–2227.

Kamb, B. (1987). Glacier surge mechanism based on linked cavity configuration of the basal water conduit system. *J. Geophys. Res.*, 92(B9):9083–9099.

Kavanagh, M. and Tarasov, L. (2017). BrAHMs v1.0: A fast, physically-based subglacial

hydrology model for continental-scale application. *Geoscientific Model Development Discussions*, 2017:1–20.

Kessler, M. A. and Anderson, R. S. (2004). Testing a numerical glacial hydrological model using spring speed-up events and outburst floods. *Geophys. Res. Lett.*, 31(18):1–5.

Koziol, C. P. and Arnold, N. (2018). Modelling seasonal meltwater forcing of the velocity of land-terminating margins of the Greenland Ice Sheet. *The Cryosphere*, 12(3):971–991.

Le Brocq, A., Payne, A., Siegert, M., and Alley, R. (2009). A subglacial water-flow model for West Antarctica. *J. Glaciol.*, 55(193):879–888.

Meierbachtol, T., Harper, J., and Humphrey, N. (2013). Basal drainage system response to increasing surface melt on the Greenland Ice Sheet. *Science*, 341(6147):777–779.

Morlighem, M., Seroussi, H., Larour, E., and Rignot, E. (2013). Inversion of basal friction in Antarctica using exact and incomplete adjoints of a higher-order model. *J. Geophys. Res.*, 118(3):1746–1753.

Nye, J. F. (1973). Water at the bed of a glacier. Technical report, H. H. Wills Physics Laboratory, University of Bristol, Bristol, England.

Nye, J. F. (1976). Water flow in glaciers: jökulhlaups, tunnels and veins. *J. Glaciol.*, 17(76):181–207.

Oreskes, N., Shrader-Frechette, K., and Belitz, K. (1994). Verification, validation, and confirmation of numerical models in the earth sciences. *Science*, 263(5147):641–646.

Pattyn, F., Perichon, L., Aschwanden, A., Breuer, B., de Smedt, B., Gagliardini, O., Gudmundsson, G. H., Hindmarsh, R. C. A., Hubbard, A., Johnson, J. V., Kleiner, T., Konovalov, Y., Martin, C., Payne, A. J., Pollard, D., Price, S., Rückamp, M., Saito, F., Soucek, O., Sugiyama, S., and Zwinger, T. (2008). Benchmark experiments

for higher-order and full-stokes ice sheet models (ISMIP-HOM). *The Cryosphere*, 2(2):95–108.

Pattyn, F., Perichon, L., Durand, G.and Favier, L., Gagliardini, O., Hindmarsh, R. C. A., Zwinger, T., Albrecht, T., Cornford, S., Docquier, D., Fuerst, J., Goldberg, D., Gudmundsson, H., Humbert, A., Hutten, M., Huybrecht, P., Jouvet, G., Kleiner, T., Larour, E., Martin, D., Morlighem, M., Payne, A., Pollard, D., Ruckamp, M., Rybak, O., Seroussi, H., Thoma, M., and Wilkens, N. (2013). Grounding-line migration in plan-view marine ice-sheet models: results of the ice2sea MISMIP3d intercomparison. *J. Glaciol.*, 59(215):410–422.

Pattyn, F., Schoof, C., Perichon, L., Hindmarsh, R. C. A., Bueler, E., de Fleurian, B., Durand, G., Gagliardini, O., Gladstone, R., Goldberg, D., Gudmundsson, G. H., Huybrechts, P., Lee, V., Nick, F. M., Payne, A. J., Pollard, D., Rybak, O., Saito, F., and Vieli, A. (2012). Results of the Marine Ice Sheet Model Intercomparison Project, MISMIP. *The Cryosphere*, 6(3):573–588.

Payne, A. J., Huybrechts, P., Abe-Ouchi, A., Calov, R., Fastook, J. L., Greve, R., Marshall, S. J., Marsiat, I., Ritz, C., Tarasov, L., and Thomassen, M. P. (2000). Results from the EISMINT model intercomparison: the effects of thermomechanical coupling. *J. Glaciol.*, 46(153):227–238.

Pimentel, S. and Flowers, G. E. (2010). A numerical study of hydrologically driven glacier dynamics and subglacial flooding. *Proc. R. Soc. A*, 467(2126):537–558.

Poinar, K., Joughin, I., Das, S. B., Behn, M. D., Lenaerts, J., and Broeke, M. R. (2015). Limits to future expansion of surface-melt-enhanced ice flow into the interior of western Greenland. *Geophys. Res. Lett.*, 42(6):1800–1807.

Rada, C. and Schoof, C. (2018). Subglacial drainage characterization from eight years

of continuous borehole data on a small glacier in the yukon territory, canada. *The Cryosphere Discussions*, 2018:1–42.

Ridley, J., Gregory, J. M., Huybrechts, P., and Lowe, J. (2010). Thresholds for irreversible decline of the Greenland Ice Sheet. *Climate Dynamics*, 35(6):1049–1057.

Röthlisberger, H. (1972). Water pressure in intra- and subglacial channels. *J. Glaciol.*, 11(62):177–203.

Röthlisberger, H. and Lang, H. (1987). *Glacio-Fluvial Sediment Transfer: An Alpine Perspective*. John Wiley and Sons, New York, NY, USA.

Schoof, C. (2010). Ice-sheet acceleration driven by melt supply variability. *Nature*, 468(7325):803–806.

Schoof, C., Hewitt, I. J., and Werder, M. A. (2012). Flotation and free surface flow in a model for subglacial drainage. Part I: Distributed drainage. *Journal of Fluid Mechanics*, 702:126–156.

Shannon, S. R., Payne, A. J., Bartholomew, I. D., van den Broeke, M. R., Edwards, T. L., Fettweis, X., Gagliardini, O., Gillet-Chaulet, F., Goelzer, H., Hoffman, M. J., Huybrechts, P., Mair, D. W. F., Nienow, P. W., Perego, M., Price, S. F., Smeets, C. J. P. P., Sole, A. J., van de Wal, R. S. W., and Zwinger, T. (2013). Enhanced basal lubrication and the contribution of the Greenland Ice Sheet to future sea-level rise. *Proceedings of the National Academy of Sciences*, 110(35):14156–14161.

Shoemaker, E. M. (1986). Subglacial hydrology for an ice sheet resting on a deformable aquifer. *J. Glaciol.*, 32(110):20–30.

Shreve, R. L. (1972). Movement of water in glaicers. *J. Glaciol.*, 11(62):205–214.

Smith, L. C., Yang, K., Pitcher, L. H., Overstreet, B. T., Chu, V. W., Rennermalm, Å. K., Ryan, J. C., Cooper, M. G., Gleason, C. J., Tedesco, M., Jeyaratnam, J., van

As, D., van den Broeke, M. R., van de Berg, W. J., Noël, B., Langen, P. L., Cullather, R. I., Zhao, B., Willis, M. J., Hubbard, A., Box, J. E., Jenner, B. A., and Behar, A. E. (2017). Direct measurements of meltwater runoff on the greenland ice sheet surface. *Proceedings of the National Academy of Sciences*, 114(50):E10622–E10631.

Sole, A., Nienow, P., Bartholomew, I., Mair, D., Cowton, T., Tedstone, A., and King, M. A. (2013). Winter motion mediates dynamic response of the Greenland Ice Sheet to warmer summers. *Geophys. Res. Lett.*, 40(15):3940–3944.

Sommers, A., Rajaram, H., and Morlighem, M. (2018). Shakti: Subglacial hydrology and kinetic transient interactions v1.0. *Geoscientific Model Development*, 11(7):2955–2974.

Spring, U. and Hutter, K. (1982). Conduit flow of a fluid through its solid phase and its application to intraglacial channel flow. *International Journal of Engineering Sciences*, 20:327–363.

Tedstone, A. J., Nienow, P. W., Gourmelen, N., Dehecq, A., Goldberg, D., and Hanna, E. (2015). Decadal slowdown of a land-terminating sector of the Greenland Ice Sheet despite warming. *Nature*, 526(7575):692–695.

Teutsch, G. and Sauter, M. (1991). Groundwater modeling in karst terranes: Scale effects, data acquisition and field validation. In *Third Conference on Hydrogeology, Ecology, Monitoring, and Management of Ground Water in Karst Terranes. National Ground Water Association, Dublin, Ohio*, pages 17–35.

Tsai, V. C. and Rice, J. R. (2010). A model for turbulent hydraulic fracture and application to crack propagation at glacier beds. *J.Geophys. Res.*, 115(F3):F03007.

Tulaczyk, S., Kamb, W. B., and Engelhardt, H. F. (2000). Basal mechanics of Ice Stream B, West Antarctica: 2. Undrained plastic bed model. *J. Geophys. Res.*, 105(B1):483–494.

van de Wal, R. S. W., Boot, W., van den Broeke, M. R., Smeets, C. J. P. P., Reijmer, C. H., Donker, J. J. A., and Oerlemans, J. (2008). Large and rapid melt-induced velocity changes in the ablation zone of the Greenland Ice Sheet. *Science*, 321(5885):111–113.

van de Wal, R. S. W., Smeets, C. J. P. P., Boot, W., Stoffelen, M., van Kampen, R., Doyle, S. H., Wilhelms, F., van den Broeke, M. R., Reijmer, C. H., Oerlemans, J., and Hubbard, A. (2015). Self-regulation of ice flow varies across the ablation area in south-west Greenland. *The Cryosphere*, 9(2):603–611.

Vaughan, D. G., Comiso, J. C., Allison, I., Carrasco, J., Kaser, G., Kwok, R., Mote, P., Murray, T., Paul, F., Ren, J., E., R., Solomina, O., Steffen, K., and Zhang, T. (2013). *Observations: Cryosphere. In: Climate Change 2013: The Physical Science Basis. Contribution of Working Group I to the Fifth Assessment Report of the Intergovernmental Panel on Climate Change.* Cambridge University Press, Cambridge, United Kingdom and New York, NY, USA.

Walder, J. S. (1986). Hydraulics of subglacial cavities. *J. Glaciol.*, 32(112):439–445.

Walder, J. S. and Fowler, A. (1994). Channelized subglacial drainage over a deformable bed. *J. Glaciol.*, 40(134):3–15.

Walker, R. T., Werder, M. A., Dow, C. F., and Nowicki, S. M. J. (2017). Determining ice-sheet uplift surrounding subglacial lakes with a viscous plate model. *Frontiers in Earth Science*, 5:103.

Weertman, J. (1962). Catastrophic glacier advances. In *Union Géodésique et Géophysique Internationale, Association Internationale d'Hydrologie Scientifique. Colloque d'Obergurgl 10–18 Sept 1962.*, pages 31–39.

Werder, M. A. (2016). The hydrology of subglacial overdeepenings: A new supercooling threshold formula. *Geophys. Res. Lett.*, 43(5):2045–2052.

Werder, M. A., Hewitt, I. J., Schoof, C. G., and Flowers, G. E. (2013). Modeling channelized and distributed subglacial drainage in two dimensions. *J. Geophys. Res.*, 118:1–19.

Werder, M. A., Schuler, T. V., and Funk, M. (2010). Short term variations of tracer transit speed on alpine glaciers. *The Cryosphere*, 4:381–396.

Wright, P. J., Harper, J. T., Humphrey, N. F., and Meierbachtol, T. W. (2016). Measured basal water pressure variability of the western greenland ice sheet: Implications for hydraulic potential. *J. Geophys. Res.*, 121(6):1134–1147.